TECHNICAL UNIVERSITY OF CRETE

DIPLOMA THESIS

Eccentricity impact and detection in permanent magnet generators for renewables

---

Author:
Stefanos KARAMPAS

Thesis Committee:
Assoc. Prof. Dr. Konstantinos GYFTAKIS
(Supervisor)
Prof. Dr. Eftichios Koutroulis
Asst. Prof. Dr. Georgios Peppas

School of Electrical and Computer Engineering

Πολυτεχνείο Κρήτης

Διπλωματική Εργασία

Επίδραση και διάγνωση της εκκεντρότητας σε γεννήτριες μόνιμων μαγνητών για ανανεώσιμες

Συγγραφέας:
Στέφανος Καραμπάς

Εξεταστική Επιτροπή:
Αναπλ. Καθ. Κωνσταντίνος Γυφτάκης
(Επιβλέπων)
Καθηγητής Ευτύχιος Κουτρούλης
Επίκ. Καθ. Γεώργιος Πέππας

Σχολή Ηλεκτρολόγων Μηχανικών και Μηχανικών Υπολογιστών

TECHNICAL UNIVERSITY OF CRETE

Abstract

Electrical and Computer Engineering

Eccentricity impact and detection in permanent magnet generators for renewables

by Stefanos KARAMPAS

This thesis explores the diagnosis of static,dynamic and mixed eccentricity faults in permanent magnet synchronous generators (PMSGs). For the purposes of this thesis, the C-GEN topology, a double rotor, slotless, air-cored Permanent Magnet Synchronous Generator, was employed. Traditional diagnostic methods, such as Motor Current Signature Analysis (MCSA), can lead to false negative results due to the double rotor configuration, air-cored structure and circuit design, which can suppress fault signatures and reduce diagnostic accuracy.

The performance and reliability of the C-GEN machine depends on the early identification of eccentricity faults. The machine coils are subjected to electrical and thermal stress as a result of circulating currents in the circuit's parallel coils caused by the eccentricity fault. This stress can degrade insulation and aggravate faults, leading potentially to secondary failures such as winding short circuits or rotor demagnetization.

A Finite Element Method (FEM) Software (Simcenter MAGNET) is used in this study to examine the generator's behavior, under varying load and fault conditions. The simulated data was post-processed in MATLAB to diagnose each fault condition and analyze the behavior associated with eccentricity faults. The study evaluates multiple diagnostic techniques, such as MCSA, Torque Monitoring, Flux Monitoring, Magnetically Coupled Search Coils, and Zero-Sequence Flux (ZSF). ZSF emerged as the most reliable method, offering robust fault identification and high sensitivity.

TECHNICAL UNIVERSITY OF CRETE

Abstract

Electrical and Computer Engineering

Eccentricity impact and detection in permanent magnet generators for renewables

by Stefanos KARAMPAS

Αυτή η διπλωματική εργασία εξετάζει τη διάγνωση σφαλμάτων στατικής, δυναμικής και μεικτής εκκεντρότητας σε σύγχρονες γεννήτριες με μόνιμους μαγνήτες. Για τους σκοπούς της παρούσας εργασίας, χρησιμοποιήθηκε η τοπολογία C-GEN, μια σύγχρονη γεννήτρια με δύο δρομείς, χωρίς αυλάκια και χωρίς φερομαγνητικό πυρήνα στο στάτη. Οι παραδοσιακές μέθοδοι διάγνωσης, όπως η Ανάλυση Υπογραφής Ρεύματος Κινητήρα (MCSA), μπορούν να οδηγήσουν σε ψευδώς αρνητικά αποτελέσματα λόγω της τοπολογίας του διπλού δρομέα, της ελλειψης πυρήνα στο στάτη και του σχεδιασμού του κυκλώματος, που περιορίζουν τις χαρακτηριστικές υπογραφές σφάλματος και μειώνουν την ακρίβεια διάγνωσης.

Η απόδοση και η αξιοπιστία της μηχανής C-GEN εξαρτάται από την έγκαιρη ανίχνευση των σφαλμάτων εκκεντρότητας. Τα πηνία της μηχανής υφίστανται ηλεκτρική και θερμική καταπόνηση λόγω των κυκλοφορούντων ρευμάτων στα παράλληλα πηνία του κυκλώματος, τα οποία προκαλούνται από το σφάλμα εκκεντρότητας. Αυτή η καταπόνηση μπορεί να υποβαθμίσει τη μόνωση και να επιδεινώσει τα σφάλματα, οδηγώντας ενδεχομένως σε δευτερογενείς βλάβες, όπως εσωτερικά βραχυκυκλώματα ή απομαγνήτιση των μόνιμων μαγνητών.

Στην παρούσα εργασία, χρησιμοποιήθηκε λογισμικό Μεθόδου Πεπερασμένων Στοιχείων (FEM) (Simcenter MAGNET) για την εξέταση της συμπεριφοράς της γεννήτριας υπό διάφορες συνθήκες φορτίου και σφάλματος. Τα προσομοιωμένα δεδομένα υποβλήθηκαν σε επεξεργασία με MATLAB για τη διάγνωση κάθε κατάστασης σφάλματος και την ανάλυση της συμπεριφοράς που σχετίζεται με τα σφάλματα εκκεντρότητας. Η μελέτη αξιολογεί πολλές διαγνωστικές τεχνικές, όπως η η Ανάλυση Υπογραφής Ρεύματος Κινητήρα, η Ανάλυση Υπογραφής Ροπής, η Ανάλυση Φάσματος Μαγνητικής Ροής, τα Μαγνητικά Συζευγμένα Ανιχνευτικά Πηνία και τήν Ανάλυση Μαγνητικής Ροής Μηδενικής Ακολουθίας (ZSF). Η Ανάλυση Μαγνητικής Ροής Μηδενικής Ακολουθίας αναδείχθηκε ως η πιο αξιόπιστη μέθοδος, προσφέροντας ισχυρή ταυτοποίηση σφαλμάτων και υψηλή ευαισθησία.

Acknowledgements

I would like to express my profound gratitude to Professor Konstantinos Gyftakis for his valuable guidance, expertise, and support throughout the duration of this work. His instructive feedback and encouragement were very crucial to the successful completion of this thesis, and I consider myself privileged to have had the opportunity to work under his supervision.

I am also deeply thankful to my collaborator Nikos Giolekas, who contributed a great deal with his commitment, insightful discussions, and collaboration that shaped the outcomes of this research.

To my friends and family, thanks for their understanding and continuous support throughout the period of this work. Their encouragement kept me motivated and focused during those times when things seemed very tough.

This thesis is as much a result of your contributions as it is my own effort. Thank you all.

Contents

List of Figures

List of Abbreviations

PMSM	**P**ermanent **M**agnet **S**ynchronous **M**achine
PMSGs	**P**ermanent **M**agnet **S**ynchronous **G**enerators
FEM	**F**inite **E**lement **M**ethod
MMF	**M**agneto**m**otive **F**orce
SPM	**S**urface **P**ermanent **M**agnet
IPM	**I**nset **P**ermanent **M**agnet
ZSF	**Z**ero-**S**equence **F**lux
ZSC	**Z**ero-**S**equence **C**omponent
MCSA	**M**otor **C**urrent **S**ignature **A**nalysis
RFPM	**R**adial **F**lux **P**ermanent **M**agnet
AFPM	**A**xial **F**lux **P**ermanent **M**agnet
FFT	**F**ast **F**ourier **T**ransform
NECP	**N**ational **E**nergy and **C**limate **P**lan
EV	**E**lectric **V**ehicle
EMF	**E**lectromotive **F**orce
PM	**P**ermanent **M**agnet
AC	**A**lternating **C**urrent
DC	**D**irect **C**urrent
RPM	**R**otations **P**er **M**inute
RMS	**R**oot **M**ean **S**quare

Chapter 1

Introduction

1.1 Wind Energy

Wind energy is the product of solar energy. The sun heats the Earth's surface unevenly, resulting in some areas warming up faster than others. The difference in temperature creates the movement of huge masses of air from one region to another. This movement of air is known as wind [1]. Wind energy is of great interest because it is a renewable, non-polluting source of energy. Up until the present time, the main source of electricity generation was coal. Coal, however, is a resource that is both polluting and expendable. With rising concerns about energy security and a growing need to cut greenhouse gas emissions, many nations are taking steps toward adopting renewable and alternative energy sources. This shift is driven by a commitment to reducing dependency on fossil fuels, aiming for cleaner, more reliable power options that can sustain long-term environmental and economic stability. This has led to an increase in wind energy applications, with an approximate annual growth of 10-15% per year in the last decade [2].

1.2 Wind Turbines

Wind turbines are machines that convert the kinetic energy of air in motion into electricity. The key components of a wind turbine are [3]:

- Blades : There are usually two or three blades, which are responsible for capturing and optimizing the wind.
- Shaft: The captured air from the blades rotates the shaft.
- Generator: The Generator converts the rotational energy from the shaft into electricity. It is placed inside the nacelle of the turbine.
- Tower: The role of the tower is to elevate the turbine so the blades can capture stronger and more consistent winds. This in turn produces more power.

Another component of the turbine is the gearbox. The gearbox is connected to the shaft, and its role is to increase the rotational speed that is input to the generator. The gearbox, however, may be a disadvantage to the design of a turbine because it is usually under a lot of mechanical stress and is often in need of replacement. This gives rise to the development of new designs, such as direct-drive machines that don't use the gearbox [4].

Regions that normally present the most attractive potential are located near coasts, inland areas with open terrain or on the edge of bodies of water. Some mountainous areas also have good potential.

Typically, Onshore wind turbines come to mind when we think of wind turbines. In the last decade, however, there has been a significant rise in Offshore wind turbines.

1.2.1 Offshore vs Onshore Wind Turbines [5]

Offshore wind Turbines have gained significant attention over the last decade because of their potential to have higher energy production. Offshore wind is an attractive energy proposition for countries with long coastlines and with major demand centers located in proximity. Typically, offshore winds are stronger and more consistent without turbulence compared to onshore winds. This means that offshore turbines have a higher life expectancy without the need of regular maintenance. However offshore are expensive to construct and have a higher maintenance cost due to the challenges from the difficult location and access to them. Onshore wind turbines are a more wide-spread technology due to the low cost of maintenance and construction and may be a better solution for some cases.

The table below compares the advantages and disadvantages of both Onshore and Offshore wind turbines, highlighting their respective strengths and weaknesses

Wind Turbines	Advantages	Disadvantages
Onshore	• Lower initial costs • Easier to access for maintenance • Easier integration with the grid • More established technology	• Lower energy production due to less consistent wind • Limited by land availability • Visual and noise pollution concerns • Local opposition due to land use
Offshore	• Stronger, more consistent winds • Higher energy generation potential • Longer operational life expectancy • Fewer land-use conflicts	• Higher installation and maintenance costs • Technological challenges in installation and operation • Environmental impact on marine ecosystems

TABLE 1.1: Advantages and Disadvantages of Offshore and Onshore Wind Turbines

1.2.2 Developement of Wind Turbines in Greece [6],[7]

Greece has made significant strides in expanding wind energy, targeting both onshore and offshore development to meet its climate targets. Onshore wind farms have played a foundational role in Greece's renewable energy sector, currently providing over 4.5 GW of installed capacity. They cover approximately 18% of Greece's electricity needs, with future targets pushing to expand this share as part of the National Energy and Climate Plan (NECP) for 2030. The plan sets forth ambitious goals, including a 58% reduction in greenhouse gas emissions by 2030, an 80% reduction by 2040, and achieving full carbon neutrality by 2050.

Greece is setting ambitious goals for offshore wind energy, aiming to install a minimum of 2 GW by 2030. A newly passed offshore wind law is paving the way for this transition. Because Greece's coastal waters are quite deep, floating wind turbines are expected to play a key role. This allows turbines to be place farther out at sea, where the conditions for energy generation are more ideal. Key areas for these plans include the waters around Crete, Cyclades and the Dodecanese.

1.3 Objective of the Thesis

The main focus of this thesis is the impact and detection of eccentricity faults in permanent magnet synchronous generators (PMSGs). For the purpose of this thesis, the C-GEN Topology was used. The study intends to assess the performance of different diagnostic methods for the identification and characterization of static, dynamic, and mixed eccentricity faults, considering the challenges introduced by the circuit design and the double-rotor, slotless, air-cored design of the C-GEN generator.

To achieve this, Finite Element Method (FEM) is used to simulate fault conditions. Various diagnostic techniques will be employed, exploring their performance and limitations in identifying the eccentricity faults. By comparing their sensitivities and limitations, the study seeks to identify the most effective methods for real-time fault detection.

Lastly, the thesis aims to provide insights to the implications posed by the eccentricity faults, such as circulating currents in the parallel coils of the electrical circuit of the machine.

1.4 Thesis Outline

Chapter 2: Synchronous Generators This chapter discusses the operating principles, components, and classifications of synchronous generators, highlighting the advantages of permanent magnet generators and the innovative C-GEN technology.

Chapter 3: Faults and Detection Methods in Permanent Magnet Synchronous Generators
This chapter identifies common faults in permanent magnet synchronous generators, focusing on the eccentricity fault, and describe various diagnostic techniques.

Chapter 4: Finite Element Method and Model Creation
This chapter details the application of the Finite Element Method (FEM) for modeling the C-GEN topology, outlining its design, components, and simulation processes using the SimCenter Magnet software.

Chapter 5: Study Results and Analysis
This chapter presents the results of the study, analyzing the performance of various diagnostic methods and the behavior of the C-GEN under different fault conditions using FEM simulations.

Chapter 6: Conclusions and Future Work
This chapter concludes the thesis by summarizing the findings, discussing their implications, and recommending future work directions.

Chapter 2

Synchronous Generators

2.1 Fundamental Concepts in Magnetism and Magnetic Circuits [8]

The magnetic field is defined as the space in which a conductor experiences a force of magnetic nature when placed within it. To quantify the strength of this field, Faraday introduced the concept of flux lines. He imagined the field as a series of lines, and the density of these lines passing through a given surface provides information about the strength of the magnetic field at that point. In this context, the scalar quantity Φ (magnetic flux) was defined as the number of magnetic flux lines passing through a surface A. It is mathematically expressed as:

$$\Phi = \oint_A \mathbf{B} \cdot dA \tag{2.1}$$

Where $\mathbf{B}$ is the vector of magnetic field density and dA is the differential element of area through which the flux is passing.

Another fundamental quantity in magnetism is the magnetic field intensity H, which represents the "effort" of the current in creating a magnetic field. It is related to the magnetic flux density B by the following relation:

$$B = \mu H \tag{2.2}$$

Where μ is the magnetic permeability of the material and expresses the ease with which magnetic flux lines can pass through the material. The relative magnetic permeability is defined as a measure of comparison between materials. It is given by:

$$\mu_r = \frac{\mu}{\mu_0} \tag{2.3}$$

Where $\mu_0 = 4\pi \times 10^{-7}$ H/m is the permeability of free space.

It is also important to define the magnetic reluctance, denoted by $\mathcal{R}$. Magnetic reluctance in a magnetic circuit is analogous to electrical resistance in an electrical circuit in that resistance is a measure of the opposition to the electric current. The reluctance of a magnetic circuit depends on the geometry of the path, the material's magnetic properties, and the length of the path through which the flux flows. It is given by the following relation :

$$\mathcal{R} = \frac{l}{\mu A} \tag{2.4}$$

Where l is the length of the magnetic path, μ is the magnetic permeability of the material, A is the cross-sectional area of the magnetic path.

Lastly we need to define the Magnetomotive force (MMF). Magnetomotive Force is a measure of the driving force that causes magnetic flux to flow through a magnetic circuit, analogous

to the voltage in an electrical circuit, which drives electric current. It represents the "push" of the magnetic field and is responsible for establishing the magnetic flux within a magnetic material. It is given by two equivalent equations. The first equation is :

$$\mathcal{F} = NI \tag{2.5}$$

Where $\mathcal{F}$ is the magnetomotive force in Ampere-Turns (At), N is the number of turns in the coil, I is the current flowing through the coil (in amperes).

The second equation is given by :

$$\mathcal{F} = \Phi\mathcal{R} \tag{2.6}$$

Where $\mathcal{F}$ is the magnetomotive force in Ampere-Turns (At), Φ is the magnetic Flux (measured in Weber, Wb), $\mathcal{R}$ is the magnetic reluctance (measured in Ampere-Turns per Weber, At/Wb).

2.2 Operating Principles and Components of Synchronous Generators

The operating principle of synchronous generators is based on Faraday's Law of Electromagnetic Induction [8] :

$$\mathcal{E} = -N\frac{d\Phi}{dt} \tag{2.7}$$

where $\mathcal{E}$ is the induced electromotive force (emf) in volts, Φ is the magnetic flux in webers (Wb), and $\frac{d\Phi}{dt}$ represents the rate of change of magnetic flux. N is the number of turns in a coil. The equation above (2.7) states that a time-varying magnetic field induces a voltage in a nearby conductor.
Generators consist primarily of two components: the **rotor** and the **stator**.

- **Rotor**: The rotating part of the generator responsible for producing a magnetic field that is used in the generation of electricity. It usually bears either current-carrying conductors or permanent magnets. When a DC supply is given to it, the rotor develops a stationary magnetic field. If the rotor is rotated, then the magnetic field also rotates with it.
- **Stator**: The stationary part of the generator, the stator is typically composed of coils wound around a laminated iron core. As the rotor turns, the magnetic field crosses the stator windings, inducing an alternating voltage in each stator coil due to electromagnetic induction.

The synchronous generator gets its name from its property to generate voltages at a frequency equal to the frequency of the rotating magnetic field in the machine. Alternatively said, the speed of the rotor is proportional to the voltage frequency that is induced in the stator, where a constant relationship between the two exists given by (2.8)

$$n_s = \frac{60 f_s}{p} \tag{2.8}$$

Where n_s is the rotational speed of the magnetic field, f_s the electrical frequency of the stator and p the number of pole pairs in the machine. The rotational speed of the magnetic field is equal to the speed of the rotor and so the above equation gives us the relation between the speed of the machine and its frequency.

In order for the generator to work the rotor must be rotated by a mechanical force. This mechanical force may come from renewable energy sources like, wind energy, tidal waves, hydropower and even geothermal energy.

Another essential component for the generator's operation is the rotor's ability to produce a stationary magnetic field. Typically windings connected to a power supply are placed inside the rotor. When the windings are excited with DC current they generate a stationary magnetic field. As the rotor rotates, the magnetic field it generates also rotates. This rotating magnetic field is then seen by the stator. As a result, an induced voltage is produced in the stator coils due to the changing magnetic flux.

Generators with windings on the rotor usually include components that work together to produce electrical power. Such components are brushes and slip rings. Their role is to provide a continuous electrical contact between the rotating rotor and the external DC power supply, despite the constant rotation. This is achieved through brushes that are in contact with the slip rings. As the slip rings rotate, the brushes maintain their position, allowing the current to flow continuously. However brushes and slip rings come with two major disadvantages [9]. The first one is the frequent need of replacement of the brushes because of their constant friction and stress. The second disadvantage comes from the voltage drop present in brushes that increases the power losses. As the DC excitation current is increased the voltage drop in brushes increases and we have unwanted power losses that affect the efficiency of the machine.

Because of these disadvantages the need to remove the slip rings and brushes arises. Instead of windings in the rotor, DC current can also be produced by permanent magnets placed in the rotor. These magnets produce the necessary stationary magnetic field so the generator may work, without the need of the excitation winding inside the rotor. This topology with the permanent magnets inside the rotor comes with great advantages such as the removal of slip rings and brushes and other extra components used for the topology with the rotor windings. Permanent magnet generators also have higher torque compared to generators with windings on the rotor [10]. Permanent magnets are constructed from rare earth materials. These materials often have high magnetic strength and so machines with high power density, high efficiency and smaller size compared to conventional generators are constructed.

The main reason why machines with permanent magnets weren't used often until recently is because of the high cost and rarity of permanent magnets as well as the lack of knowledge about power electronics. With the development of power electronics and the drop of rare earth materials prices, machines with permanents magnets are a viable option with great potential. Machines with permanent magnets are well-suited for a wide variety of renewable energy applications [11].

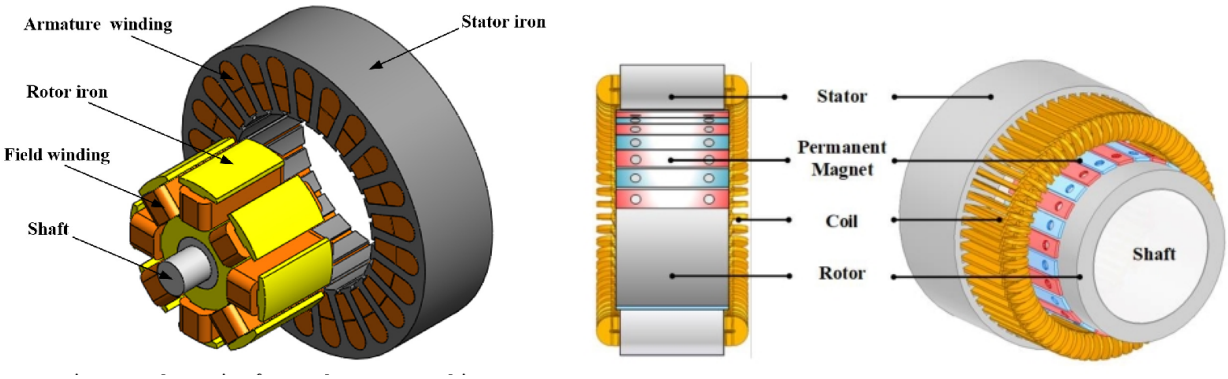

(A) Synchronous Wound Rotor Generator [12] (B) Synchronous Permanent Magnet Generator [13]

FIGURE 2.1: Types of Synchronous Generators

2.3 Synchronous Generators with Permanent Magnets

As discussed in the previous section, synchronous generators with permanent magnets are machines that use permanent magnets to generate the stationary magnetic field in the rotor, eliminating the need for an external excitation system. The classification of these machines can vary and depending on the direction of the air-gap magnetic field, the position of the magnets, the position of the rotor and the structure of the stator.

2.3.1 Radial and Axial Flux Synchronous Generators

Synchronous generators can be classified into radial flux (RFPM) and axial flux (AFPM) types based on the direction of the air-gap magnetic field. In radial flux machines, the magnetic flux is perpendicular to the axis (shaft) of the machine. In contrast, in axial flux machines, the magnetic flux flows parallel to the machine's axis. This distinction affects the generator's design, performance, and application suitability. Each topology has its advantages and disadvantages and will be discussed in this section

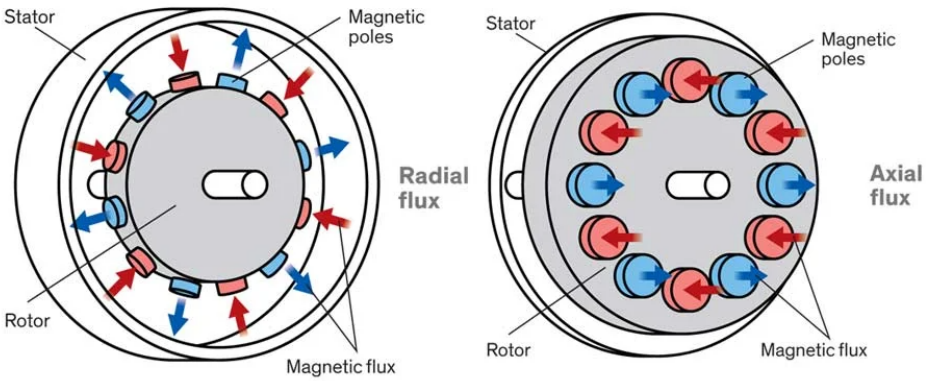

FIGURE 2.2: Comparison of Radial and Axial Flux in Synchronous Generators [14]

Radial Flux machines are the most widely used type of synchronous generators with permanent magnets. Because the direction of the magnetic flux is radial, the lamination of the stator core is done axially, which makes the manufacturing process easier. Radial flux machine design, especially in relation to the stator lamination, is inherently low cost which has made this topology widespread [15].

Axial flux machines are more expensive and the manufacturing process is more difficult. Also the increased tractive forces between the stator and rotor in AFPM machines can lead to mechanical challenges reducing the overall reliability and lifespan of the machine. However they offer several advantages over RFPM machines [16]. For instance, AFPM machines have smaller volume for the same power rating compared to a RFPM machine. AFPM are an attractive option for applications where space and weight constraints take place. Such applications are for example electric vehicles (EVs) and aerospace.

In summary, radial flux machines are currently the best performer in the synchronous generator market owing to their cost advantage, lower complexity and long-established manufacture. These machines hold the market by virtue of their ruggedness, scalability and ability to operate at high power with relatively low manufacturing costs. While axial flux machines are making inroads into niche areas that demand high power density, compactness and lightweight designs, they are hindered by higher fabrication costs and mechanical limitations such as tractive forces between the rotor and stator.

2.3.2 Inner and Outer Rotor Synchronous Generators

Synchronous Generators featuring Permanent Magnets can be categorized based on the rotor's positioning. The rotor may be situated internally, encircled by the stator, or externally, enveloping the stator. These configurations are applicable to both Radial Flux and Axial Flux machines. In the Inner Rotor design, the stator is positioned externally. The permanent magnets are placed to the internal rotor, which rotates within the fixed stator, allowing the outer section to remain stationary while the internal elements are in motion. In the Outer Rotor design, the stator is positioned internally. The permanent magnets are placed to the external rotor, which rotates on the outside of the fixed stator, allowing the inner section to remain stationary while the external elements are in motion.

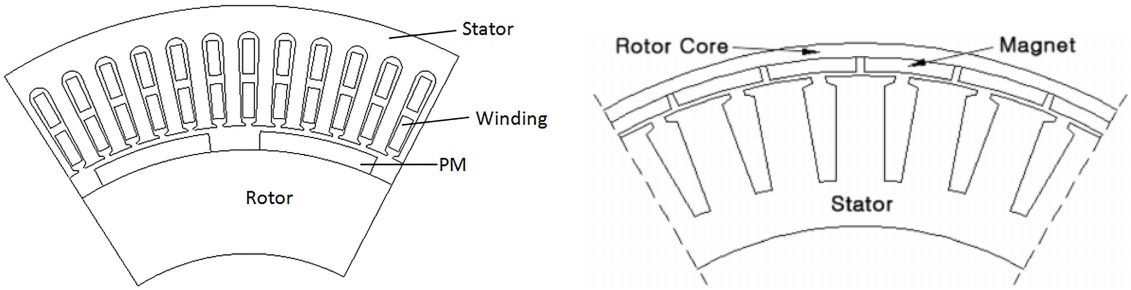

(A) Synchronous Permanent Magnet Generator with Inner Rotor [17]

(B) Synchronous Permanent Magnet Generator with Outer Rotor [18]

FIGURE 2.3: Inner Rotor vs Outer Rotor Topologies

The inner rotor topology is the most common and widely used configuration compared to the outer rotor design. With the stator located on the outside of the machine, heat dissipation is more efficient, enhancing thermal management. The inner rotor topology is more suited for high speed applications. The rotor is compact and centrally located, reducing centrifugal forces at high speeds. This ensures the mechanical stability of the system and minimizes the risk of structural failure. A smaller rotor has less surface area for placing poles, which naturally limits the number of poles that can be installed. According to equation (2.8) the number of poles are inversely proportional to the speed of the rotor. This means that inner rotor permanent magnet generators can reach higher speeds due to the smaller diameter of the rotor.

On the other hand, Outer Rotor permanent magnet generators are more suited for low speed applications. These machines can be used very efficiently with Wind Turbines. Due to the larger surface area of the outer rotor, more poles can be placed on the rotor and so the generator can work with low rotational speeds. This is essential for applications where the gearbox is excluded from the design (Direct-Drives). Also with this topology, the permanent magnets are less prone to demagnetization due to thermal stress, because they are directly exposed to the wind and have enhanced cooling [16].

In conclusion, the choice between outer rotor and inner rotor designs, heavily depends on the specific application. The outer rotor topology is ideal for low-speed applications, while the inner rotor topology is better suited for high-speed operations.

2.3.3 Placement of Permanent Magnets in Synchronous Generators

Synchronous Generators with Permanent Magnets can be classified to two main different categories, depending on the placement of the magnets. These categories are:

- Surface mounted permanent magnet synchronous machines (SPM)
- Inset permanent magnet synchronous machines (IPM)

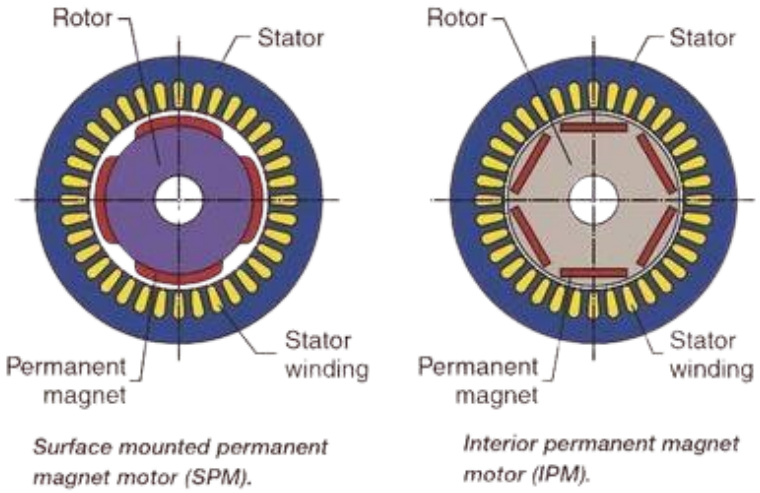

FIGURE 2.4: IPM vs SPM Rotor Desing [19]

Surface mounted permanent magnet synchronous machines

In this category the permanent magnets are mounted on the surface of the rotor as is implied by their name. Because the magnets are on the surface, the rotor has a relatively simple construction, which reduces complexity and manufacturing costs. This magnet configuration is typically used for low-speed applications due to the limitation that, at high speeds, the centrifugal forces could cause the magnets to become detached from the rotor. The permeability of the permanent magnets is almost equal to that of the air. That means that the effective air-gap is typically larger in SPM machines. Larger air-gap means larger magnetic path length and so a bigger reluctance (2.4). When the magnetic reluctance increases, it leads to a decrease in the magnetic flux for a given MMF (2.6) and, consequently, reduced torque and efficiency. This implies that to enhance the magnetic flux density (B) and improve efficiency, stronger magnets must be used, which in turn increases the cost of the machine. These machines also exhibit minimal saliency, as the permeabilities along the direct and quadrature axes are nearly identical. This is due to the fact that the permeability of the air gap is almost equal to the permeability of the permanent magnets. As a result, the ability to control the magnetic flux is limited, reducing the machine's overall performance in applications that require dynamic flux regulation (Variable speed drives).

Inset permanent magnet synchronous machines

In this category the permanent magnets are placed inside the rotor core. Typically IPM machines have many advantages compared to SPM. They have smaller reluctance in the air-gap, increased magnetic flux density, increased efficiency and torque. They also exhibit saliency which gives the ability to control the magnetic flux of the machine. They are typically used in high speed applications and in variable speed drives. However IPM machines are expensive to manufacture and exhibit high torque ripple especially for low speed applications [20].

2.3.4 Stator structure in Synchronous Generators

The synchronous machine can be further classified by the stator structure and the winding topology. The winding of electrical machines can be categorized to overlapping or non-overlapping. The non-overlapping winding is always concentrated, while the overlapping can be classified to concentrated and distributed.

The distributed overlapping winding generally results in a more sinusoidal magnetomotive force (MMF) distribution and EMF waveform, reducing harmonics and eddy currents [21]. However the distributed overlapping winding has several disadvantages. To achieve the overlapping configuration, the winding heads must bend, resulting in longer end windings . However, these end windings do not contribute to the generation of electromotive force (EMF) through induction. Their role is limited to transferring current from one coil to another. Thus, machines with this type of stator winding experience increased copper losses (Cu losses) [22].

In concentrated winding the coil turns are concentrated around one tooth and therefore it will benefit from short end windings due to non-overlapping property. Another advantage is that this winding topology concentrates the magnetic flux, resulting in a high magnetomotive force (MMF). This concentration enhances the efficiency of the magnetic circuit, improving the overall performance of the machine [23]. However concentrated windings display high cogging torque. Cogging torque is the unwanted torque ripple in a machine caused by the interaction between the permanent magnets and the stator teeth, resulting in a jerky or uneven motion as the rotor aligns with the stator slots. This will affect the production of the total torque. Also concentrated windings lead to a less sinusoidal magnetomotive force (MMF) distribution and a distorted electromotive force (EMF) waveform, which increases harmonic content and induces higher eddy currents [21].

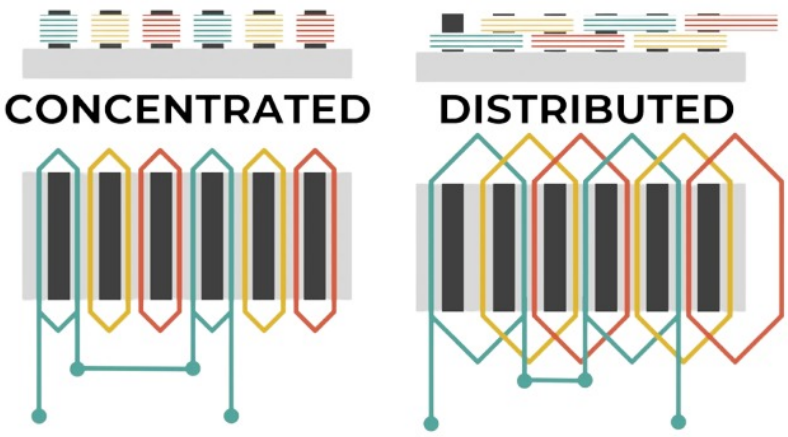

FIGURE 2.5: Concentrated and Distributed Winding Topologies [24]

Slotless Stator

To reduce the cogging torque associated with stators having concentrated windings, slotless stator designs are often employed. In these configurations, the absence of stator slots eliminates the interaction between the rotor magnets and the slot teeth, which is a primary cause of cogging [25]. This results in smoother torque production and improved performance, particularly in applications where low torque ripple is crucial.

2.4 C-GEN Technology

C-GEN Permanent Magnet Generators are representative of a state-of-the-art technology that enables the development of lightweight, direct-drive generators specific to wind plants or tidal wave generators [26]. Direct-drive machines are generally more complex and heavier than gear-driven machines. This is because they eliminate the gearbox, requiring a generator with a larger diameter to produce sufficient torque at low rotational speeds. The enlargement is also required to fit more poles and higher magnetic flux density. This also adds to the machine's weight, making machine manufacture more complex and increasing production cost.

C-GEN is an air-cored, slotless stator with non-overlapping concentrated windings machine. The distinctive topology consists of two rotors and one stator, and it is flexible enough to be setup in either radial flux or axial flux topology. This design offers multiple advantages. The absence of an iron core in the stator eliminates hysteresis and eddy current losses, enhancing efficiency. The slotless configuration removes the cogging torque entirely as there is no interaction between the permanent magnets and the stator teeth, which typically cause such a torque. Furthermore, concentrated, non-overlapping winding topology shortens end winding lengths, which, in turn, results in reduced copper losses and, as a result, better machine performance and energy efficiency [27].

The C-GEN machine gets its name from its unique core design, which supports the magnets positioned on both the inner and outer rotors. This distinctive configuration directs the primary structural load onto the C-shaped core, which not only counteracts the magnetic attraction between the magnets but also serves as a pathway for both inter-pole and intra-pole flux [28]. (Figure 2.6)

In the double-rotor topology, magnets are mounted on both the inner and outer surfaces of the rotors, creating a symmetrical magnetic field. The air-cored or slotless stator is positioned between the two rotors. Magnetic flux flows from the north poles on one rotor to the south poles on the other, passing through the air gap. The magnetic path primarily consists of air, which has a much lower permeability compared to iron. This increases the effective magnetic air-gap length, because the magnetic flux has to travel through a less efficient medium without the iron to guide it. This results in a larger air-gap reluctance (2.4). Since the reluctance is higher, the air-cored machine requires more MMF for the same flux (2.6), resulting in a weaker magnetic circuit compared to an iron-cored machine. To compensate for this more permanent magnet material or stronger magnets (NdFeB) and a larger radius can be used if the same torque as an iron-cored machine is required [27].

The stator structure can be significantly lighter because it experiences less stress and does not require as much stiffness compared to iron core design. The maxwell stress is the force per unit area exerted on the machine by the magnetic field. This stress is proportional to the square of the magnetic field in the air-gap. The normal component of Maxwell stress q can be calculated as :

$$q = \frac{B^2}{2\mu_0} \tag{2.9}$$

Since there is no iron core to concentrate the magnetic field, magnetic field density (B) in the air-gap is much lower than in a machine with a ferromagnetic core. Due to the reduced shear stress the air-cored machine must be larger than an iron-cored machine which is rated for the same torque.

$$\sigma = \frac{F}{A_r} \tag{2.10}$$

Where F is the force and A_r is the rotor area.

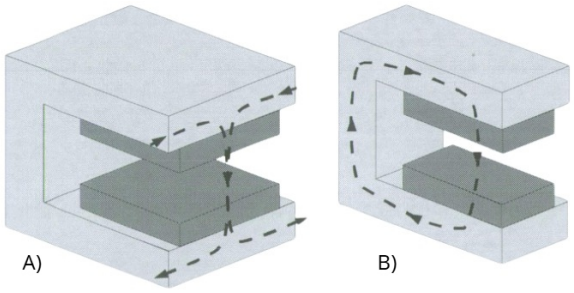

FIGURE 2.6: C-core flux paths (A) Intermodule (longitudinal) (B) Intramodule (transverse) [28]

2.4.1 Electromagnetic modeling of C-GEN [28]

In order to model C-GEN we need to draw the equivalent magnetic circuit.

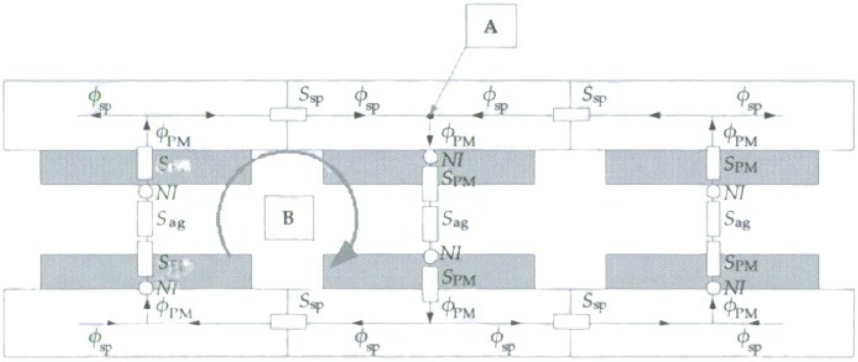

FIGURE 2.7: C-core (front) reluctance network [27]

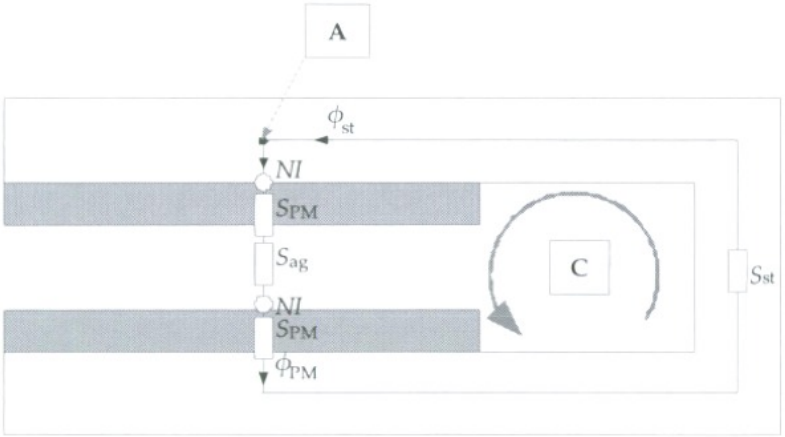

FIGURE 2.8: C-core (side) reluctance network [27]

(Figure 2.7) shows the magnetic circuit of 3 C-core modules from the front. Each C-core is composed of two steel components: the top and bottom sections. The top section is larger than the bottom to accommodate the larger surface area of the outer rotor. Additionally, the magnets on the outer rotor have a greater pitch compared to those on the inner rotor, ensuring effective flux linkage and balanced performance. Both steel components feature a trapezoidal shape, designed to align with the curved profile of the rotors, optimizing the magnetic path and minimizing leakage flux. For simplification purposes in (figure 2.7) , the top and bottom parts are assumed to have equal dimensions. Below is a figure depicting the main dimensions of the C-cored module that will be used in this analysis.

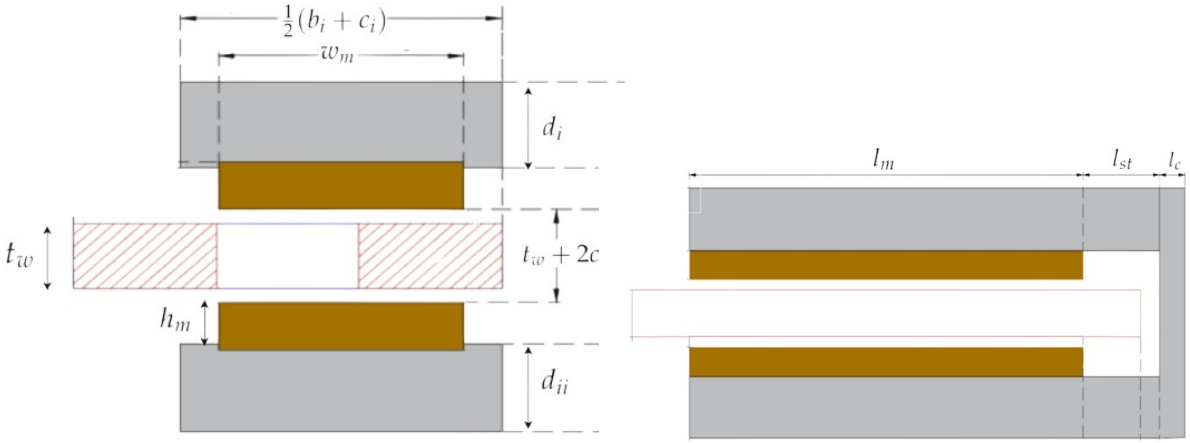

(A) (B)

FIGURE 2.9: Front view of C-cored module (A), Side view of C-cored module (B) [29]

The magnetic circuit model (Figures 2.7, 2.8) incorporates several elements, including sources of magnetomotive force (MMF), reluctances, and fluxes. The MMF produced by the magnets can be expressed as:

$$\mathcal{F}_{pm} = \Phi_{pm} \cdot \mathcal{R}_{pm} \overset{(2.1)}{=} B_r \cdot A_{pm} \cdot \mathcal{R}_{pm} \overset{(2.4)}{=} B_r \cdot \cancel{A_{pm}} \cdot \frac{B_r \cdot h_m}{\mu_0 \cdot \mu_r \cdot \cancel{A_{pm}}} = \frac{B_r \cdot h_m}{\mu_0 \cdot \mu_r} \overset{(2.5)}{=} N \cdot I \tag{2.11}$$

Where B_r the remnant flux density of the magnets used it the circuit, h_m the height of the magnets, μ_0 the permeability of free space, μ_r the relative permeability of permanent magnet material. Equation (2.11) illustrates that the same magnetomotive force (MMF) can also be generated by a coil with N turns carrying a current I.

The air-gap reluctance of the magnetic circuit can be expressed as :

$$S_{ag} = \mathcal{R}_{ag} \overset{(2.4)}{=} \frac{t_w + 2c}{l_m w_m \mu_0} \tag{2.12}$$

Where t_w is the winding height, c is the clearance between the windings and the magnets, l_m is the axial length of the magnets, w_m is the average pitch of the magnets.

The reluctance of the permanent magnets in both the bottom and top sections can be expressed as:

$$S_{pm,T} \overset{(2.4)}{=} \frac{h_m}{l_m w_{m,T} \mu_r \mu_0} + \frac{\frac{1}{2} d_i}{l_m w_{m,T} \mu_{st} \mu_0} \tag{2.13}$$

$$S_{pm,B} \overset{(2.4)}{=} \frac{h_m}{l_m w_{m,B} \mu_r \mu_0} + \frac{\frac{1}{2} d_{ii}}{l_m w_{m,B} \mu_{st} \mu_0} \tag{2.14}$$

Where μ_r is the relative permeability of the permanent magnets and μ_{st} is the relative permeability of the steel. The subscripts refer to the top (T) and bottom (B) magnets. The second fractions in (2.13) and (2.14) refer to the reluctance between the steel edge and node A of the magnetic circuit, where d_i is the height of the top steel and d_{ii} is the height of the bottom steel.

The reluctance of the intramodule steel as shown in (2.8) can be expressed as :

$$S_{st} \overset{(2.4)}{=} \frac{\frac{1}{2} l_m + l_{st} + l_c}{\frac{1}{2} d_i (b_i + c_i) \mu_{st} \mu_0} + \frac{2h_m + t_w + 2c}{\frac{1}{2} (b_{ii} + c_i) l_c \mu_{st} \mu_0} + \frac{\frac{1}{2} l_m + l_{st} + l_c}{\frac{1}{2} d_{ii} (b_{ii} + c_{ii}) \mu_{st} \mu_0} \tag{2.15}$$

Where l_{st} is the clearance between magnet and steel web and l_c is the thickness of the steel web. The dimensions of the trapezoidal top and bottom steel sections are represented as b_i,b_{ii},c_i and c_{ii}, where b corresponds to the larger base and c to the smaller base of the trapezoid. The subscript i denotes the top steel section, while ii refers to the bottom steel section.

The spacer reluctance is the reluctance of the intermodule steel and any air-gap between modules. It is expressed by :

$$S_{sp,T} \overset{(2.4)}{=} \frac{\frac{1}{2}(b_i + c_i)}{d_i l_m \mu_{st} \mu_0} + \frac{c_{sp}}{d_i l_m \mu_0} \tag{2.16}$$

$$S_{sp,B} \overset{(2.4)}{=} \frac{\frac{1}{2}(b_{ii} + c_{ii})}{d_{ii} l_m \mu_{st} \mu_0} + \frac{c_{sp}}{d_{ii} l_m \mu_0} \tag{2.17}$$

Where c_{sp} is the air-gap distance between modules. Typically there is no air-gap between modules, so $c_{sp} = 0$.

The next step in the electromagnetic modeling process is to define the fluxes within the magnetic circuit. The intramodule flux within the steel is denoted by Φ_{st}, while the intermodule flux in the steel is represented by Φ_{sp}. The fluxes associated with the permanent magnets (Φ_{pm}) and the air gap (Φ_{ag}) are considered equal, ensuring consistent magnetic flow through these components.

Applying Kirchhoff's Current Law, adapted for fluxes at node A of the magnetic circuit (figure 2.7) we get :

$$\begin{aligned} \Phi_{pm} &= 2\Phi_{sp} + \Phi_{st} \\ \Phi_{sp} &= \frac{1}{2}\Phi_{pm} - \frac{1}{2}\Phi_{st} \end{aligned} \tag{2.18}$$

Applying Kirchhoff's Voltage Law (MMF), for loop B of the magnetic circuit (figure 2.7) we get :

$$\begin{aligned} 4\frac{B_r \cdot h_m}{\mu_0 \cdot \mu_r} &= \Phi_{sp}(S_{sp,T} + S_{sp,B}) + 2\Phi_{pm}(S_{pm,T} + S_{pm,B}) + 2\Phi_{ag} S_{ag} \\ \frac{B_r \cdot h_m}{\mu_0 \cdot \mu_r} &= \frac{1}{4}\Phi_{sp}(S_{sp,T} + S_{sp,B}) + \frac{1}{2}\Phi_{ag}(S_{pm,T} + S_{pm,B} + S_{ag}) \\ &\overset{(2.18)}{=} -\frac{1}{8}\Phi_{st}(S_{sp,T} + S_{sp,B}) + \frac{1}{2}\Phi_{ag}(S_{pm,T} + S_{pm,B} + S_{ag} + \frac{1}{4}S_{sp,T} + \frac{1}{4}S_{sp,B}) \end{aligned} \tag{2.19}$$

Applying Kirchhoff's Voltage Law (MMF), for loop C of the magnetic circuit (figure 2.8) we get :

$$\begin{aligned} 2\frac{B_r \cdot h_m}{\mu_0 \cdot \mu_r} &= \Phi_{st} S_{st} + \Phi_{pm}(S_{pm,T} + S_{pm,B}) + \Phi_{ag} S_{ag} \\ \frac{B_r \cdot h_m}{\mu_0 \cdot \mu_r} &= \frac{1}{2}\Phi_{st} S_{st} + \frac{1}{2}\Phi_{ag}(S_{pm,T} + S_{pm,B} + S_{ag}) \end{aligned} \tag{2.20}$$

Combining equations. (2.19),(2.20) leads to :

$$\frac{B_r h_m}{\mu_0 \mu_r}\begin{bmatrix}1\\1\end{bmatrix} = \begin{bmatrix} \frac{1}{2}S_{st} & \frac{1}{2}(S_{\mathrm{pm,T}} + S_{\mathrm{pm,B}} + S_{ag}) \\ -\frac{1}{8}(S_{\mathrm{sp,T}} + S_{\mathrm{sp,B}}) & \frac{1}{2}(S_{\mathrm{pm,T}} + S_{\mathrm{pm,B}} + S_{ag} + \frac{1}{4}S_{\mathrm{sp,T}} + \frac{1}{4}S_{\mathrm{sp,B}}) \end{bmatrix}\begin{bmatrix}\Phi_{st}\\ \Phi_{ag}\end{bmatrix} \tag{2.21}$$

From equations (2.21), (2.18) we obtain the fluxes of the magnetic circuit :

$$\Phi_{st} = \frac{\frac{1}{8}(S_{sp,T} + S_{sp,B})}{\frac{1}{4}S_{st}(S_{pm,T} + S_{pm,B} + S_{ag} + \frac{1}{4}S_{sp,T} + \frac{1}{4}S_{sp,B}) + \frac{1}{16}(S_{sp,T} + S_{sp,B})(S_{pm,T} + S_{pm,B} + S_{ag})} \frac{B_r \cdot h_m}{\mu_0 \cdot \mu_r} \tag{2.22}$$

$$\Phi_{ag} = \frac{\frac{1}{8}(S_{sp,T} + S_{sp,B}) + \frac{1}{2}S_{st}}{\frac{1}{4}S_{st}(S_{pm,T} + S_{pm,B} + S_{ag} + \frac{1}{4}S_{sp,T} + \frac{1}{4}S_{sp,B}) + \frac{1}{16}(S_{sp,T} + S_{sp,B})(S_{pm,T} + S_{pm,B} + S_{ag})} \frac{B_r \cdot h_m}{\mu_0 \cdot \mu_r} \tag{2.23}$$

$$\Phi_{sp} = \frac{\frac{1}{4}S_{st}}{\frac{1}{4}S_{st}(S_{pm,T} + S_{pm,B} + S_{ag} + \frac{1}{4}S_{sp,T} + \frac{1}{4}S_{sp,B}) + \frac{1}{16}(S_{sp,T} + S_{sp,B})(S_{pm,T} + S_{pm,B} + S_{ag})} \frac{B_r \cdot h_m}{\mu_0 \cdot \mu_r} \tag{2.24}$$

To compute the flux densities at no load we will use equation (2.1) :

$$B_g = \frac{\Phi_{ag}}{l_m w_m} \tag{2.25}$$

$$B_{st} = \frac{\Phi_{st}}{\frac{1}{2}d_i(b_i + c_i)} \tag{2.26}$$

$$B_{sp} = \frac{\Phi_{sp}}{l_m d_i} \tag{2.27}$$

Chapter 3

Faults and Detection Methods in Permanent Magnet Synchronous Generators

3.1 Faults

Faults in permanent-magnet synchronous machines can be categorized into magnetic, mechanical and electrical types. The most common faults include inter-turn faults, partial demagnetization and both static and dynamic eccentricities. The mechanical faults are divided into eccentricity and bearing faults. The magnetic faults are demagnetization faults and the electrical faults are inter-turn faults.

Regardless of the specific fault type, their effects manifest as variations in the magnetic flux within the air gap, which can be classified as either static or dynamic. These flux imbalances serve as critical diagnostic indicators, acting as the "signature" of the fault in the machine's operation.

Faults can also be classified based on their location within the machine. For instance, inter-turn faults are typically considered "stator faults," while demagnetization and eccentricity are regarded as "rotor faults." [30]

- **Static faults**, such as inter-turn faults and static eccentricity, generate flux imbalances that remain stationary relative to the rotor's motion.
- **Dynamic faults**, including partial demagnetization and dynamic eccentricity, produce flux imbalances that vary as the rotor rotates.

This section will primarily focus on **eccentricity faults** and their impact on the C-GEN topology, while also briefly discussing other common faults for context.

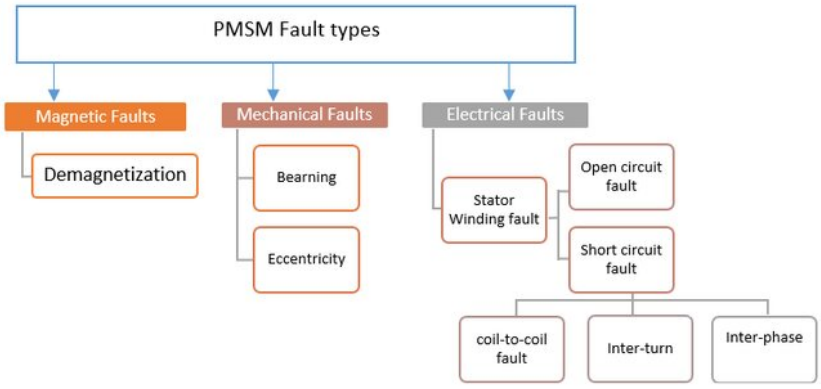

FIGURE 3.1: Categories of faults in a PMSM [31]

3.1.1 Electrical Faults

Stator winding faults are among the most frequent issues in PMSM. These faults encompass various types of short circuits, including inter-turn short-circuits, short-circuits between coils within the same phase, phase-to-phase short-circuits, phase-to-ground short-circuits and open circuits (as depicted in Figure 3.2). Of these, inter-turn short-circuits are the most common. They are primarily caused by insulation damage in the stator windings due to electrical stresses, mechanical stresses, or prolonged overload conditions [32],[33].

An inter-turn fault is an electrical fault within a machine's stator winding, whereby insulation between adjacent turns of a coil deteriorates or fails, causing a short circuit between the turns. As a result, this fault gives an uneven current distribution in the affected winding, resulting in excessive localized heating. This may cause further deterioration of insulation and, if not checked, may lead to severe failure of the machine [30].

When one turn in a coil shorts, it generates a hotspot which can be sufficient for other turns to short in a domino-effect manner, depending on the winding distribution. The more turns affected, the more likely the fault will develop into a ground fault, where at least one turn electrically connects to the stator core. Again, in C-GEN topology, the stator is iron-less and therefore, eliminating the risk of ground faults occurring in this scenario.

An inter-turn fault is considered a static fault because it occurs in a fixed location within the machine's stator winding and does not involve moving components. The schematic below illustrates various short-circuit scenarios in a Y-connected configuration.

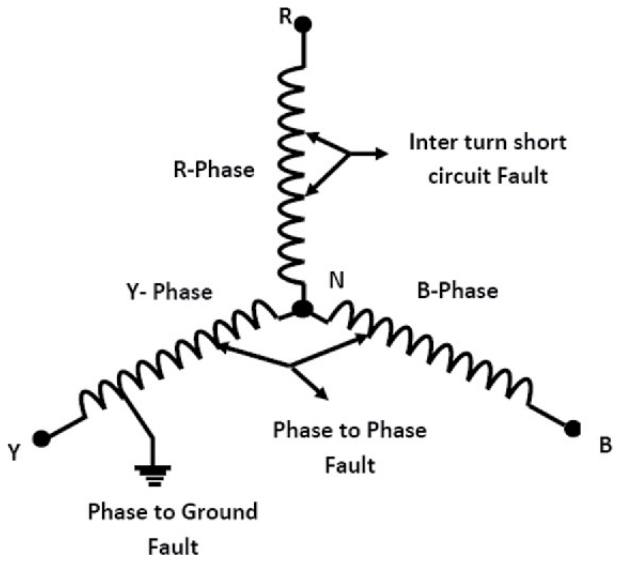

FIGURE 3.2: Schematic diagram of stator winding with different short circuit possibilities in a Y-connected configuration [34].

3.1.2 Magnetic Faults [35],[36]

The behavior of permanent magnets, like ferromagnetic materials, is described by the B-H hysteresis loop, particularly focusing on the second quadrant, known as the demagnetization curve. This curve is characteristic of the material, with key points such as B_r , representing the maximum residual magnetic flux density and H_c, the coercive force required for demagnetization. For effective performance, magnetic materials should exhibit high magnetic permeability and resistance to demagnetization.

In the case of synchronous permanent magnet machines, the operating point is given by the intersection of the magnetization curve with the load line. In the linear part, when the operating point moves slightly, one has reversible demagnetization. If the operating point is beyond the knee of the curve, demagnetization becomes irreversible and, thus the magnetic flux density of the magnet will be permanently reduced. This phenomenon is described by (Figure 3.3)

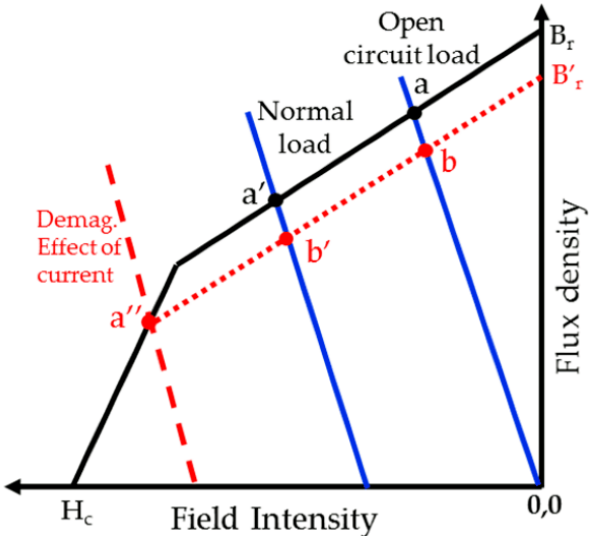

FIGURE 3.3: Operating point and demagnetization curve of PM. [36]

Despite the advantages, permanent magnet machines are subject to one of the most critical and frequent faults: irreversible demagnetization. This kind of fault can be partial or complete and is very often caused by overheating, which is usually rooted in operational inefficiency or insufficient heat dissipation. Other causes include wear and aging of magnets, reverse magnetic fields at short circuits, manufacturing defects, corrosion and mechanical or electrical stresses. Being brittle materials, permanent magnets are also susceptible to crackling during production or operation. The harsh environment with pollutants, humidity, vibrations, high temperature and overload augments the risk of demagnetization.

Demagnetization faults disrupt the magnetic flux distribution, leading to an asymmetric magnetic motive force (MMF) and a permanent loss of flux density. This reduces the generator's performance, affecting induced voltage, stator voltage and current and often generates noise and vibrations.

3.1.3 Eccentricity Faults [37, 38, 39, 40, 41]

Eccentricity faults in rotating machines are typically classified into three categories: static, dynamic and mixed eccentricity faults [37].

In the case of static eccentricity fault, the axis of rotation O_B coincides with the axis of rotor O_R but it is displaced from the stator axis O_A. Due to the displacement, the air gap becomes uneven between the rotor and stator. This entails ending up with an air gap which is not constant but has one position where it is the minimum length and another where it has the maximum length. The general causes of static eccentricity can be an oval-shaped stator core, improper alignment of the rotor or stator during manufacturing, incorrect positioning of the bearings, or wearing of the bearings during long operation.

In the case of dynamic fault, the axis of rotation O_B coincides with the stator axis O_A but not with the rotor axis O_R. The general causes of dynamic eccentricity can be rotor shaft inclination, bearing wear, mechanical resonance at critical speeds, or unbalanced magnetic pull. Misalignment causes a moving air gap with respect to the fixed stator during the rotation of the rotor, causing increased mechanical and electromagnetic stresses on the machine. Due to the attractive force between the rotor and the stator the minimum air-gap length can increase further.

A mixed eccentricity fault combines features of both static and dynamic eccentricity faults. In this case, the axis of rotation O_B is misaligned both from stator axis O_A and rotor axis O_R. Mixed eccentricity faults result in highly irregular air gaps and are typically the consequence of a combination of mechanical and manufacturing defects, such as bearing deterioration, shaft misalignment and unbalanced torque [38].

These faults may significantly affect the machine performance, causing increased vibrations, unbalanced magnetic pull, excessive noise and accelerated wear of the machine components. An improved understanding and detection of eccentricity faults is essential for ensuring reliable operation and extending the life of rotating machines. Figure (3.4) shows how stator axis O_A, rotor axis O_R and axis of rotation O_B are related to each other in cases of different eccentricity fault conditions.

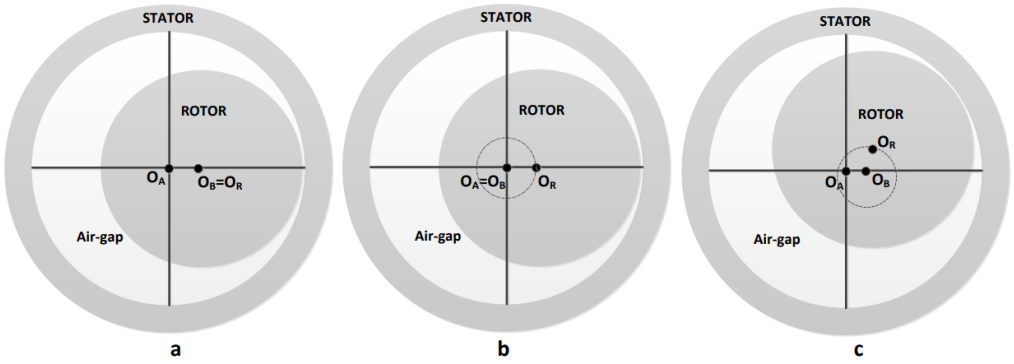

FIGURE 3.4: Eccentricity fault types: a-Static, b-Dynamic, c-Mixed. [42]

In this subsection, we will conduct a detailed analytical examination of each type of eccentricity fault and their respective impacts on C-GEN technology.

Static Eccentricity

In conventional topologies, which include a single stator and rotor, static eccentricity results in an uneven air gap length between the stator and the rotor. Due to this irregular air gap, the magnetic reluctance varies, creating an unequal distribution of magnetic flux and flux density. Consequently, the machine suffers from electromagnetic performance imbalances in its locality. In contrast, the topology of C-GEN, which is constituted of two rotors and a single stator, has a constant total magnetic air gap. The C-GEN topology has two mechanical air gaps: one between the inner rotor and the stator and another between the stator and the outer rotor. When static eccentricity occurs along the x-axis, the air gaps are affected oppositely. In particular, one of the air gaps becomes maximum in length at x-axis while the other air gap becomes minimum simultaneously. Since there is no iron core, there is no induced spatial magnetic asymmetry. Because the magnetic permeability of the windings and magnets is very close to that of air, the effective magnetic air gap extends directly from one rotor to the other, unaffected by the static eccentricity fault. No imbalance takes place in the magnetic flux or flux density, making the detection of such fault more difficult. In the following section, we will be providing a detailed proof of this phenomenon.

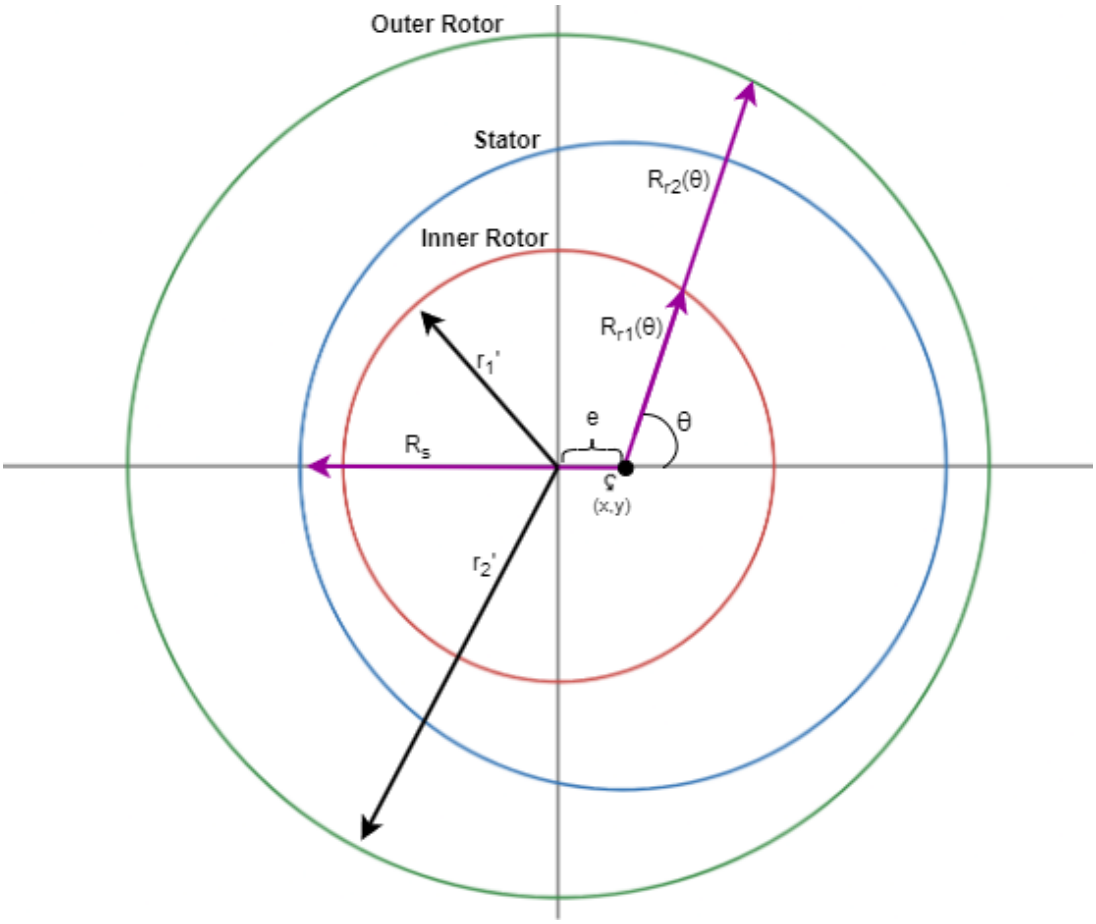

FIGURE 3.5: Static Eccentricity

The air-gap between the inner rotor and the stator is defined as g_{se1} in static eccentricity and is a function of θ.

$$g_{se1}(\theta) = R_s - R_{r1}(\theta) \tag{3.1}$$

Where:

- R_s is the radius of the stator and
- $R_{r1}(\theta)$ is the distance from the center of the stator to the inner rotor as a function of θ.

Using the equation of a circle: :

$$r_1'^2 = (x-e)^2 + y^2 \tag{3.2}$$

Where:

- r_1' is the radius of the inner rotor,
- (x, y) are the coordinates of the stator center and.
- e represents the offset between the centers of the two rotors and the stator.

We then convert equation (3.2) from Cartesian to polar coordinates and obtain:

$$\begin{aligned} r_1'^2 &= (R_{r1}cos\theta - e)^2 + R_{r1}^2 sin^2\theta \\ r_1'^2 &= (R_{r1}cos\theta)^2 - 2R_{r1}\cdot e\cdot cos\theta + e^2 + R_{r1}^2 sin^2\theta \\ r_1'^2 &= R_{r1}^2 - 2R_{r1}\cdot e\cdot cos\theta + e^2 \\ R_{r1}^2 - 2R_{r1}\cdot e\cdot cos\theta &+ (e^2 - r_1'^2) = 0 \end{aligned} \tag{3.3}$$

We will now solve the quadratic equation (3.3) to obtain R_{r1} :

$$R_{r1} = \frac{2ecos\theta \pm 2\sqrt{r_1'^2 - e^2 sin^2\theta}}{2} = e\cos\theta \pm \sqrt{r_1'^2\left(1 - \frac{(e\sin\theta)^2}{r_1'^2}\right)} \tag{3.4}$$

Because $e << r_1'$ Equation (3.4) becomes :

$$R_{r1} = ecos\theta \pm r_1' \tag{3.5}$$

Substituting Equation 3.4 to 3.1 we obtain :

$$g_{se1}(\theta) = R_s - ecos\theta \pm r_1' \tag{3.6}$$

Because $R_s - r_1' = g_1$, Where g_1 represents the air-gap between the stator and the inner rotor in the healthy case, we can modify equation (3.6) as follows:

$$g_{se1}(\theta) = g_1 - ecos\theta \tag{3.7}$$

By following the same process, the air-gap between the outer rotor and the stator is defined as g_{se2} in static eccentricity and is a function of θ.

$$g_{se2}(\theta) = R_{r2}(\theta) - R_s \tag{3.8}$$

Where:

- R_s is the radius of the stator and
- $R_{r2}(\theta)$ is the distance from the center of the stator to the outer rotor as a function of θ.

Using the equation of a circle: :

$$r_2'^2 = (x-e)^2 + y^2 \tag{3.9}$$

Where:

- r_2' is the radius of the outer rotor,
- (x, y) are the coordinates of the stator center and.
- e represents the offset between the centers of the two rotors and the stator.

We then convert equation (3.9) from Cartesian to polar coordinates and obtain:

$$\begin{aligned} r_2'^2 &= (R_{r2}cos\theta - e)^2 + R_{r2}^2 sin^2\theta \\ R_{r2} &= ecos\theta \pm r_2' \end{aligned} \tag{3.10}$$

Substituting Equation 3.10 to 3.8 we obtain :

$$g_{se2}(\theta) = ecos\theta \pm r_2' - R_s \tag{3.11}$$

Because $r_2' - R_s = g_2$, Where g_2 represents the air-gap between the stator and the outer rotor in the healthy case, we can modify equation (3.11) as follows:

$$g_{se2}(\theta) = g_2 + ecos\theta \tag{3.12}$$

The effective magnetic air-gap in the case of static eccentricity can be found by Equation (3.13). To be exact $g_{se} \approx g_{he}$ because of the approximations we took in (3.5) and (3.10), as well as the fact that the permeability of the magnets and the windings are not exactly equal to the permeability of the air.

$$g_{se} = g_{se1}(\theta) + g_{se2}(\theta) \overset{(3.7),(3.12)}{=} g_1 - ecos\theta + g_2 + ecos\theta = g_1 + g_2 = g_{he} \tag{3.13}$$

Next step is to calculate the magnetic flux density within the air-gap for the static eccentricity fault. To do that we need to also define the reluctance of the magnetic air gap as well as the MMF.

$$B_{ag} = \frac{\mathcal{F}_m}{R_{se}} \tag{3.14}$$

The reluctance of the effective magnetic air-gap can be found by :

$$\mathcal{R}_{se} = \mathcal{R}_{he} = \frac{g_{se}}{\mu_0 \mu_r A_{ag}} = \frac{\frac{t_w}{\mu_{ag}} + 2\frac{c}{\mu_{ag}} + 2\frac{h_m}{\mu_{pm}}}{\mu_0 A_{ag}} \tag{3.15}$$

Where: t_w the winding height, h_m the magnet height, c the mechanical air-gap, μ_{pm} the relative permeability of the permanent magnets, μ_{ag} the relative permeability of the air and A_{ag} the cross-sectional area of the magnetic air-gap.

Since the effective magnetic air gap length remains unchanged in both the static eccentricity and healthy cases, the air gap reluctance will also remain constant. The same stays true for the cross-sectional area of the magnetic air-gap.

The MMF developed from the permanent magnets can be expressed using Fourier series composition as follows:

$$\mathcal{F}_m(\theta, t) = \sum_{n=2m+1}^{\infty} F_{PM} \cos\left(np\theta - n\omega_s t - \phi_n\right) \tag{3.16}$$

Where : $\mathcal{F}_m$ the magneto motive force (MMF), F_{PM} the MMF Amplitude, n the harmonic order, p the pole pair number, θ the space angle, ω_s the synchronous radial frequency, ϕ_n the phase angle of the n^{th} harmonic component.

From Equations (3.14),(3.15),(3.16) we have proven that the magnetic flux density withing the air-gap stays the same for the healthy model and for the model with static eccentricity.

The magnetic flux of the air-gap will be :

$$\Phi_{ag}(t) = B_{ag} A_{ag} \tag{3.17}$$

Where : B_{ag} the magnetic flux density of the air-gap and A_{ag} the cross-sectional area of the magnetic air-gap.

Since the magnetic flux density in the air gap remains unchanged between the healthy model and the model with static eccentricity, the magnetic flux will also remain constant (Equation 3.17). Consequently, the phase voltage of the stator and so the current, become unaffected by the fault, because it is proportional to the rate of change of the air-gap magnetic flux (Faradays Law Equation 2.7). This holds true under the assumption that the system operates within the linear magnetic region, where flux density and MMF are proportional. However, C-GEN does not have a ferromagnetic core, eliminating the possibility of saturation and ensuring a constant flux-density relationship.

Dynamic Eccentricity

In conventional topologies featuring a single stator and rotor, dynamic eccentricity occurs when the rotor's center is misaligned with the common center of the stator and the axis of rotation, leading to a time-varying air gap as the rotor rotates. This variation causes fluctuations in magnetic reluctance, resulting in uneven magnetic flux distribution and flux density. These fluctuations create dynamic imbalances in the machine's electromagnetic performance, which can induce vibrations and noise and impact efficiency.

In contrast, the C-GEN topology, with its two rotors and single stator, mitigates these effects through its symmetrical configuration as was the case with the static eccentricity. We will demonstrate that, similar to the case of static eccentricity, dynamic eccentricity does not result in variations in the magnetic flux distribution, flux density, or changes in the current.

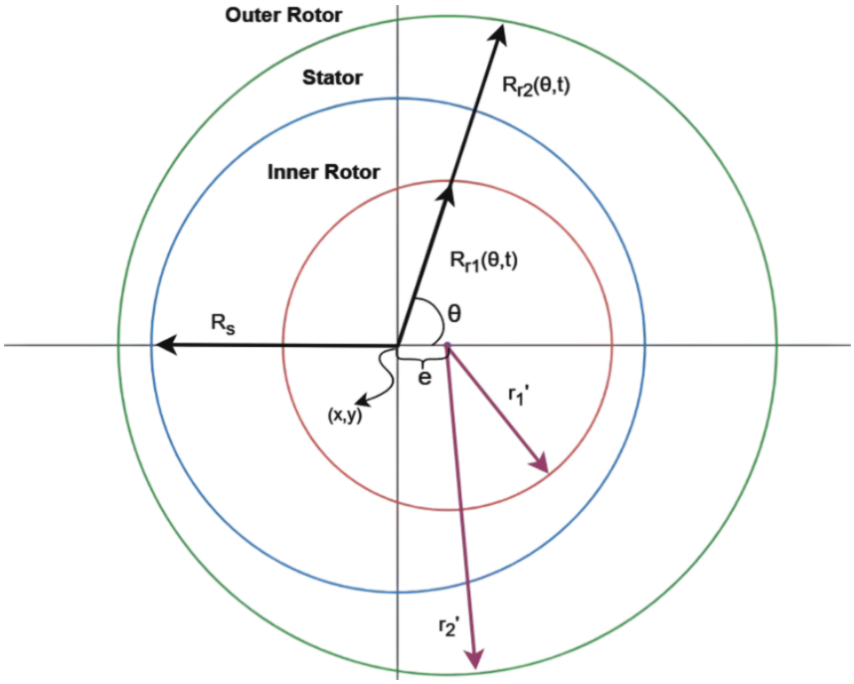

FIGURE 3.6: Dynamic Eccentricity

We will follow the same approach as in the analysis of the static eccentricity fault. However, in the case of dynamic eccentricity, g_{de1} and g_{de2} will depend not only on θ but also on ω_r and time.

g_{de1} is defined as the distance between the inner rotor and the stator and g_{de2} is the distance between the outer rotor and the stator. To calculate g_{de1} and g_{de2}, we first need to determine $R_{r1}(\theta,t)$ and $R_{r2}(\theta,t)$, which represent the distances from the stator center to the inner rotor and outer rotor, respectively. By applying the same process used for static eccentricity, starting with the equation of the circle, converting it from Cartesian to polar coordinates and solving the resulting quadratic equation, we obtain:

$$R_{r1}(\theta,t) = e \cdot cos(\theta - \omega_r t) \pm r_1' \tag{3.18}$$

$$R_{r2}(\theta,t) = e \cdot cos(\theta - \omega_r t) \pm r_2' \tag{3.19}$$

Using equations (3.18),(3.19) we can compute g_{de1} and g_{de2}.

$$g_{de1}(\theta,t) = R_s - R_{r1}(\theta,t) = R_s - ecos(\theta - \omega_r t) \pm r_1' = g_1 - ecos(\theta - \omega_r t) \tag{3.20}$$

$$g_{de2}(\theta,t) = R_{r2}(\theta,t) - R_s = ecos(\theta - \omega_r t) \pm r_2' - R_s = g_2 + ecos(\theta - \omega_r t) \tag{3.21}$$

It is important to note that e is also a function of time and ω_r. However, this dependency does not influence the final expression for the magnetic air-gap length, as the terms involving e cancel out.

$$g_{de} = g_{de1}(\theta,t) + g_{de2}(\theta,t) = g_1 + g_2 = g_{he} \tag{3.22}$$

Since the magnetic air gap remains unchanged in both healthy and faulty conditions, the magnetic flux density remains constant. So, similar to the case of static eccentricity, the phase current will remain unaffected overall. To be exact $g_{he} \approx g_{de}$ for the same reasons as the static eccentricity.

Mixed eccentricity

Mixed eccentricity is the superposition of the two other eccentricity faults, static and dynamic. Mixed eccentricity is a more realistic fault case, as a machine always has a small amount of both eccentricities. As with static and dynamic eccentricity, mixed eccentricity does not cause variations in the C-GEN magnetic air gap length. Thus, there is no change in the magnetic flux or flux density, resulting in no variations in the phase current overall.

3.2 Diagnostic Methods

Electrical machines are vulnerable to various faults, as discussed in the previous section. Research on their reliability shows that failures can occur in any component, with the risk influenced by factors such as the machine's type, design, operating conditions and application. As energy demand continues to grow, ensuring the reliability of electrical machines is crucial to enhancing both productivity and efficiency.

An early detection and analysis of faults in electrical machines before they develop into severe failures has been made possible by diagnostic methods. The processes primarily answer to the need of evolving predictive maintenance and effective fault management. This would help minimize unexpected downtime and repair costs. By monitoring machine performance and identifying early signs of wear or malfunction, diagnostic techniques play a pivotal role in maintaining operational reliability. [30]

Regardless of the specific type, a fault introduces asymmetry into the magnetic field, which then affects various electromagnetic variables, such as currents, voltages, magnetic flux, electric and mechanical power, torque and speed. By employing suitable signal processing techniques tailored to the nature of the signal, these fault-induced effects can be detected. Typically, faults manifest as unwanted harmonics or irregularities within the signal, serving as clear indicators of their presence and severity.

For several years condition monitoring of electric machines was done through offline testing, inspections and thermal or vibration analysis. Since the late 1980s, however, a fair amount of research has gone into finally developing electrical monitoring tools used to prevent in-service failure of machines and of the processes associated with them. These tools offer the advantage of remote monitoring at a lower cost, making them a more efficient and accessible solution for maintaining machine reliability [43]. Figure (3.7) depicts the diagnostic procedure.

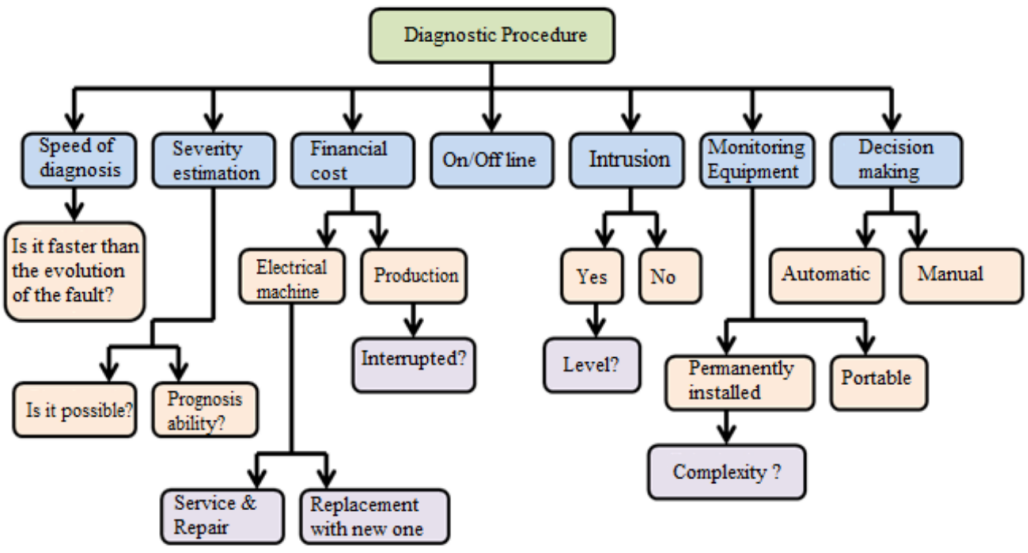

FIGURE 3.7: Diagnostic Procedure [30]

3.2.1 Motor Current Signature Analysis

Motor Current Signature Analysis (MCSA), is one of the most widespread techniques for electrical machine fault diagnosis. This method analyzes the electromagnetic phenomena through the harmonic content of the stator current. Simplicity, cost-effectiveness and the ability to remotely perform online monitoring, make it one of the most widely used techniques in diagnostics of electrical machines. This technique can be applied to multiple machines under different operating conditions and types of failures, providing conclusions about the machines condition. Identifying the unique fault-induced harmonic patterns by analyzing the spectra, enables early detection of failures, thereby preventing long downtime and improving overall system reliability.

For a typical permanent magnet machine, with one stator and one rotor, the harmonics generated by partial demagnetization and eccentricities depend primarily on the pole number of the machine and their frequencies are [39],[44] :

$$f_{fault} = (1 \pm \frac{k}{p}) f_s \tag{3.23}$$

Where k is an integer number p is the number of pole pairs and f_s is the fundamental frequency of the stator current.

Despite its wide usage range, MCSA does not come without its limitations. One limitation of MCSA is its inability to distinguish between certain faults, such as dynamic eccentricity and demagnetization in PMSM, as the fault signatures overlap and manifest at the same harmonic frequencies (Equation. 3.23) [45]. Another major disadvantage is that it can give false positive or false negative diagnostic results, which may undermine the reliability of fault detection [41]. False negatives are particularly problematic because they provide a false sense of security, delaying repairs and greatly increasing the possibility of severe damage or failure. In the case of the C-GEN topology under discussion in this thesis, the possibility of false negatives is higher in MCSA diagnostics. Due to the unique double-rotor design, this setup effectively mirrors fault-induced asymmetries between the two sides of the machine. Additionally, the absence of an iron core results in no spatial magnetic asymmetry typically used to detect faults. All these factors combined make fault detection using MCSA quite difficult for this topology.

3.2.2 Torque Monitoring

Torque monitoring is a very useful diagnostic method in PMSM. It involves the capture of the torque signal, which is representative of the operational characteristics of the machine and then applying the Fast Fourier Transform to analyze it. The torque signal can be converted into the frequency domain to identify harmonic components and oscillations that may be a symptom of certain underlying problems like eccentricity, demagnetization, or imbalanced forces [46]. It has harmonic patterns that provide important information about the condition of a machine, which helps detect anomalies at an early stage. This method also identifies torque ripples or abnormalities that affect efficiency and reliability, ensuring prompt maintenance and reducing the risk of significant mechanical failures.

Although a torque sensor can be used to directly measure the mechanical torque, its installation is sometimes too costly and impracticable for real-world applications. On the other hand, it is possible to indirectly determine the electromagnetic torque by using voltage and current readings from the machine. This method is thus far more practical and economical, especially for applications that call for continuous or remote monitoring, since no additional hardware is needed to estimate torque with a sufficient level of accuracy for diagnostic and control purposes [47],[48].

It can be found that static and dynamic eccentricity in permanent magnet synchronous machines have characteristic fault signatures at the torque signal as follows [46]:

Static eccentricity:

$$f_{se} = 2kf_s \tag{3.24}$$

Dynamic eccentricity:

$$f_{de} = f_s\left(2k \pm \frac{m}{p}\right) \tag{3.25}$$

Where:

f_s is the fundamental frequency of the system,
k is an integer multiplier (harmonic order), and
p is the number of pole pairs in the machine.

3.2.3 Magnetic Flux Analysis

Flux monitoring is an widely used diagnostic technique that analyzes the harmonic content of the flux in a machine, using Fast Fourier Transform (FFT). This method is primarily divided into two categories: airgap flux monitoring and stray flux monitoring. Stray flux monitoring is a non-intrusive, low-cost method that has the ability to be applied to machines already in operation, offering a valuable on-line monitoring solution [49]. This method serves as a valuable asset in the diagnostics field, as it is capable of differentiating among various fault conditions. Nevertheless, the placement of sensors outside the machine, which only captures weaker flux signals, presents limitations for stray flux monitoring, particularly in terms of reduced sensitivity. Conversely, airgap flux monitoring excels in identifying defects due to its high fault sensitivity and diagnostic dependability. However, the installation of sensors requires physical intervention, rendering it intrusive [43].

One of the main advantages of flux monitoring over more traditional techniques, such as Motor Current Signature Analysis, MCSA, is that flux monitoring can offer a wide spectrum of harmonic content with more precise information about the state of the machine. Since the current is related to the flux, MCSA signals can also be found in the radial flux spectrum. In MCSA on the other hand, harmonics like the 3rd and its multiples are effectively canceled out because of the circuit Y-connection. Another key advantage of the airgap flux monitoring is that it remains unaffected by load defects [43]. Airgap flux monitoring captures the flux directly caused by rotor-stator interaction, offering a clearer and more accurate indication of machine health. This makes it particularly useful in applications where load conditions are variable or difficult to control.

3.2.4 Diagnostics using two magnetically coupled search coils [50],[51]

The described method is a novel diagnostic tool designed to detect various faults in permanent magnet machines using the air-gap flux monitoring technique. It employs two magnetically coupled coils: one placed in the rotor air gap and another on the stator. These coils are strategically configured, with the rotor search coil short-circuited and the stator search coil left open-circuited. Both coils share the same pitch and are designed to span the minimum number of odd coil pitches and even poles.

In a healthy machine, the magnetic flux across the air gap is symmetric, resulting in no current in the rotor search coil and, consequently, no induced voltage in the stator search coil. However, when a static fault occurs, such as static eccentricity in the C-GEN topology, the situation changes. Although the total air-gap flux remains constant, local variations in reluctance

due to misaligned stator-rotor positioning cause the flux per coil to differ. These variations are static, but because the rotor is in motion, a time-varying voltage is induced in the rotor search coil, leading to a current. This current generates an MMF, producing an air-gap magnetic field that induces a time-varying flux in the stator search coil, resulting in an observable voltage. This voltage is increased monotonically with the severity of the fault.

For dynamic faults, the rotor search coil is unnecessary. This is because dynamic variations inherently cause time-varying magnetic flux, directly inducing a voltage in the stator search coil. Thus, this diagnostic tool is capable of detecting both static and dynamic faults. However it is a very intrusive method, especially for the search coil that is placed on the rotor.

3.2.5 Zero-Sequence-Flux [52],[53],[54]

The zero-sequence flux method is a technique based on the airgap flux monitoring method. In this approach, three flux sensors are installed in the healthy stator, spaced 120 electrical or mechanical degrees apart. These sensors detect the flux density, which exhibits a phase difference of 120° in time. According to Faraday's Law of Induction, the sensor output voltages will be proportional to the flux.

The mathematical representation of the induced sensor voltages is given by:

$$V_a = \sum_{n=1}^{\infty} V_n \cos(n\omega t), \tag{3.26}$$

$$V_b = \sum_{n=1}^{\infty} V_n \cos\left(n\omega t - \frac{2\pi}{3}\right), \tag{3.27}$$

$$V_c = \sum_{n=1}^{\infty} V_n \cos\left(n\omega t + \frac{2\pi}{3}\right). \tag{3.28}$$

When the three signals are summed, the resulting voltage is expressed as:

$$V_{ZS} = V_a + V_b + V_c = \sum_{k=3(2m+1)} 3V_k \cos(k\omega t), \tag{3.29}$$

where the summation cancels out harmonics of frequencies $(6k \pm 1)f_s$ (e.g., 1st, 5th, 7th harmonics). These are the same harmonics typically observed in the stator current spectrum. However, the odd triplets (e.g., 3rd, 9th, etc.) remain in the zero-sequence flux, with the fundamental of the zero-sequence component occurring at $3f_s$.

Static Faults

When a static fault occurs like static eccentricity, local variations in reluctance due to misaligned stator-rotor positioning cause the flux per coil to differ among the three sensors. As a result, the amplitudes of the three induced voltages are no longer equal, and their summation no longer cancels out the $(6k \pm 1)f_s$ harmonics. The amplitudes of these harmonics increase monotonically with the severity of the fault, making it a clear indicator of static faults.

Dynamic Faults

In the case of dynamic faults, the three sensors detect flux signals with equal amplitudes and with a 120° phase difference. For example in dynamic eccentricity, the rotor's motion creates time-varying changes in the flux per coil. However, these changes occur uniformly across the three sensors, leading to the same signal being detected with only a phase shift of 120°. This symmetry means that harmonics at $(6k \pm 1)f_s$ (e.g., 1st, 5th, 7th harmonics) still cancel out, as in the healthy condition. However, dynamic eccentricity induces time-varying variations in

the flux of each coil, which repeat every full rotation of the machine. These variations create sideband harmonics around the main frequencies $(6k \pm 1) f_s$ as well as the 3^{rd} harmonic. These sidebands occur at multiples of the mechanical frequency.

Advantages of Zero-Sequence Flux Analysis

The zero-sequence component (ZSC) has a fundamental frequency of $3f_s$, which results in a higher signal amplitude compared to the individual sensor outputs. This enhanced amplitude improves signal quality, making it easier to process and analyze. Consequently, the method allows for more accurate detection of faults. The method also is able to detect both static and dynamic faults and differentiate between them.

Chapter 4

Finite Element Method and Model Creation

4.1 The Finite Element Method (FEM)

The **Finite Element Method (FEM)** is a numerical technique widely used to solve complex engineering and physical problems governed by partial differential equations (PDEs). Its strength lies in its ability to handle intricate geometries, non-linear material properties, and complex boundary conditions.

FEM works by dividing the domain into smaller regions called finite elements, interconnected at discrete points known as nodes. Within each element, the solution is approximated using simple functions, typically polynomials, called shape functions. The overall solution is obtained by assembling these local solutions into a global system [55].

4.1.1 FEM and Electrical Machines [56],[57]

It is nearly impossible to discover an analytical solution to the governing equations for issues like those found in the study of electrical machines. The goal is to convert the problem's continuous model into a discrete one so that a computer can solve it. Significant simplifications are frequently needed when using analytical methods, particularly when dealing with complex geometries like those found in electrical devices. In certain situations, numerical techniques like FEM yield more dependable findings.

Because they use a limited set of points to approximate the continuous domain, these techniques are frequently called approximation methods. However by increasing the computational effort it is possible to increase accuracy to the necessary level. For the study of electrical machine models, FEM is the method of choice due to its versatility and precision. While it may be considered approximate, FEM often provides more reliable results than equivalent circuit analysis. Additionally, FEM can be applied to any problem, regardless of its complexity.

The Finite Element Method (FEM) is a very important tool used for diagnostics of electrical machines, because it allows insight into operational behavior. Its capability for accurate modeling of complex geometries and nonlinear material properties is very important for identifying deviations from normal performance, which may be indicative of the presence of faults. FEM enables the analysis of phenomena such as electromagnetic field distortions, thermal anomalies, and mechanical stresses, all of which are vital for detecting issues like insulation failure, rotor eccentricity, or winding faults. By simulating these conditions with high precision, FEM supports the development of advanced diagnostic techniques, facilitating early fault detection and improving the reliability of predictive maintenance systems. This could address potentially upcoming problems before they could seriously make severe failures occur.

Despite its strengths, FEM faces some challenges:

- **Data Availability:** Accurate geometric and material data may not always be accessible, limiting the precision of results.
- **Computational Cost:** As problem complexity increases, so does the required computational time and resources.
- **Setup Complexity:** Preparing the model, generating a mesh, and defining boundary conditions require expertise and time.

4.1.2 FEM Implementation via Software

Finite Element Method (FEM) software facilitates the simulation and analysis of complex engineering problems by automating key aspects of the method. These tools streamline preprocessing tasks such as defining geometries, assigning material properties, and specifying boundary conditions. The domain is discretized into finite elements through automated mesh generation, which significantly influences the accuracy and efficiency of the solution. Solvers embedded within the software handle the computational demands of solving large systems of equations, while postprocessing tools allow users to visualize results and generate detailed plots for analysis.

FEM simulations can be conducted using either a linear or nonlinear approach, depending on the complexity of the problem and the material behavior. In a linear analysis, the software assumes constant material properties, such as a fixed relative permeability, as specified by the user. This approach simplifies the computation but may overlook important phenomena like magnetic saturation. Nonlinear analysis, on the other hand, incorporates the material's B-H curve, enabling the simulation to account for changes in material properties under varying magnetic fields. This results in a more realistic representation of physical behavior, particularly in applications involving electromagnetic fields.

4.1.3 Equations Used in FEM [56],[58]

The selection of equations in Finite Element Method (FEM) depends on the nature of the problem being analyzed, which typically falls into two categories: magnetostatic and harmonic problems. Magnetostatic problems involve time-invariant quantities, while harmonic problems deal with time-varying sinusoidal quantities. The governing equations are derived from Maxwell's equations, tailored to the specific characteristics of the problem.

Magnetostatic Problems

In magnetostatic problems, the magnetic field intensity $\mathbf{H}$ and the magnetic flux density $\mathbf{B}$ are connected through Maxwell's equations:

$$\nabla \times \mathbf{H} = \mathbf{J} \tag{4.1}$$

$$\nabla \cdot \mathbf{B} = 0 \tag{4.2}$$

where $\mathbf{J}$ is the current density. For a given material, $\mathbf{H}$ and $\mathbf{B}$ are related by the magnetic permeability μ:

$$\mathbf{B} = \mu \mathbf{H}. \tag{4.3}$$

The magnetic vector potential $\mathbf{A}$ is introduced such that:

$$\mathbf{B} = \nabla \times \mathbf{A}. \tag{4.4}$$

Substituting (4.4),(4.3) into (4.1) yields the governing equation:

$$\nabla \times (\frac{1}{\mu(B)} \nabla \times \mathbf{A}) = \mathbf{J}, \tag{4.5}$$

which, in the case of a linear and isotropic medium, simplifies to:

$$-\frac{1}{\mu} \nabla^2 \mathbf{A} = \mathbf{J} \tag{4.6}$$

Harmonic Problems

For harmonic problems, where the magnetic fields vary with time, eddy currents are induced in materials with conductivity σ. The current density $\mathbf{J}$ is related to the electric field intensity $\mathbf{E}$ by:

$$\mathbf{J} = \sigma \mathbf{E}. \tag{4.7}$$

Maxwell's equation for a time-varying magnetic field is given by:

$$\nabla \times \mathbf{E} = -\frac{\partial \mathbf{B}}{\partial t}. \tag{4.8}$$

Substituting (4.4) into (4.8) results in:

$$\nabla \times \mathbf{E} = -\frac{\partial (\nabla \times \mathbf{A})}{\partial t}. \tag{4.9}$$

Combining (4.7) and (4.9) into (4.6) yields the time-dependent governing equation:

$$-\frac{1}{\mu} \nabla^2 \mathbf{A} + \sigma \frac{\partial \mathbf{A}}{\partial t} = \mathbf{J}. \tag{4.10}$$

Motion Analysis

In problems involving rotating machines under load, the equation of motion is also considered:

$$J \frac{\partial^2 \theta}{\partial t^2} = T, \tag{4.11}$$

where J is the moment of inertia, θ is the angular position, and T is the torque. The total torque T is the sum of electromagnetic torque T_{Em}, load torque T_{L}, and friction torque T_{F}:

$$T = T_{\text{Em}} + T_{\text{L}} + T_{\text{F}}. \tag{4.12}$$

2D Problems

For two-dimensional problems, only the axial component of the magnetic vector potential $\mathbf{A}$ is considered, simplifying the analysis significantly. These equations form the mathematical foundation for solving FEM problems, enabling the simulation of magnetic, electric, and mechanical phenomena in complex systems.

4.2 C-GEN Tutorial - Simcenter MAGNET [59]

This section focuses on the simulation and modeling characteristics of a radial flux air-cored permanent magnet synchronous generator, a part of the innovative C-GEN technology. The generator's primary rated characteristics, are outlined in the following table.

Table 4.1. Generator Characteristics

Parameter	Value
Rated Power	21.5 kW
Rated Speed	100 rpm
Stator	Coreless
Frequency	26.67 Hz
Pole Pairs	16
Stator Coils	24 × Single Concentrated
Stator Coil Turns	205
Magnet Material	N42 Recoil NdFeB

The initial step after launching **Simcenter MAGNET** is to create a new `.mn` project and configure the length unit to millimeters (`mm`). To accomplish this, navigate to **Tools**, select **Set Units**, and under the **Length** section, choose **Millimeters** from the dropdown menu. To design the machine's outline, it is essential to enable the **Keyboard Input Bar**. This can be done by navigating to the **Tools** menu and activating the option.

4.2.1 C-GEN Outline Design

Inner and Outer Rotor Outline

The next step is to design the outlines of the inner and outer rotors. These outlines are not circular, as the inner and outer rotors consist of steel components that are trapezoidal in shape. We will first design the outline of the outer rotor, followed by the inner rotor using the same process.

For the outer rotor, we begin by drawing a line that represents the long base of the trapezoidal steel (length b_i). To draw this line, navigate to **Draw** → **Add Line**, and specify the two endpoints in Cartesian coordinates. Specifically, set the start point to $(-b_i/2, 0)$ and the end point to $(b_i/2, 0)$.

Next, click on **Edit**, select **Select Construction Slice Edges**, and choose the line that was drawn. Once the line turns red, navigate to **Draw** → **Shift Edges**, and input the coordinates of the desired shift point. In this case, input $(0, r_{bi})$, where r_{bi} represents the radius from the machine center to the outermost point of the outer rotor.

With the shifted line selected, navigate to **Draw** → **Rotate Edges**. Set the rotation angle to $\frac{360}{32} = 11.25°$, as there are 32 steel modules in the rotor and the machine spans 360°. Then, set the **Number of Copies** to 31. This process completes the design of the outer outline of the outer rotor.

To design the inner outline of the outer rotor, we follow the same process, but use c_i (the short base of the trapezoidal steel module) and r_{ci} (the radius from the machine center to the inner edge of the steel module).

The exact same process is used to design the outline of the inner rotor. However, instead of using b_i, c_i, r_{bi}, and r_{ci}, we now use b_{ii}, c_{ii}, r_{bii}, and r_{cii}. Here, b_{ii} and c_{ii} represent the long and short bases of the trapezoidal steel modules for the inner rotor, respectively, while r_{bii} and r_{cii} correspond to the radii from the center of the machine to the outermost and innermost points of the inner rotor.

By following this method, the outlines of both the inner and outer rotors are completed, ensuring that their geometric design accurately reflects the trapezoidal steel module configurations.

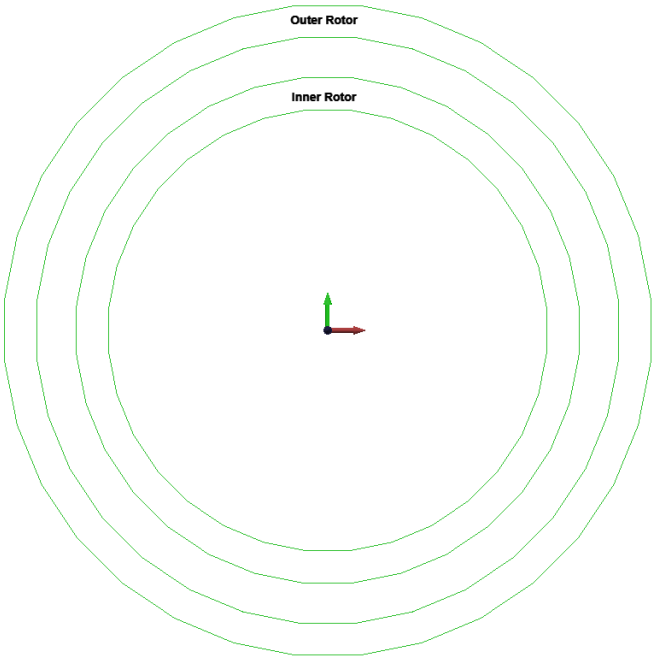

Figure 4.1. Inner and Outer Rotor Outline

Inner and Outer Rotor Magnets Outline

The next step is to design the outlines of the inner and outer permanent magnets of the machine. We will begin with the outer rotor permanent magnets. The permanent magnets have a rectangular shape, which can be represented by drawing four lines.

1. The first line is drawn from $(-w_{\text{pm\_out}}/2, 0)$ to $(w_{\text{pm\_out}}/2, 0)$, where $w_{\text{pm\_out}}$ is the width of the outer rotor permanent magnet.
2. The second line is drawn from $(-w_{\text{pm\_out}}/2, 0)$ to $(-w_{\text{pm\_out}}/2, -h_m)$, where h_m is the height of the magnet.
3. The third line is drawn from $(-w_{\text{pm\_out}}/2, -h_m)$ to $(w_{\text{pm\_out}}/2, -h_m)$.
4. The final line is drawn from $(w_{\text{pm\_out}}/2, -h_m)$ to $(w_{\text{pm\_out}}/2, 0)$.

By connecting these four lines, the rectangular shape of the outer rotor permanent magnets is completed. Next, select the four lines and navigate to **Draw** $\rightarrow$ **Shift Edges**, shifting them to the point $(0, r_{ci})$. Then, use **Draw** $\rightarrow$ **Rotate Edges**, setting the rotation angle to 11.25° and the **Number of Copies** to 31.

This process completes the outline of the outer rotor permanent magnets, which are positioned on the inner surface of the outer rotor.

For the inner rotor permanent magnets, the same process is followed, with the difference that the width of the permanent magnets is smaller ($w_{\text{pm\_in}}$), and the magnets are placed on the outer surface of the inner rotor. Therefore, when selecting the **Shift Edges** option, the shift point is set to $(0, r_{bii} + h_m)$, where r_{bii} represents the radius to the outer surface of the inner rotor.

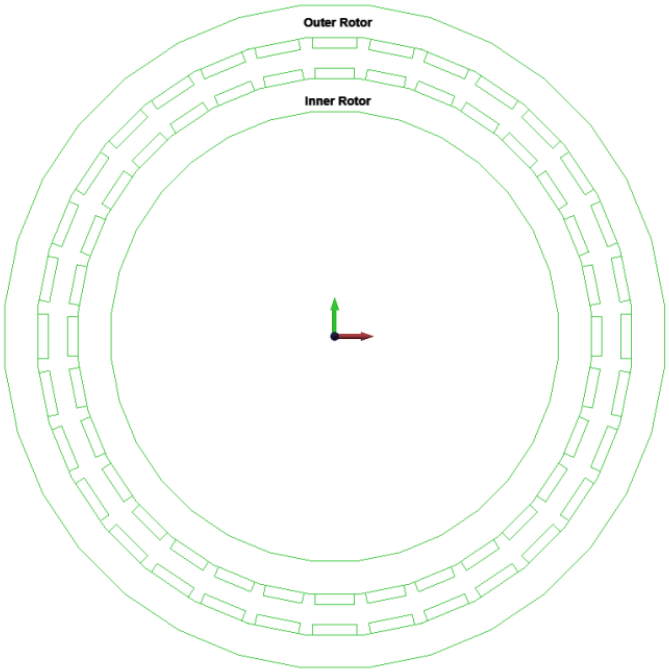

Figure 4.2. Inner and Outer Rotor Permanent Magnets Outline

Stator Outline

The stator consists of 24 concentrated windings. In slotless machines, the stator lacks conventional slots to house the windings. Instead, the coils are placed in the air-gap region between the inner and outer rotors. Each coil has an input and output, separated by an air-gap.

To create the stator coil outline, the following lines are drawn:

1. The first line is drawn from $(-w_{\text{c}}/2, 0)$ to $(w_{\text{c}}/2, 0)$, where w_{c} represents the width of the coil, including the air-gap between the input and output of the coil.
2. The second line is drawn from $(-w_{\text{c}}/2, 0)$ to $(-w_{\text{c}}/2, -t_w)$, where t_w is the height of the winding.
3. The third line is drawn from $(-w_{\text{c}}/2, -t_w)$ to $(w_{\text{c}}/2, -t_w)$.
4. The fourth line is drawn from $(w_{\text{c}}/2, -t_w)$ to $(w_{\text{c}}/2, 0)$.
5. The fifth line is drawn from $\big(-w_{\text{c}}/2 + w_{\text{c\_end}}, -t_w\big)$ to $\big(-w_{\text{c}}/2 + w_{\text{c\_end}}, 0\big)$, where $w_{\text{c\_end}}$ is the width of each coil input and output.
6. The final line is drawn from $\big(w_{\text{c}}/2 - w_{\text{c\_end}}, -t_w\big)$ to $\big(w_{\text{c}}/2 - w_{\text{c\_end}}, 0\big)$.

After drawing these lines, select them and navigate to **Draw** $\rightarrow$ **Shift Edges**, shifting the coil to the point $(r_{\text{ci}} - h_m - c, 0)$, where c is the mechanical air-gap between the stator and the rotor. Finally, after selecting the coil lines, we navigate to **Draw** $\rightarrow$ **Rotate Edges**, and set the rotation angle to $\frac{360}{24} = 15^\circ$, as there are 24 windings in the stator and the machine spans 360°.

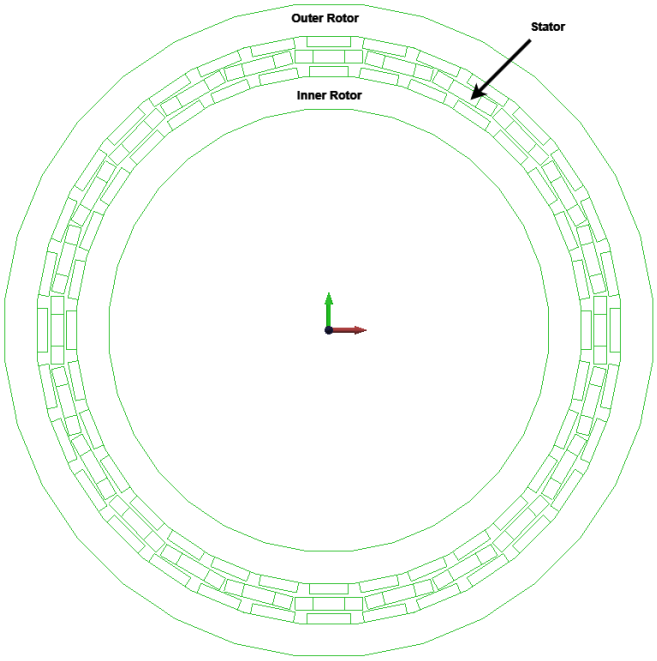

Figure 4.3. Stator Outline

Air-gap Layers Outline

The **C-GEN** design features two air-gaps: one between the inner rotor and the stator, and another between the outer rotor and the stator. Each of these air-gaps is divided into three distinct sub-layers, each with specific roles and characteristics:

1. **Rotor-Side Layer**: The layer closest to the rotor is part of the simulation's motion component, capturing the dynamic interaction between the rotating rotor and the stator.
2. **Middle Layer**: This layer is modeled as a standard ring, representing the typical separation between the rotor and stator.
3. **Stator-Side Layer**: The layer adjacent to the stator accounts for both air and insulation, serving a dual-purpose function. Notably, this layer is shared between the inner and outer air-gaps.

To construct these layers, four circles were drawn: two for the air-gap between the outer rotor and the stator, and two for the air-gap between the inner rotor and the stator. These circles define the boundaries of the sub-layers described earlier. It is crucial to ensure that these circles do not physically intersect or connect with any components of the stator or rotors.

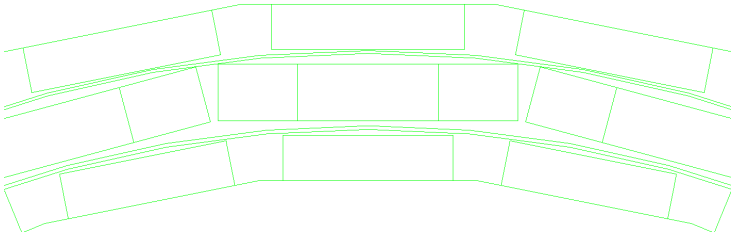

Figure 4.4. Air-gap layers Outline

C-GEN Complete Outline

To finalize the outline of the C-GEN, an external air layer was added around the machine. This layer simulates open-space conditions, enhancing the accuracy and realism of the simulation.

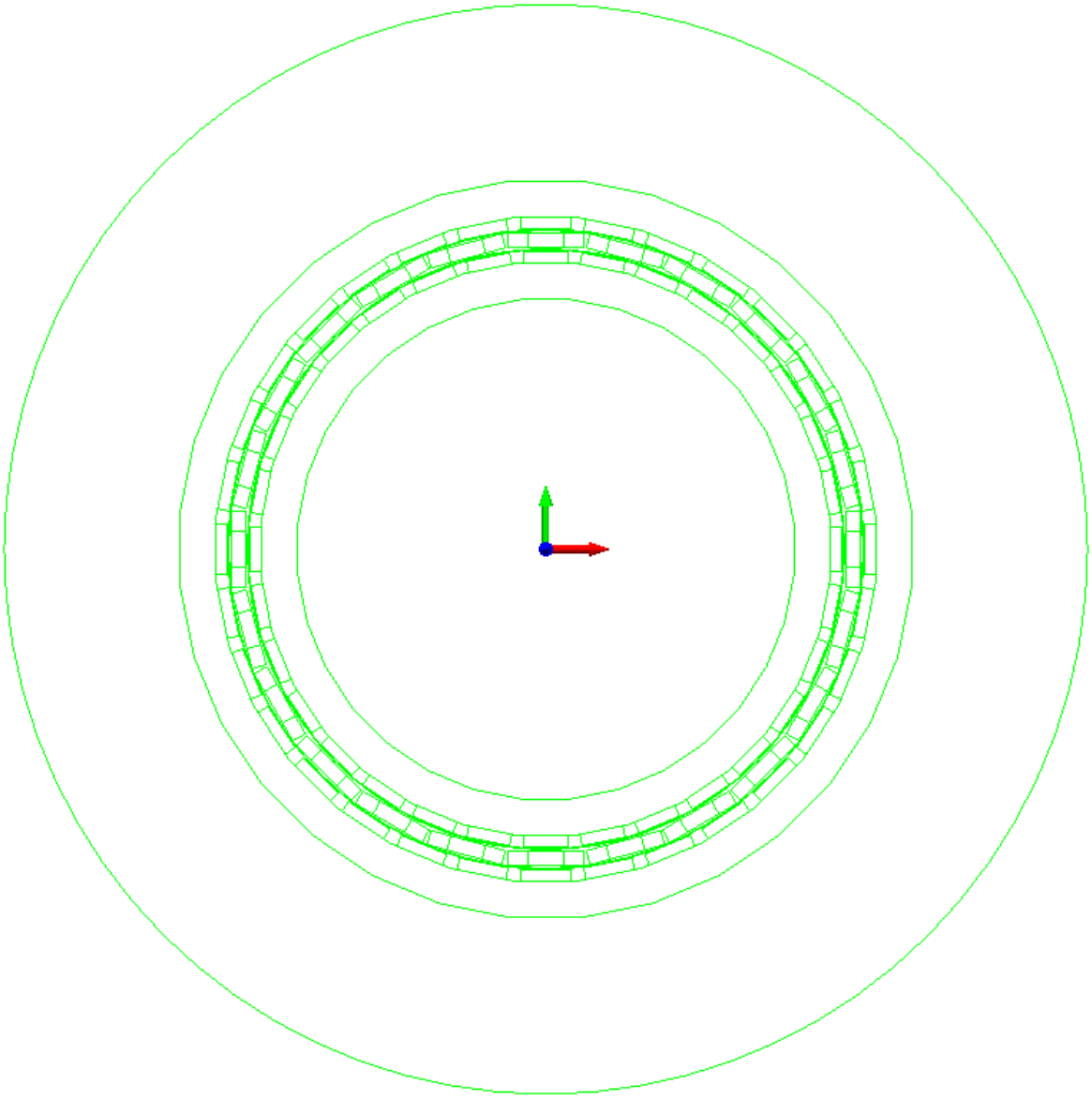

Figure 4.5. C-GEN Outline

4.2.2 C-GEN Component Creation

The next step in the model creation process is to define the components and assign the appropriate materials to them.

Rotor Components

To create the rotor components, follow these steps:

1. Navigate to **Edit** → **Select Construction Slice Surfaces** and select one of the rotors.
2. Go to **Model** → **Make Component in Line**.
3. In the dialog box, specify the component's name, its axial length (Distance), and the material.

Repeat the same process for the other rotor. Both rotors share the same axial length and are made of the same steel material.

Magnet Components

The model includes 32 inner magnets and 32 outer magnets, all created from N42 material. The magnets are categorized into two types, **South** and **North**, depending on their magnetization direction.

We begin by defining the outer rotor magnets. Adjacent magnets alternate between South and North polarities.

1. Navigate to **Edit** → **Select Construction Slice Surfaces** and select one of the outer magnets.
2. Go to **Model** → **Make Component in Line**.
3. In the dialog box, specify the component's name, its axial length (**Distance**), and the material. Since the material is magnetic, also define its magnetization direction.
4. Select the newly created magnet component and navigate to **Model** → **Rotate Components**. Set the rotational angle to 11.25° and the number of copies to 31.
5. As mentioned earlier, the magnets alternate between South and North polarities. For half of the magnets, change the magnetization direction by reversing the signs of x and y in the **Direction** box. Additionally, override the material color: use red for North magnets and blue for South magnets.

The same process is followed for the magnets in the inner rotor. Keep in mind that magnets positioned opposite each other in the inner and outer rotors alternate between South and North polarities.

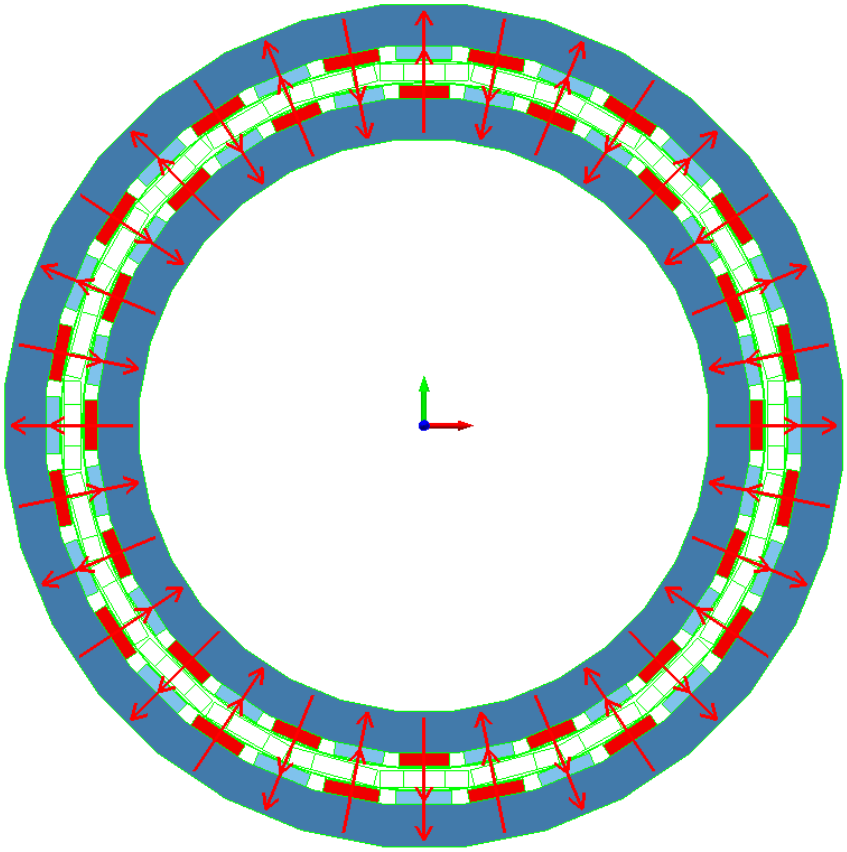

Figure 4.6. Creation of Magnets Component

Coil Components

The model includes 24 concentrated coils, each with an input and an output. All coils are made of copper.

To define the coils, we follow these steps:

1. Select one coil end using **Edit** → **Select Construction Slice Surfaces**.
2. Navigate to **Model** → **Make Component in Line** and specify the material as copper, with a conductivity of 5.77×10^7 Siemens/meter.
3. Select the newly created coil end component using **Edit** → **Select Components**.
4. Use **Model** → **Rotate Components**, setting the rotational angle to ensure that all coil end positions are filled with the copper component.

At this stage, only the material of the coils has been specified. The next step is to create the coils themselves. To do that we follow these steps:

1. Select both the input and output of a coil.
2. Navigate to **Model** → **Make a Simple Coil**.
3. Right-click on the newly created coil and select **Properties**.

4. In the **Properties** dialog box, we define the following parameters:
    - **Number of Turns**: Specify the number of turns in the coil.
    - **Strand Area**: Enter the cross-sectional area of the coil strands.
    - **Additional Resistance**: Specify any additional resistance in the coil.

    We repeat this process for all coils.

To distinguish between the three phases of the coils, we modify the colors of the coil end components as follows: **Phase A** coils are colored brown, **Phase B** coils are colored yellow, and **Phase C** coils are colored grey.

Lastly, we need to define the air-gap between each coil input and output. To do this, we follow these steps:

1. Select the outline of one of the coil air-gaps using **Edit** → **Select Construction Slice Surfaces**.
2. Navigate to **Model** → **Make Component in Line** and specify the name of the component and set the material to **AIR**.
3. Use **Model** → **Rotate Components**, setting the rotational angle to 15° to create all the air-gap components for the rest 23 coils.

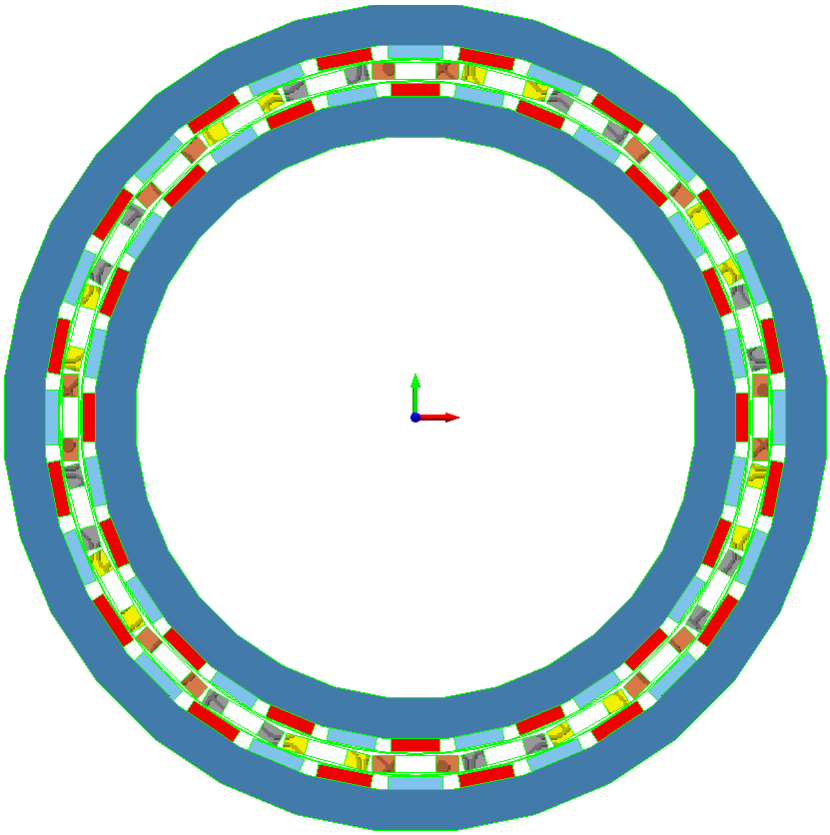

Figure 4.7. Creation of Coil Components

Air gap Layers Components

The next step is to define the air-gap layers described earlier. The two layers closest to the rotors (**Rotor-Side Layers**) are assigned the material **Virtual Air**. The two middle layers are assigned the material **AIR**, as is the common stator air-gap layer.

To define the materials for these components, we follow these steps for each layer:

1. Select the desired layer using **Edit** → **Select Construction Slice Surfaces**.
2. Navigate to **Model** → **Make Component in Line**.
3. Specify the component's name and assign the appropriate material (**Virtual Air** or **AIR**).

Lastly, for the external air layer that was added around the machine we select the AIR material.

Motion Components

We define three motion components, one for each of the moving parts. These motion components include various components described earlier to determine the motion of each group:

- **Inner Motion**: This motion component includes:
  - The 32 Inner Rotor Magnets
  - The inner rotor-side air gap
  - The Inner Rotor Core
- **Stator Motion**: This motion component includes:
  - All the coils
  - All the air gaps between the coils
  - The Stator Air Gap
- **Outer Motion**: This motion component includes:
  - The 32 Outer Rotor Magnets
  - The outer rotor-side air gap
  - The Outer Rotor Core

The **Outer Motion** and **Inner Motion** components are velocity-driven, utilizing rotary motion at a speed of 100 rpm. In contrast, the stator components remain stationary, with a rotational speed of 0 rpm.

To create a motion component, we follow these steps:

1. Select all the components included in the motion component.
2. Navigate to **Model** → **Make Motion Component**.
3. Open the properties of the newly created motion component and define its **Source Type** and **Motion Type**.
4. To specify the speed, go to the **Position** tab, select **Speed Based** from the drop-down menu, and input the required values for **Time** and **Speed** in *radians per second (rad/s)*.

Sensor Components

To calculate the zero-sequence flux and implement the flux monitoring technique, sensors were placed across the machine. Specifically, these sensors were positioned in every air-gap of the coils, resulting in a total of 24 sensors—equal to the number of coils in the machine. These sensors are essentially copper coils, each with 100 turns per coil.

To create a sensor, we follow these steps:

1. Draw two squares at equal distances from the input and output of one coil using **Draw** → **Add Line**.
2. Use **Edit** → **Select Construction Slice Surfaces** to select the surfaces of the drawn squares.
3. Navigate to **Model** → **Make Component in Line**, assign the material as **Copper**, and provide a name for each end of the coil.
4. Use **Model** → **Rotate Components**, set the rotational angle to 15°, and specify the number of copies as 23 to place the remaining sensors.
5. Select the input and output components of one sensor coil and navigate to **Model** → **Make Simple Coil**.
6. In the properties of the newly created coil, set the **Number of Turns** to 100.

Repeat 5,6 steps for each sensor coil in the air-gap between the coils to complete the placement of all 24 sensors.

In addition to these sensors, two search coils must also be placed within the machine: one in the rotor and one in the stator air-gap. Each search coil spans 180° and consists of a single turn.

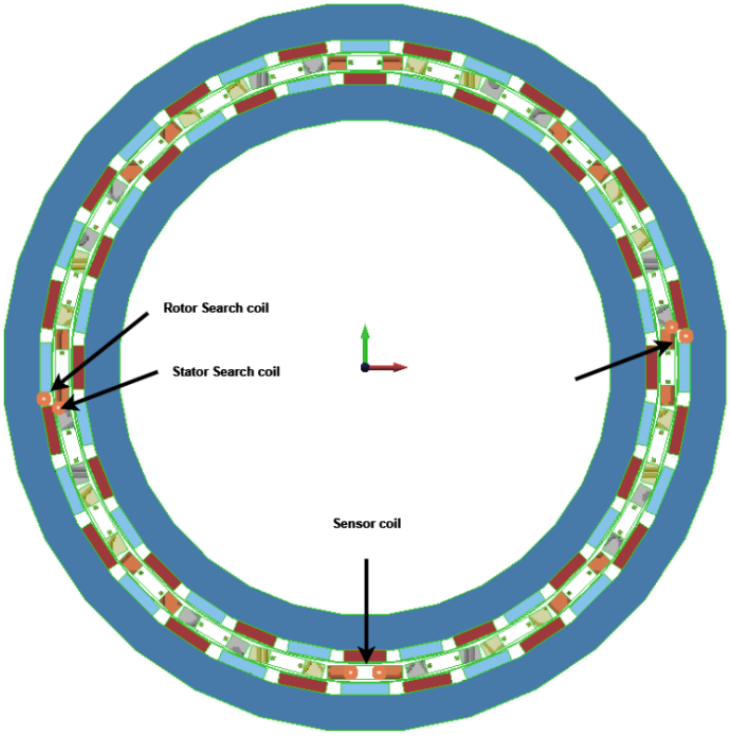

Figure 4.8. Creation of Sensor Coil Components

4.2.3 Circuit Creation

Each phase consists of 8 coils, resulting in a total of 24 coils across the 3 phases. In each phase, 4 coils are connected in parallel, and these parallel groups are then connected in series with the other 4 parallel coils. This configuration is applied to all three phases. The circuit is connected in a **Y-configuration**, and the 3-phase Ohmic load, also in a **Y-connection**, includes 3 resistors, each with a resistance of 17.5 Ω.

All 24 sensors must be open-circuited. To achieve this, each sensor coil is connected to a 1 GΩ resistor. The same configuration is applied to the stator search coil. Conversely, the rotor search coil is short-circuited.

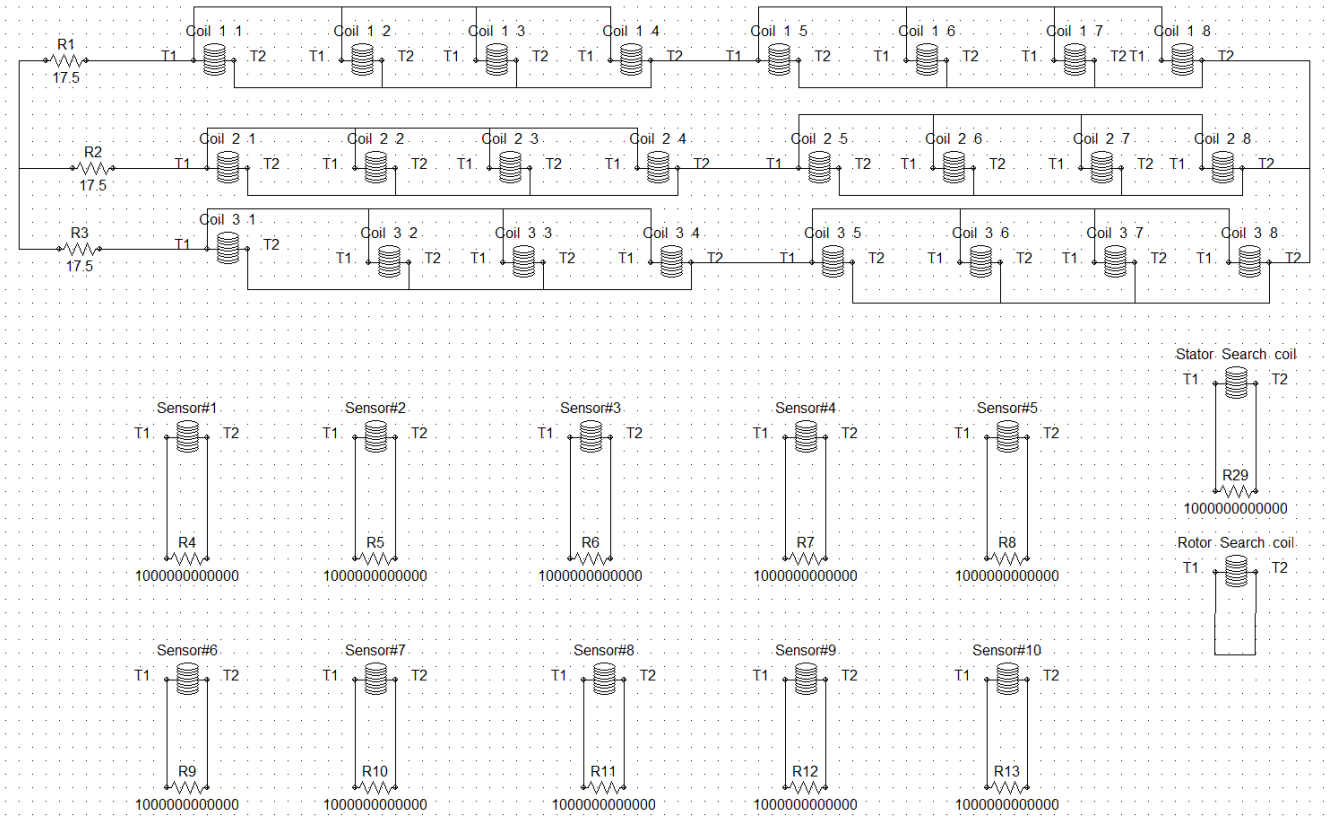

Figure 4.9. Circuit Design

4.2.4 Simulation Solver

The final step is to run the simulation. First, we need to configure the simulation parameters, including the start time, stop time, and time step. For this case, the simulation will run for 4 seconds (4000 ms) with a sampling frequency of 6 kHz, corresponding to a time step of 0.167 ms.

To set these parameters, navigate to **Solve** → **Set Transient Options**, and input the desired values. Once the settings are configured, the simulation can be started by going to **Solve** → **Transient 2D with Motion**.

4.2.5 Obtain Results

After the solver has completed, the results are post-processed using MATLAB. To do this, the required results are exported as an Excel file and imported into MATLAB. The first step in analyzing a healthy machine after solving is to verify that the experimental [60] and simulation results are in agreement. In our case, the comparison is as follows:

Table 4.2. Comparison of Simulation (FEM) and Experimental Results

Variable	**FEM**	**Experiment**
Phase Voltage (V)	300.74	306.7
Stator Current (A)	17.18	17.41
Torque (Nm)	1567	1575
Output Power (kW)	15.5	15.4
Input Power (kW)	16.41	16.5

Chapter 5

Study Results and Analysis

5.1 Study Case

For the purpose of this thesis, a total of 30 simulations were conducted, comprising of 27 simulations for the faulty conditions and an additional 3 simulations for the healthy machine. The faulty simulations are categorized into three types: static eccentricity, dynamic eccentricity, and mixed eccentricity, with each fault type consisting of 9 simulations. For every fault type, three severity levels—20%, 30%, and 40%—are examined. Furthermore, each fault type and severity level is tested under three distinct load conditions corresponding to load resistances of 17.5 Ω, 13.125 Ω, and 21.875 Ω. The total simulation setup is summarized in the following table:

Table 5.1. Fault Simulation Overview

Fault Type	Severity Level	Load Cases (Ω)	Simulations per Type
Static Eccentricity Fault	20%, 30%, 40%	17.5, 13.125, 21.875	9
Dynamic Eccentricity Fault	20%, 30%, 40%	17.5, 13.125, 21.875	9
Mixed Eccentricity Fault	20%, 30%, 40%	17.5, 13.125, 21.875	9
Healthy Machine	None	17.5, 13.125, 21.875	3

5.2 Performance Analysis

This section presents a detailed analysis of the machine's performance under various simulated conditions, presented in the case study. The results were derived through signal processing and analysis performed in MATLAB. The outcomes are presented below.

Table 5.2. Performance Characteristics for Load = 17.5 Ω

Condition	Vrms (V)	Irms (A)	Torque (Nm)	P_{el} (kW)	P_{mech} (kW)	Efficiency (%)
Healthy	300.74	17.185	1567.0	15.505	16.409	94.489
Static 20%	300.75	17.186	1568.3	15.506	16.423	94.414
Static 30%	300.75	17.186	1569.8	15.506	16.439	94.321
Static 40%	300.75	17.186	1572.0	15.506	16.462	94.190
Dynamic 20%	300.75	17.186	1567.8	15.506	16.418	94.444
Dynamic 30%	300.75	17.186	1568.7	15.506	16.428	94.388
Dynamic 40%	300.75	17.186	1570.1	15.506	16.442	94.308
Mixed 20%	300.75	17.186	1567.5	15.505	16.415	94.459
Mixed 30%	300.75	17.186	1568.1	15.505	16.421	94.425
Mixed 40%	300.75	17.186	1569.0	15.506	16.431	94.369

Table 5.3. Performance Characteristics for Load = 13.125 Ω

Condition	Vrms (V)	Irms (A)	Torque (Nm)	P_{el} (kW)	P_{mech} (kW)	Efficiency (%)
Healthy	295.03	22.479	2047.6	19.896	21.443	92.787
Static 20%	295.04	22.479	2049.0	19.897	21.457	92.730
Static 30%	295.04	22.479	2050.5	19.897	21.473	92.661
Static 40%	295.04	22.479	2052.7	19.897	21.496	92.561
Dynamic 20%	295.04	22.479	2048.5	19.897	21.452	92.752
Dynamic 30%	295.04	22.479	2049.4	19.897	21.462	92.711
Dynamic 40%	295.04	22.480	2050.8	19.897	21.476	92.651
Mixed 20%	295.04	22.479	2048.2	19.897	21.449	92.764
Mixed 30%	295.04	22.479	2048.8	19.897	21.454	92.738
Mixed 40%	295.04	22.479	2049.7	19.897	21.465	92.697

Table 5.4. Performance Characteristics for Load = 21.875 Ω

Condition	Vrms (V)	Irms (A)	Torque (Nm)	P_{el} (kW)	P_{mech} (kW)	Efficiency (%)
Healthy	304.23	13.908	1268.7	12.693	13.286	95.541
Static 20%	304.24	13.908	1270.0	12.694	13.299	95.447
Static 30%	304.24	13.908	1271.5	12.694	13.316	95.331
Static 40%	304.23	13.908	1273.7	12.694	13.338	95.167
Dynamic 20%	304.24	13.908	1269.5	12.694	13.294	95.484
Dynamic 30%	304.24	13.908	1270.5	12.694	13.304	95.415
Dynamic 40%	304.24	13.908	1271.8	12.694	13.318	95.315
Mixed 20%	304.23	13.908	1269.2	12.694	13.291	95.503
Mixed 30%	304.23	13.908	1269.8	12.694	13.297	95.461
Mixed 40%	304.24	13.908	1270.8	12.694	13.307	95.392

From the above tables, it can be observed that the values of V_{rms} and I_{rms} remain almost unaffected by the faulty conditions as was explained on Chapter 3 (Section 3.1.3). On the other hand, the torque shows a slight increase with the severity of the fault. This increase in torque, in turn, leads to a corresponding rise in the mechanical power (P_{mech}) of the machine. Since the electrical power (P_{el}) remains unaffected by the faults, the increase in mechanical power results in a slight decrease in efficiency for all faulty conditions. This drop in efficiency becomes more pronounced as the severity of the fault increases. However, even in the worst-case scenario, the decrease in efficiency is very small and cannot be used as a reliable indicator to identify the fault.

Additionally, it can be observed that the machine's efficiency varies depending on the load conditions. Specifically, efficiency increases with the increase in load and decreases with the decrease in load. This occurs because higher load resistances reduce the circulating currents between the parallel coils of each phase. As will be explained later, circulating currents cause higher temperatures and increased losses within the machine, which may result in additional faults.

5.3 Motor Current Signature Analysis

The first step in diagnosing faulty conditions involves applying the Motor Current Signature Analysis (MCSA) diagnostic method. This technique utilizes the Fourier Transform on the phase current signal to analyze its harmonic content, allowing for the identification of characteristic frequencies associated with specific faults.

5.3.1 Static Eccentricity with MCSA

The results of the MCSA analysis for different severity levels of the static eccentricity fault at the nominal load of 17.5 Ω are presented in Figure 5.1.

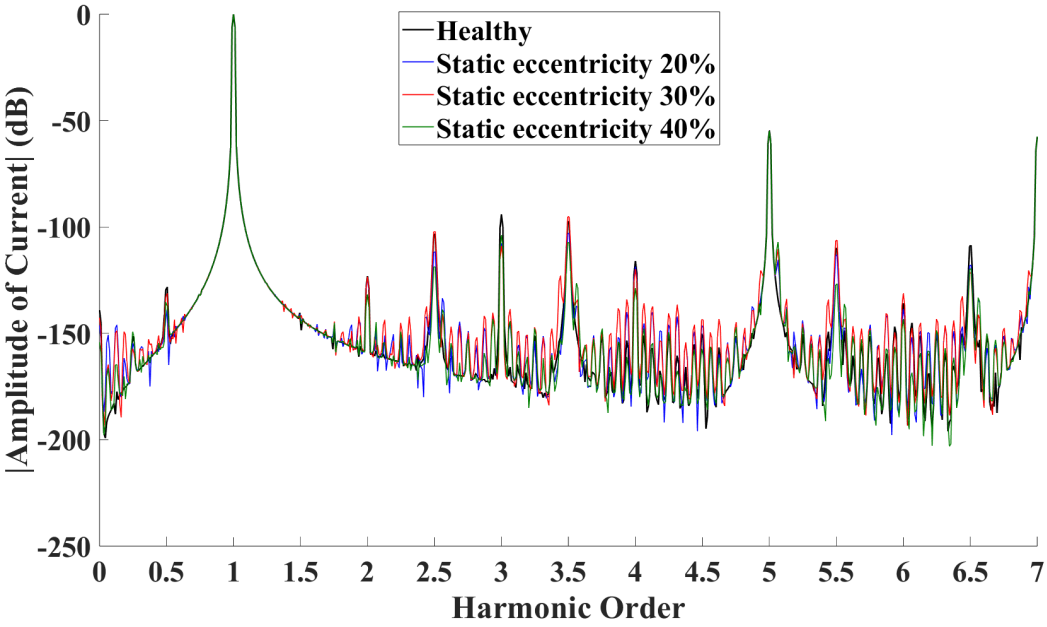

Figure 5.1. MCSA under static eccentricity Fault with nominal Load

The results are disappointing, as the method fails to produce characteristic fault signatures, as shown in Figure 5.1. This failure can be attributed to the double rotor design, which mirrors the asymmetry of the fault between the two sides of the machine, and the absence of an iron core that prevents the induction of spatial magnetic asymmetry, which could otherwise amplify fault signatures. This phenomenon is discussed in detail in Chapter 3 (Section 3.1.3).Another significant reason for the failure of the MCSA method is the circuit design, which inherently cancels some of the important characteristic frequencies that are indicative of the static fault. Due to static eccentricity, each coil in the parallel arrangement of the circuit design, experiences a different flux depending on its location. These flux variations do not change with time because the eccentricity is static. Because the flux-variations are not time-dependent we expect a periodic behavior of the flux and the coil current with frequency f_s. With the introduction of a static eccentricity fault, the machine exhibits a significant increase in the third harmonic of the coil current as the fault severity increases. Under healthy conditions, the third harmonic is absent due to the Y-connection of the circuit. In a Y connection, the phase current is identical to the line current, and the third harmonics cancel out as a result of the circuit's configuration.

As will be shown later (Figure 5.7), the C-GEN machine has an air-gap magnetic flux density that is nearly identical under healthy and static eccentricity conditions. However, small asymmetries are present in faulty conditions, leading to a magnetic flux density (B) that is less sinusoidal. These asymmetries in B introduce slight distortions in the flux of the coil under

faulty conditions, which are translated into the coil current. This results in a stronger 3rd harmonic.

As mentioned in Chapter 3 (Section 3.2.1), static eccentricity is expected to produce characteristic frequencies at $f_{\text{fault}} = \left(1 \pm \frac{k}{p}\right) f_s$. However, because the air-gap asymmetry ($g_{\text{SE}} \approx g_{\text{healthy}}$) is minor in the C-GEN machine, such harmonics are not observed. The presence of these sidebands is linked to the spatial asymmetry of the air-gap flux caused by static eccentricity. Although static eccentricity is a spatial phenomenon and does not vary with time, the rotor's motion interacts with the spatial asymmetry, resulting in periodic flux variations in each coil.

These observations are shown in Figure 5.2, where the spectrum of one of the parallel coils is plotted.

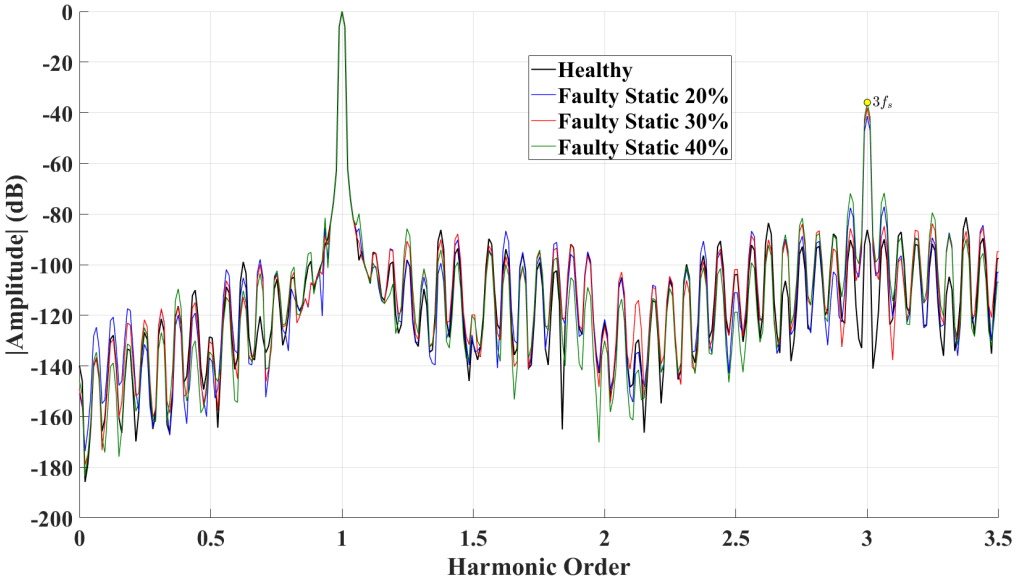

Figure 5.2. Fourier Transform of a coil current under different levels of static eccentricity

Table 5.5. Comparison of $3f_s$ amplitudes under healthy and static eccentricity conditions.

Condition	$3f_s$ **Amplitude (dB)**
Healthy	-86.8454
Static Eccentricity 20%	-41.2971
Static Eccentricity 30%	-38.11
Static Eccentricity 40%	-35.9416

To obtain the phase current we add the currents of the 4 parallel coils in the circuit. All parallel coils exhibit the increase in the third harmonic under static eccentricity. However, when these coil current signals are combined to form the phase current, the third harmonic is significantly attenuated or canceled. This occurs because the signals from each coil, while containing $3f_s$, have specific amplitudes and phases that result in cancellation when summed.

This explains the observations in Figure 5.1 and clarifies why the MCSA method fails to produce characteristic fault frequencies.

5.3.2 Dynamic Eccentricity with MCSA

The results of the MCSA analysis for different severity levels of the dynamic eccentricity fault at the nominal load of 17.5 Ω are presented in Figure 5.3.

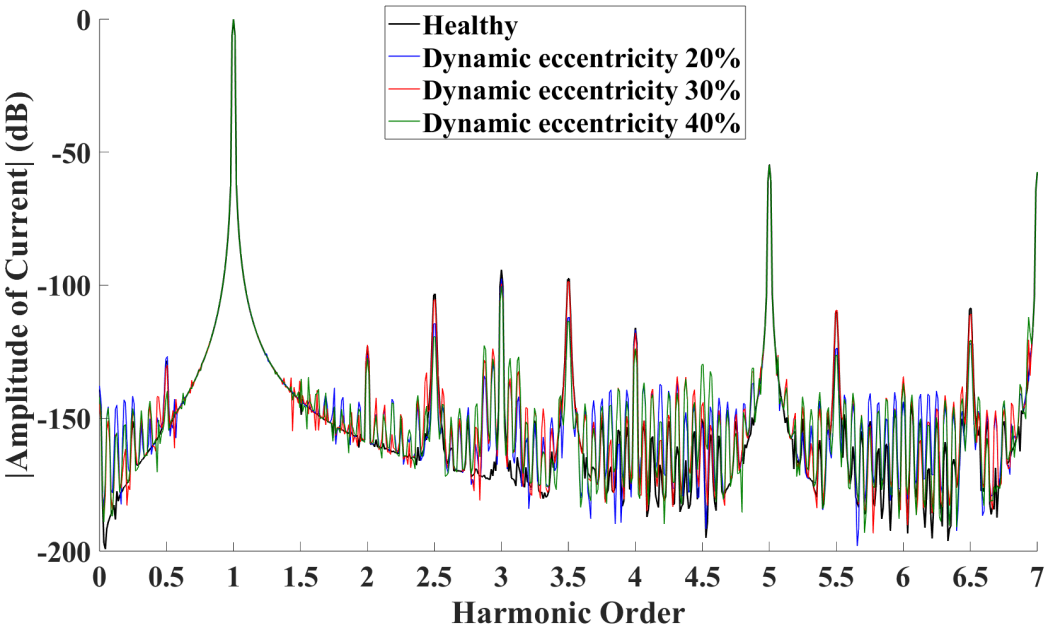

Figure 5.3. MCSA under dynamic eccentricity Fault with nominal Load

MCSA fails to produce characteristic fault signatures, even in the case of dynamic eccentricity. This is attributed to the circuit design of the C-GEN, which plays a significant role in suppressing the dynamic fault signatures, resulting in phase currents that remain nearly unchanged despite the presence of the dynamic fault. This phenomenon is illustrated in Figure 5.3.

With the introduction of dynamic eccentricity, each coil in the parallel arrangement experiences a time-varying current. These variations, caused by the fault moving with the rotors, repeat after one full mechanical cycle of the machine. As the rotor completes one full rotation, the fault returns to the same relative position with respect to the coils, causing the current variation to repeat periodically. After a 180° rotor rotation, a coil that was closer to one rotor (e.g., the inner rotor) due to dynamic eccentricity, will now be closer to the other rotor (e.g., the outer rotor). Consequently, the coil will be closer to the north pole magnet and further from the south pole, opposite to its initial position. Because the rotor has rotated 180°, the flux of the coil will be opposite. However, the current experienced by the coil will not be perfectly opposite, as the inductance of the coil depends on the width of the magnets. Since the two magnets have different widths, this asymmetry introduces additional harmonics. These harmonics correspond to the periodic flux variations caused by the 180° rotation, which occur at twice the mechanical frequency.

This indicates that performing Fourier analysis on one of the parallel coils under dynamic eccentricity reveals harmonics at frequencies $f_s \pm \frac{kf_s}{p}$, where k is an integer and $\frac{f_s}{p}$ corresponds to the mechanical frequency of the rotor. This observation is shown in Figure 5.4 and Table 5.6.

From Table 5.6, we observe that under healthy conditions, the machine's full symmetry ensures the absence of harmonics at $f_s \pm \frac{kf_s}{p}$, as all coils have identical flux and carry the same current. However, when dynamic eccentricity occurs, harmonics appear at these frequencies as expected.

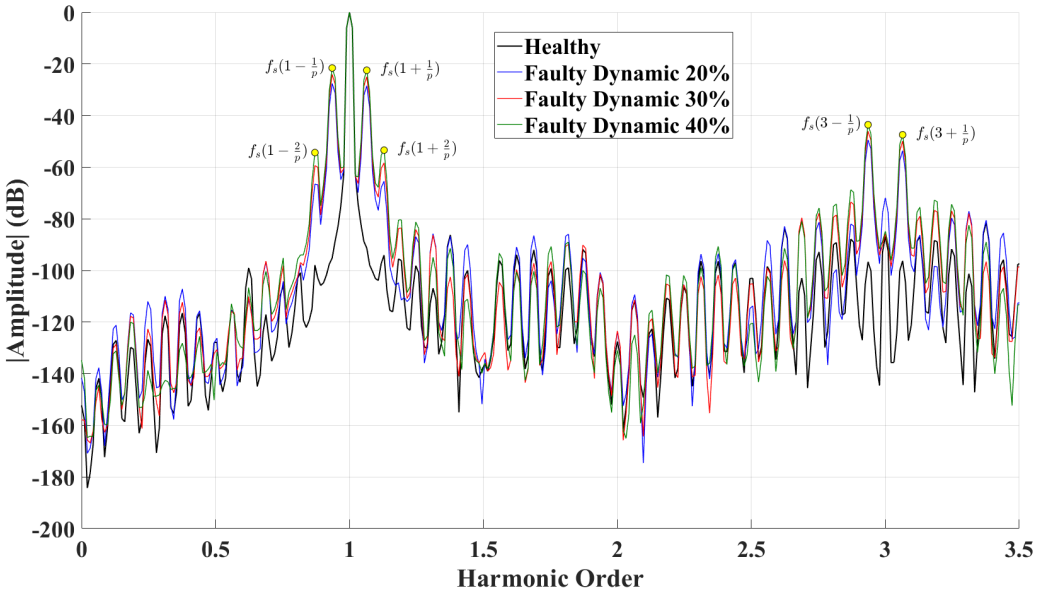

Figure 5.4. Fourier Transform of a coil current under different levels of dynamic eccentricity

Table 5.6. Harmonic Magnitudes (dB) under Healthy and Dynamic Fault Conditions

Condition	$f_s(1-\frac{2}{p})$	$f_s(1-\frac{1}{p})$	$f_s(1+\frac{1}{p})$	$f_s(1+\frac{2}{p})$	$f_s(3-\frac{1}{p})$	$f_s(3+\frac{1}{p})$	$f_s(3-\frac{2}{p})$	$f_s(3+\frac{2}{p})$
Healthy (dB)	-97.9368	-95.1817	-91.2896	-94.0672	-96.6585	-96.2697	-87.8388	-87.0413
Dynamic 20% (dB)	-66.5294	-27.5761	-28.4554	-65.4188	-49.4487	-53.6141	-82.0276	-86.3086
Dynamic 30% (dB)	-59.3765	-24.0604	-24.9322	-58.3313	-46.0716	-49.9138	-73.4715	-79.0217
Dynamic 40% (dB)	-54.3292	-21.5618	-22.4336	-53.3785	-43.5561	-47.4295	-68.7363	-75.4801

Unlike static eccentricity, dynamic eccentricity introduces time-varying current imbalances in the coils due to the rotor's motion. These current variations that are product of flux variations, repeat periodically with each mechanical rotation. Because dynamic eccentricity is a time-varying fault, the amplitude of the signature harmonics are much larger than in the case of static eccentricity, where the flux variations are time-invariant. We also observe sidebands at $\pm\frac{k}{p}$ around $3f_s$, which have smaller amplitudes compared to the sidebands around the fundamental frequency f_s. This is because, as the frequency increases the inductive reactance of the coil increases ($X_L = 2\pi f L$) and the current higher harmonics are attenuated. Lastly, the frequency signatures introduced by the 180° rotation ($k = 2$) have smaller amplitudes because the current of the coil after 180° rotation, will not be opposite only by a small factor.

All parallel coils exhibit the same harmonic frequencies as those listed in Table 5.6 under dynamic eccentricity. However, when these coil current signals are combined to form the phase current, the harmonics at these frequencies are significantly attenuated or canceled. This occurs because the signals from each coil, while containing the same harmonic frequencies, have specific amplitudes and phases that result in cancellation when summed.

This explains the observations in Figure 5.3 and highlights why the MCSA method fails to produce characteristic fault frequencies under dynamic eccentricity.

5.3.3 Mixed Eccentricity with MCSA

The results of the MCSA analysis for different severity levels of the mixed eccentricity fault at the nominal load of 17.5 Ω are presented in (Figure 5.5).

Mixed eccentricity is a combination of static and dynamic eccentricity faults. Similar to the individual static and dynamic cases, the MCSA method fails to detect characteristic fault signatures for mixed eccentricity due to the same underlying reasons.

As with dynamic eccentricity, the flux variations introduced by the mixed fault in a single coil repeat every full rotation of the machine. Additionally, due to the different magnet widths, harmonics linked to half rotation of the machine will be introduced, as was the case with dynamic eccentricity.

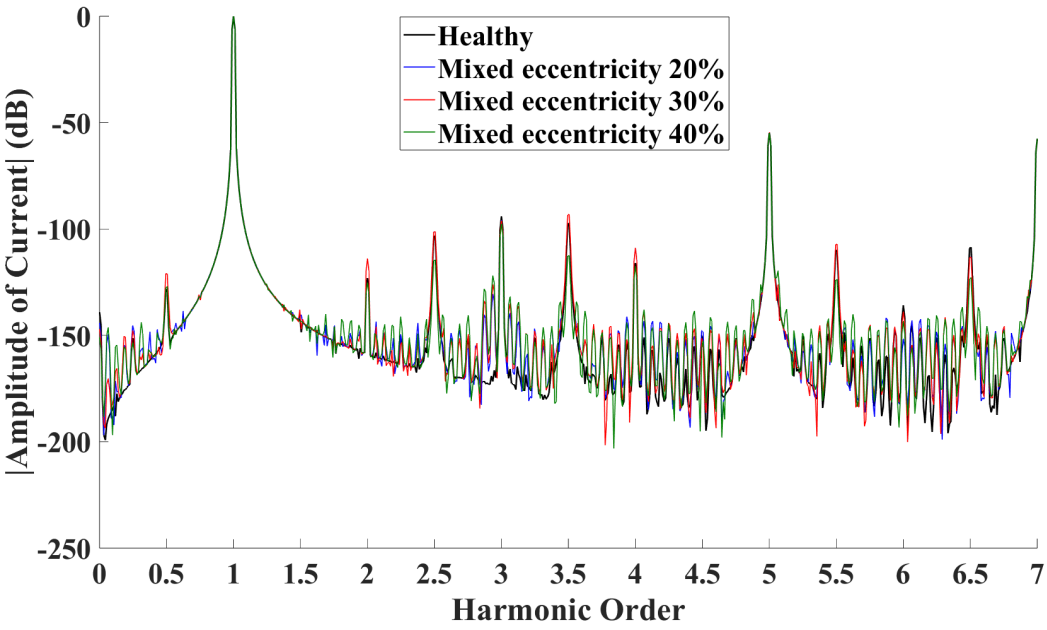

Figure 5.5. MCSA under mixed eccentricity Fault with nominal Load

Performing Fourier analysis on one of the parallel coils under mixed eccentricity reveals harmonics at frequencies $f_s \pm \frac{kf_s}{p}$, where k is an integer and $\frac{f_s}{p}$ corresponds to the mechanical frequency of the rotor. Also harmonics at $3f_s$ from the static component of the fault are expected. This observation is shown in Figure 5.6 and Table 5.7.

Table 5.7. Harmonic Magnitudes (dB) under Healthy and Mixed Fault Conditions

Condition	$f_s(1-\frac{2}{p})$	$f_s(1-\frac{1}{p})$	$f_s(1+\frac{1}{p})$	$f_s(1+\frac{2}{p})$	$f_s(3-\frac{1}{p})$	$f_s(3+\frac{1}{p})$	$f_s(3-\frac{2}{p})$	$f_s(3+\frac{2}{p})$	$3f_s$
Healthy (dB)	-97.9368	-95.1817	-91.2896	-94.0672	-96.6585	-96.2697	-87.8388	-87.0413	-86.8454
Mixed 20% (dB)	-71.4002	-29.9737	-30.9509	-70.367	-51.9103	-55.9599	-82.8617	-88.0644	-60.425
Mixed 30% (dB)	-66.277	-27.3739	-28.4534	-65.2052	-49.1993	-53.5907	-77.7539	-82.3301	-54.9604
Mixed 40% (dB)	-59.199	-23.8508	-24.9341	-58.1525	-45.5525	-50.2631	-71.8922	-75.4966	-54.9578

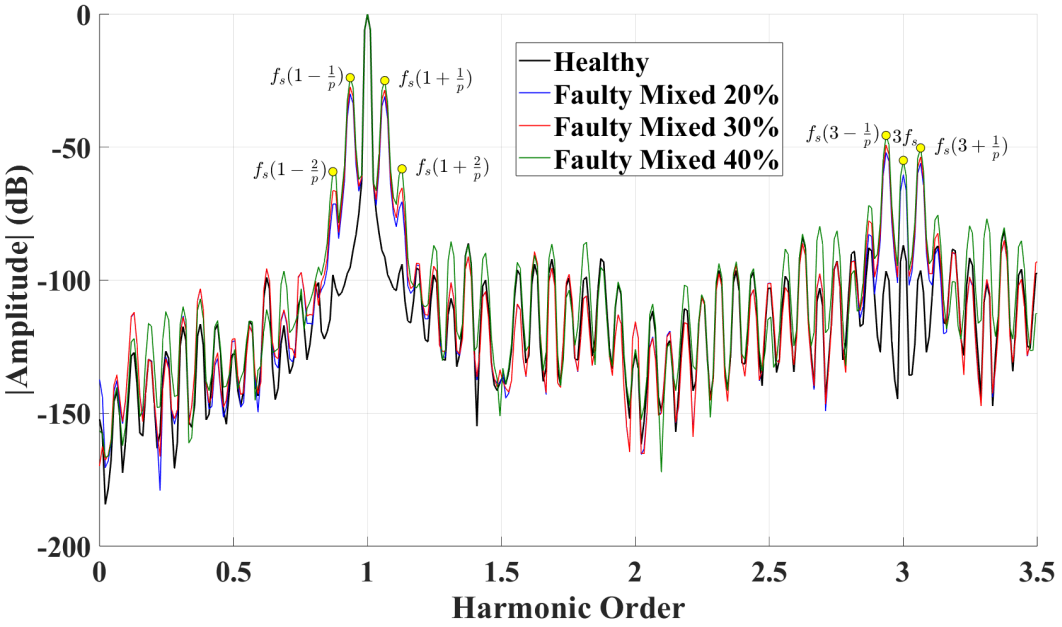

Figure 5.6. Fourier Transform of a coil current under different levels of mixed eccentricity

From Table 5.7, when mixed eccentricity occurs, harmonics appear at frequencies $f_s \pm \frac{kf_s}{p}$ as expected. Mixed eccentricity introduces time-varying current imbalances in the coils due to the dynamic fault component and spatial imbalances from the static fault component. These current variations that are product of flux variations, repeat periodically with each mechanical rotation. We also observe sidebands at $\pm\frac{k}{p}$ around $3f_s$, which have smaller amplitudes compared to the sidebands around the fundamental frequency f_s. This is because, as the frequency increases the inductive reactance of the coil increases ($X_L = 2\pi fL$) and the amplitude of the current harmonics is attenuated. The frequency signatures introduced by the 180° rotation ($k = 2$) have smaller amplitudes because the current of the coil after 180° rotation, will not be opposite only by a small factor. Lastly, we observe an increase in the amplitude of the 3rd harmonic in the coil current spectrum. This increase is attributed to the static component of the mixed fault, as previously explained in the Motor Current Signature Analysis (MCSA) under static eccentricity. An interesting observation is that for both 30% and 40% mixed eccentricity, the amplitude of the 3rd harmonic remains the same. This behavior can be explained by the fact that the static eccentricity component used in both 30% and 40% mixed eccentricity cases is identical, resulting in no further change in the amplitude of the 3rd harmonic.

All parallel coils exhibit the same harmonic frequencies as those listed in Table 5.7 under mixed eccentricity. However, when these coil current signals are combined to form the phase current, the harmonics at these frequencies are significantly attenuated or canceled. This occurs because the signals from each coil, while containing the same harmonic frequencies, have specific amplitudes and phases that result in cancellation when summed.

This explains the observations in Figure 5.5 and highlights why the MCSA method fails to produce characteristic fault frequencies under mixed eccentricity.

5.4 Circulating Currents and Their Impact on Machine Performance

As discussed in Chapter 3 (Section 3.1.3) and demonstrated in the previous Section 5.3, MCSA fails to produce characteristic fault signatures. This limitation arises from the fact that the magnetic air-gap flux density across the machine remains nearly unchanged with the introduction of the three faults, combined with the fact that, when the parallel coil currents are summed to obtain the phase current, harmonic cancellation appears. This observation holds true for all types of eccentricity faults. The magnetic flux densities for the three fault types are presented below :

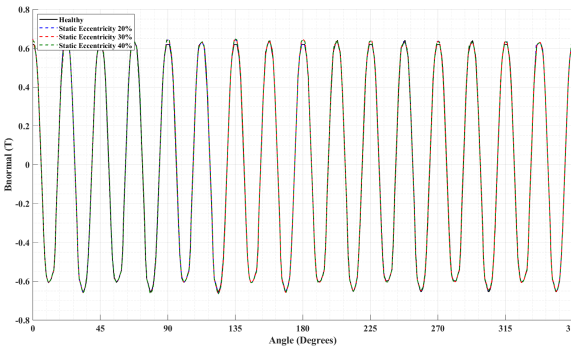

(a) Air-gap Magnetic Field Density under Static Eccentricity Fault

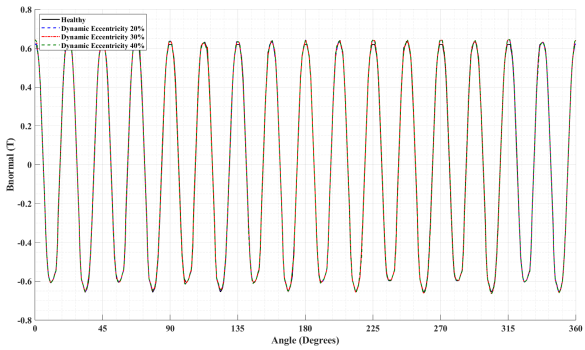

(b) Air-gap Magnetic Field Density under Dynamic Eccentricity Fault

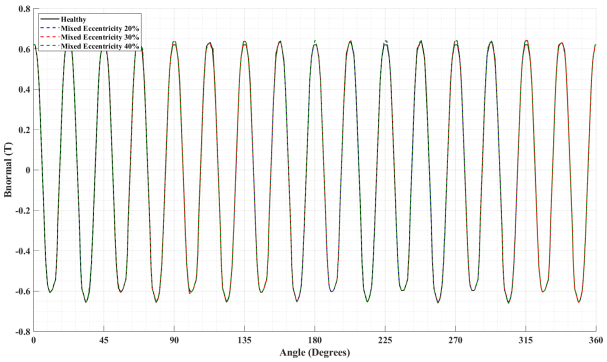

(c) Air-gap Magnetic Field Density under Mixed Eccentricity Fault

Figure 5.7. Air-gap Magnetic Field Density under Different Eccentricity Faults

From the results, it can be observed that the mean value of the differences between the healthy and faulty cases remains almost unchanged across all fault types and severity levels. This means that the air-gap magnetic field density across the machine remains practically unchanged under the different eccentricity faults. The computed mean values are summarized in Table 5.8.

Table 5.8. Mean Value of Differences Between Healthy and Faulty Cases

Fault Type	20% Severity (T)	30% Severity (T)	40% Severity (T)
Static Eccentricity	0.0011	0.0011	0.0011
Dynamic Eccentricity	0.0010	0.0014	0.0014
Mixed Eccentricity	0.0010	0.0010	0.0011

The inability to detect the eccentricity fault using conventional diagnostic methods is dangerous. The eccentricity fault causes the development of circulating currents within the stator parallel coils, resulting in uneven stress distribution. Some of the coils are seriously over-stressed while others are under-stressed. The over-stressed coils are particularly problematic , since higher current flow causes increased losses and higher operational temperatures. This leads to faster degradation of the insulation and the higher probability of an early stator inter-turn or phase to phase fault. Additionally, the high temperature contributes to faster demagnetization of the permanent magnets, further compromising the machine's performance and reliability. The uneven stress distribution can be seen from (Figure 5.8) which demonstrates the current density in the middle of the stator coils along the stator circumference.

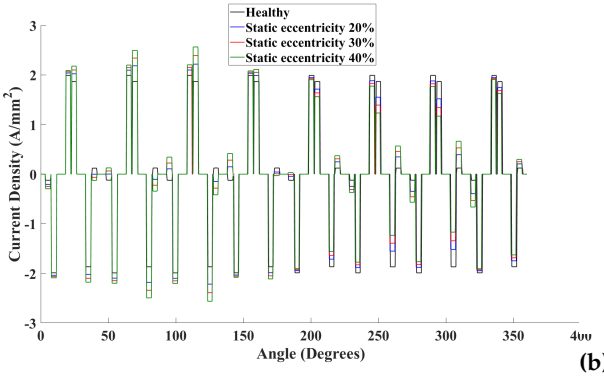

(a) Current Density in the middle of the stator coils along the circumference under Static Eccentricity Fault

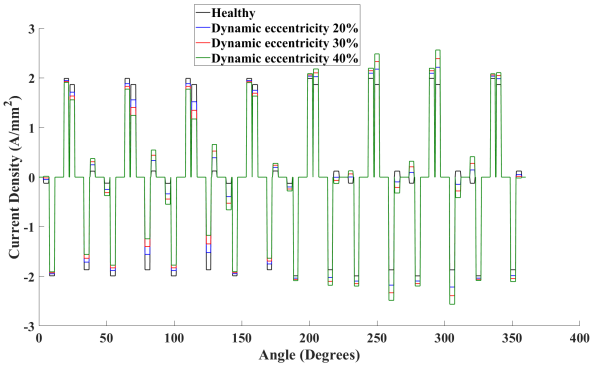

(b) Current Density in the middle of the stator coils along the circumference under Dynamic Eccentricity Fault

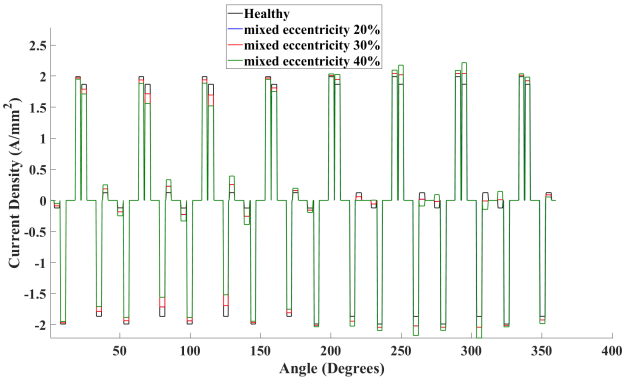

(c) Current Density in the middle of the stator coils along the circumference under Mixed Eccentricity Fault

Figure 5.8. Current Density in the middle of the stator coils along the circumference under Different Eccentricity Faults

Table 5.9. Current Increase in the Worst Coil Case under Maximum Severity Level

Eccentricity Type	Current Density Rise (%)
Static Eccentricity	37.27
Dynamic Eccentricity	37.13
Mixed Eccentricity	18.56

As observed in Table 5.9, the current rise in the worst-case scenario is substantial. This finding is critical because, although the machine's line current does not exhibit any noticeable differences, the machine is under significant stress.

It is important to note that the current density distribution on the stator coils differs significantly between static and dynamic eccentricity. Under static eccentricity, the stator displacement relative to the rotor is fixed. Consequently, the coils experiencing the highest stress, remain the same over time, as the fault does not rotate with the rotor. In contrast, under dynamic eccentricity, the rotor's displacement varies with time as it rotates. This leads to time-dependent variations in the stress levels experienced by different coils. In mixed eccentricity, the stress becomes distributed more evenly across all coils, leading to a smaller current density change because no single coil is excessively overstressed.

5.4.1 Circulating Currents of the Four Parallel Coils Under Static Eccentricity

The uneven distribution of the current affects the stator coils that are connected in parallel, forcing them to carry circulating currents since the produced electromotive forces are uneven in different locations under fault. In the machine the four parallel connected coils carry the exact same current, however the distribution changes when there is a fault, while the current difference increases with the increase of the fault severity.

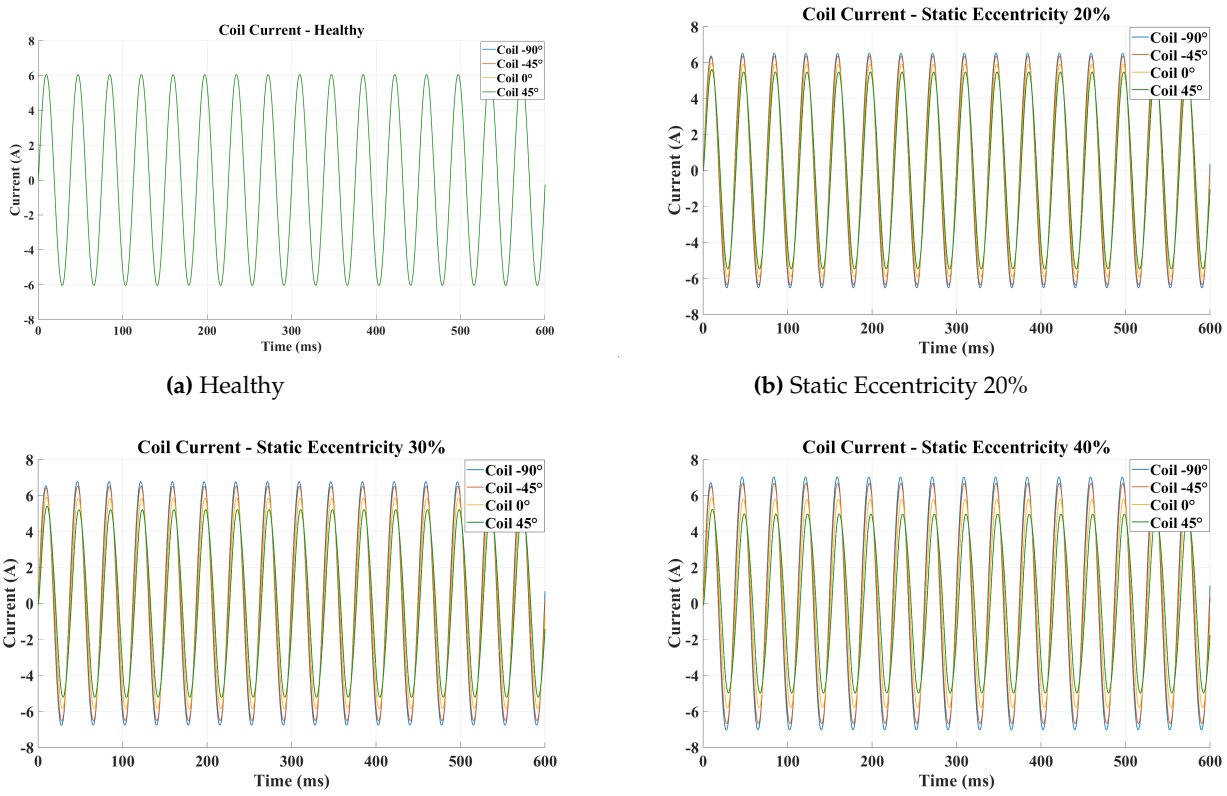

(a) Healthy

(b) Static Eccentricity 20%

(c) Static Eccentricity 30%

(d) Static Eccentricity 40%

Figure 5.9. Current of the four parallel coils under static eccentricity

Figure 5.9 illustrates the current behavior of the four parallel coils in a single phase under different levels of static eccentricity. The parallel coils are positioned at -90° (blue), -45° (orange), 0° (yellow), and 45° (green). As was expected under healthy conditions, the parallel coils carry the exact same current, but the distribution changes with the introduction of the static eccentricity fault. Because it is a static fault, the distribution of the current of each coil will not change over time.

Table 5.10. Parallel Stator Coil Currents (RMS)

Coil Location	Healthy (A)	20% SE (A)	30% SE (A)	40% SE (A)
-90°	4.28	4.6	4.78	4.96
-45°	4.28	4.49	4.6	4.72
0°	4.28	4.18	4.14	4.12
45°	4.28	3.88	3.7	3.47

Two of the coils are observed to carry a current higher than their rated value, while the other two are undercharged. Specifically, the worst case (i.e., the coil experiencing the greatest current increase) exhibits a current rise of 7.47%, 11.68%, and 15.88% for the three static fault scenarios, respectively.

The increase in current directly impacts the local Joule losses, which are given by:

$$P_{\text{Joule}} = I^2 R \tag{5.1}$$

where I is the current through the coil, and R is its resistance.

Due to the quadratic relationship between current and losses, these current increases result in local Joule losses rising by 15.5%, 24.72%, and 34.28% for the respective fault cases. This significant increase in losses highlights the critical impact of these faults on the machine's performance. However, despite the increase in local Joule losses, the total line current, which is the sum of the currents from the four parallel coils, remains unaffected by the fault.

5.4.2 Circulating Currents of the Four Parallel Coils Under Dynamic Eccentricity

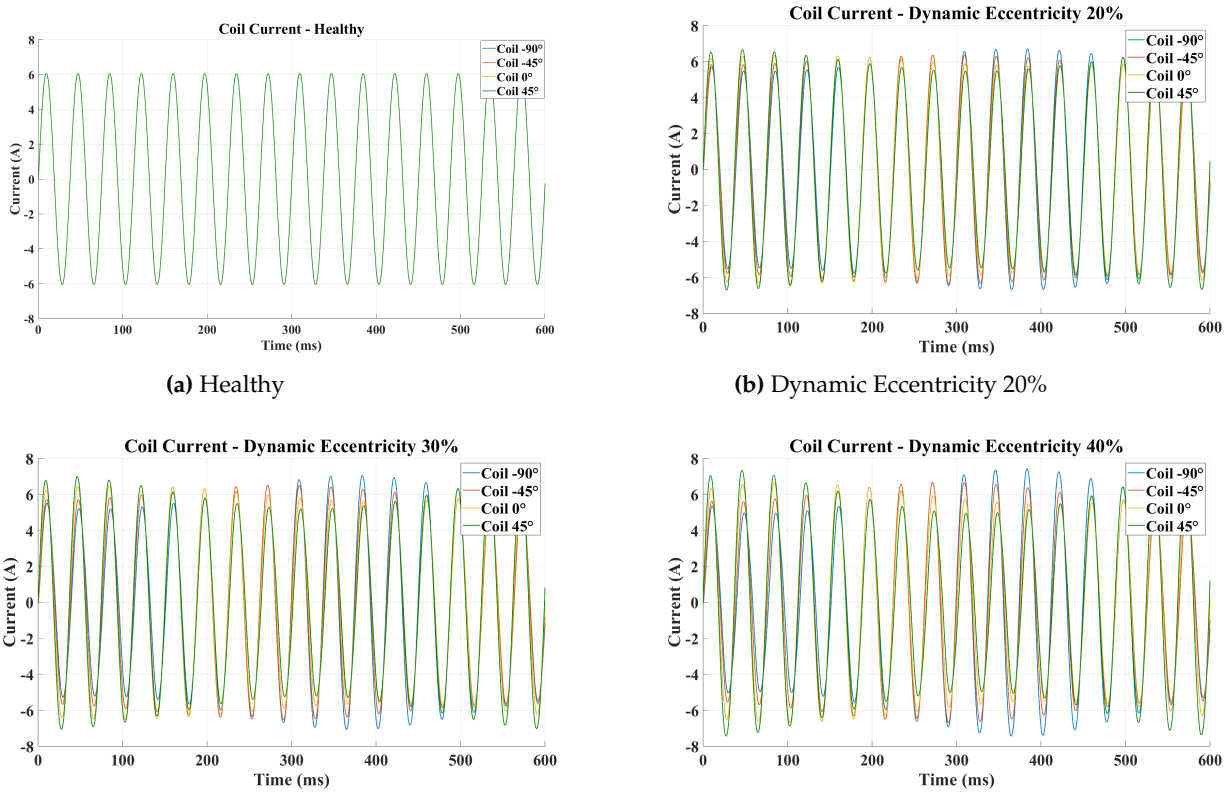

(a) Healthy

(b) Dynamic Eccentricity 20%

(c) Dynamic Eccentricity 30%

(d) Dynamic Eccentricity 40%

Figure 5.10. Current of the four parallel coils under Dynamic eccentricity

Similar to the static eccentricity fault, the current distribution among the four parallel-connected coils also changes in the presence of a dynamic eccentricity fault. Also, the difference in coil currents becomes more pronounced as the severity of the fault increases.

Figure 5.10 illustrates the current behavior of the four parallel coils in a single phase under different levels of dynamic eccentricity. The parallel coils are positioned at -90° (blue), -45° (orange), 0° (yellow), and 45° (green). As was expected under healthy conditions, the parallel coils carry the exact same current, but the distribution changes with the introduction of the dynamic eccentricity fault.

Because it is a dynamic fault, the distribution of the current of each coil will change over time. This means that the coil currents are no longer constant, and the stress alternates between coils as the fault progresses dynamically. The dynamic nature of the fault leads to time-varying Joule losses in the individual coils, that increase as the fault progresses.

5.4.3 Circulating Currents of the Four Parallel Coils Under Mixed Eccentricity

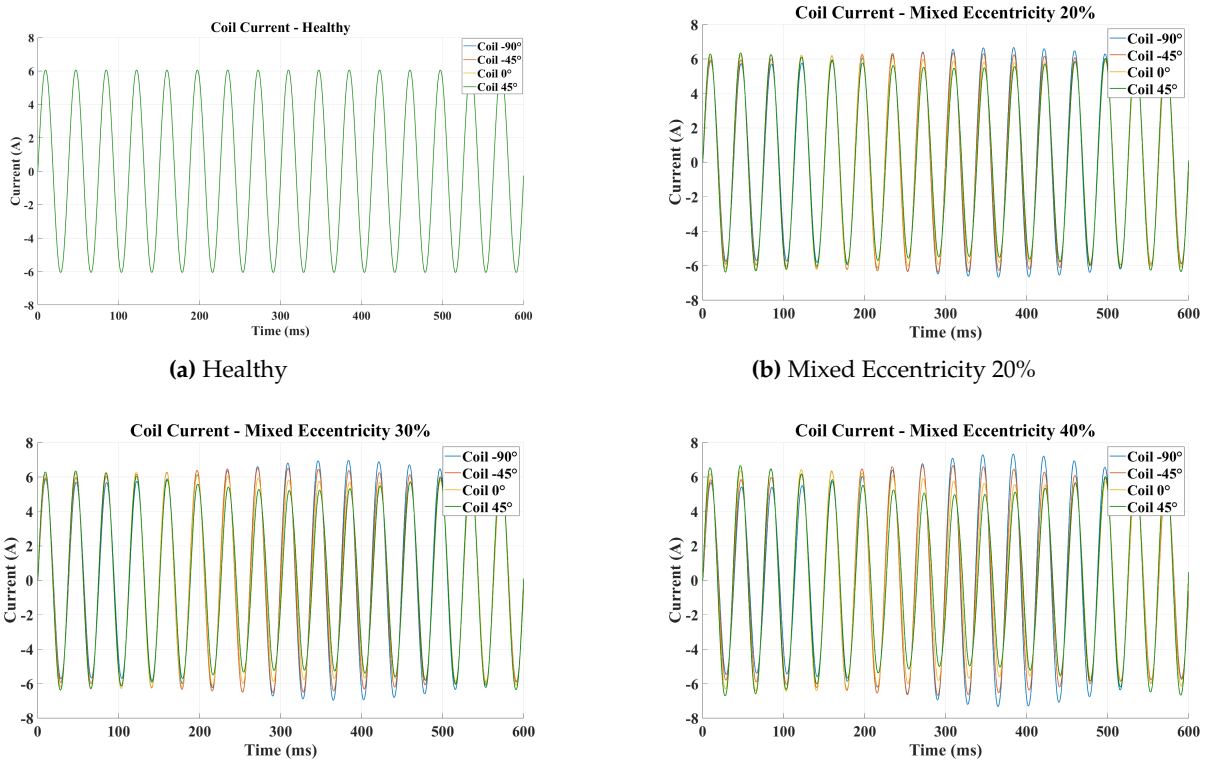

(a) Healthy

(b) Mixed Eccentricity 20%

(c) Mixed Eccentricity 30%

(d) Mixed Eccentricity 40%

Figure 5.11. Current of the four parallel coils under Dynamic eccentricity

Because mixed eccentricity combines the effects of static and dynamic eccentricity, the current distribution among the coils exhibits both time-varying and stationary characteristics. Specifically, the dynamic component of the fault causes the current distribution to change over time, as the rotor's displacement varies dynamically. Meanwhile, the static component causes certain coils to consistently carry higher currents and others to carry less current. In mixed eccentricity, the stress tends to become more evenly distributed across all coils compared to pure static or dynamic eccentricity. This leads to a smaller overall change in current density, as no single coil is excessively overstressed, reducing localized peaks in stress. This means that Joule losses are less extreme in individual coils due to the more even stress distribution. However, mixed eccentricity can still accelerate machine degradation due to cumulative thermal effects and stress cycling.

5.4.4 Circulating Currents Under Different Loads

Under healthy conditions, when the resistive load increases, the current in the coils decreases. This behavior aligns with Ohm's Law. We can verify this by plotting the current in a single coil under healthy conditions for three different loads.

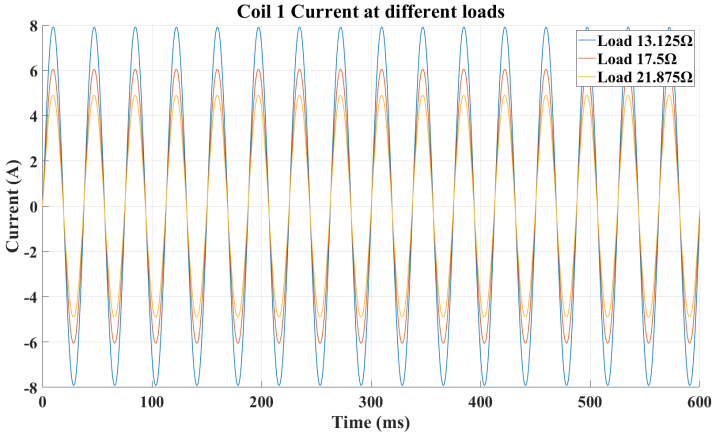

Figure 5.12. Healthy Coil Current Under Different Loads

As the load increases, Joule losses increase, causing a drop in efficiency. Under faulty conditions such as eccentricity, circulating currents arise in the stator coils connected in parallel. According to Ohm's Law, as the load increases, the amplitude of these circulating currents decreases. Conversely, when the load decreases, the circulating currents increase in amplitude, leading to higher Joule losses in overstressed coils. This behavior is illustrated in the figure below, showing the coil current positioned at -90^o under 40% Static, Dynamic, and Mixed Eccentricity for three different loads.

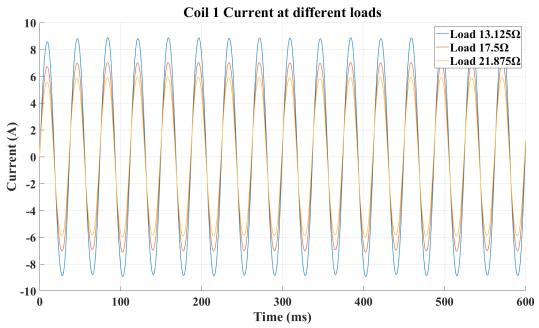

(a) Static Eccentricity

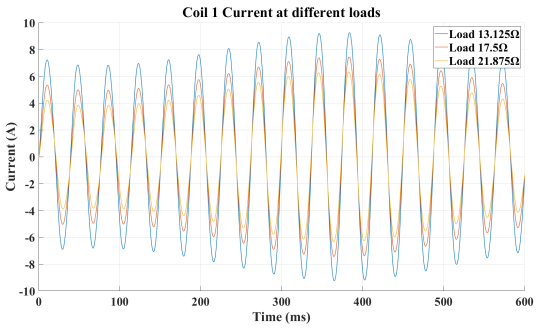

(b) Dynamic Eccentricity

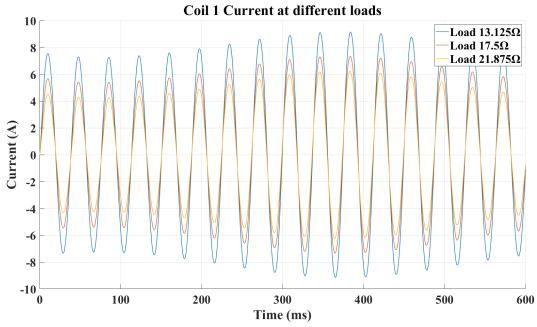

(c) Mixed Eccentricity

Figure 5.13. Coil Current under 40% Static, Dynamic, and Mixed Eccentricities for Different Loads

Interestingly, under different loads, the amplitude of the coil current variations from the healthy, remains the same. This is demonstrated in the figure below.

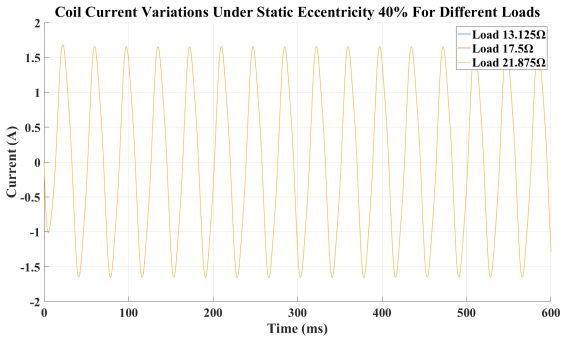

(a) Static Eccentricity

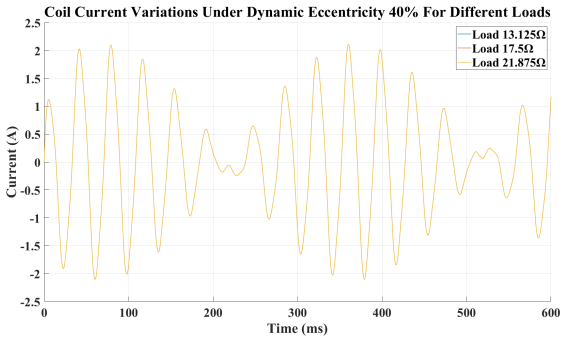

(b) Dynamic Eccentricity

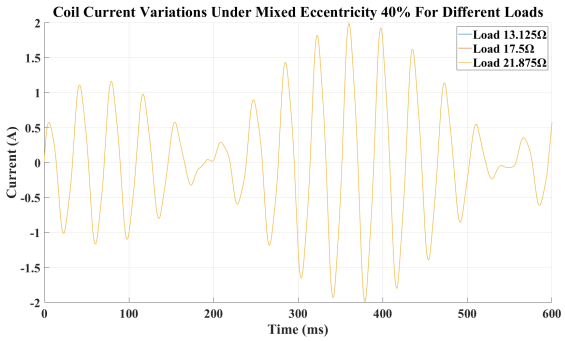

(c) Mixed Eccentricity

Figure 5.14. Coil Current Variations under 40% Static, Dynamic, and Mixed Eccentricities for Different Loads

This suggests that the variations in a coil current relative to healthy conditions depend solely on the type and severity of the eccentricity fault, and are independent of the load. Despite the constancy of these variations, a smaller load results in an increase in the overall coil current. When eccentricity faults are introduced, these variations overstress certain coils, leading to higher Joule losses and elevated temperature levels, which may further contribute to the development of additional faults.

5.5 Torque Monitoring

The next step in our analysis is to examine the torque spectrum under various types of eccentricity faults. This technique, utilizes the Fourier Transform on the Torque signal to analyze its harmonic content, allowing for the identification of characteristic frequencies associated with specific faults.

5.5.1 Static Eccentricity with Torque Monitoring

The Torque signal for different severity levels of the static eccentricity fault at the nominal load of 17.5Ω is presented in Figure 5.15

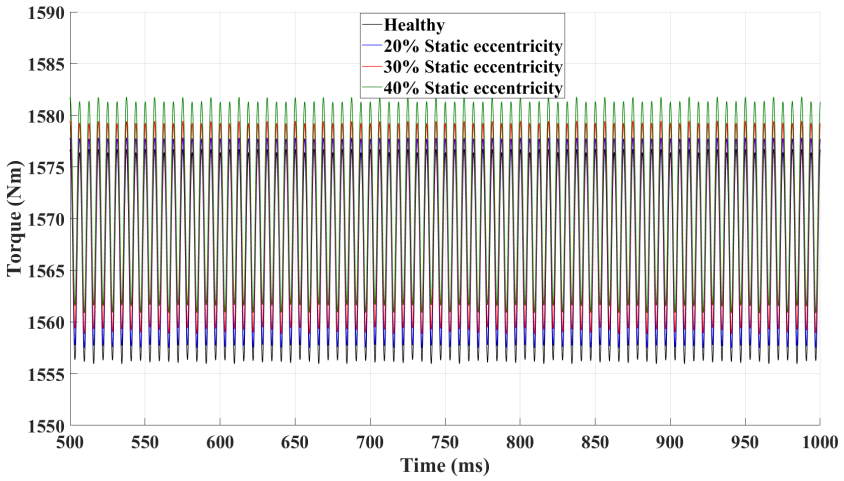

Figure 5.15. Torque Signal Under static eccentricity Fault with nominal Load

The torque signal primarily exhibits a DC component. As observed in Figure 5.15, the mean value of the torque signal increases slightly with increasing fault severity. This slight increase occurs because, while some coils experience higher currents resulting in stronger magnetic forces, other coils experience lower currents due to the specific symmetry of the double rotor topology. The net effect of these localized imbalances is a small overall increase in the mean torque. Despite that, as shown in Table 5.11, the torque ripple remains nearly constant across different fault severity levels.

Table 5.11. Torque Ripple for Different Eccentricity Levels

Eccentricity Level	Ripple (Nm)
Healthy	10.391
20% Static Eccentricity	10.166
30% Static Eccentricity	10.325
40% Static Eccentricity	10.476

The results of the Torque Monitoring diagnostic method on the frequency domain, for different severity levels of the static eccentricity fault at the nominal load of 17.5Ω are presented in Figure 5.16.

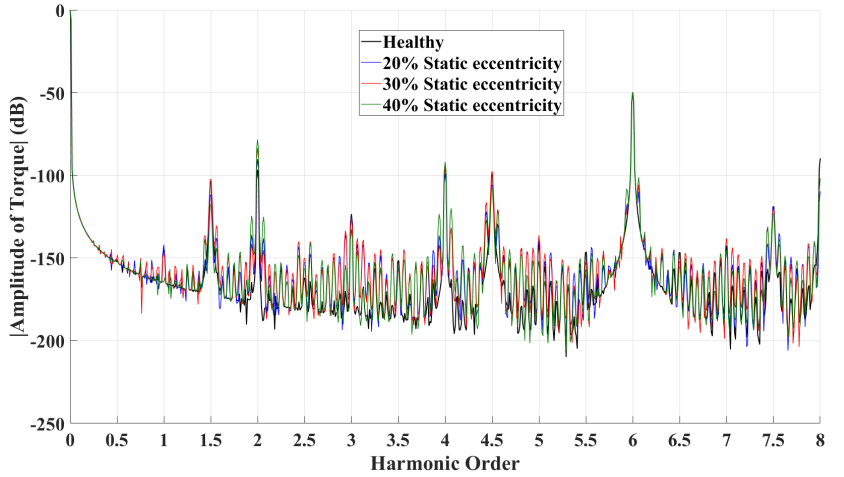

Figure 5.16. Torque Analysis Using FFT, Under static eccentricity Fault

Since the torque is a DC signal, the largest harmonic is expected to appear at 0 Hz. The second-largest harmonic observed is the 6th harmonic. The presence of the 6th harmonic is inherent to the machine's operation and does not result from a fault. Instead, it arises from the interaction between the 5th and 1st harmonics of the stator and rotor.

From the harmonic content of the torque signal, we observe a monotonic increase in the second harmonic as the fault severity increases. This observation aligns with (Equation 3.24) $f_{se} = 2kf_s$ for k = 1, which represents the characteristic fault signature frequencies associated with static eccentricity in permanent magnet synchronous machines. The second harmonic arises from the interaction between the 1st harmonic of the stator and rotor fields. This interaction is inherently stronger due to the fundamental nature of these components.Because the air-gap magnetic flux density along the circumference of the machine remains unchanged with the introduction of the static eccentricity fault, higher-order harmonics are suppressed, as their excitation often requires significant asymmetry in the overall magnetic field. Although a very small asymmetry is present due to local asymmetries of the coils, it is negligible and primarily reflected in the second harmonic. The amplitude of the harmonics introduced by the fault at the 2nd harmonic, remains very small as shown in Figure 5.17.

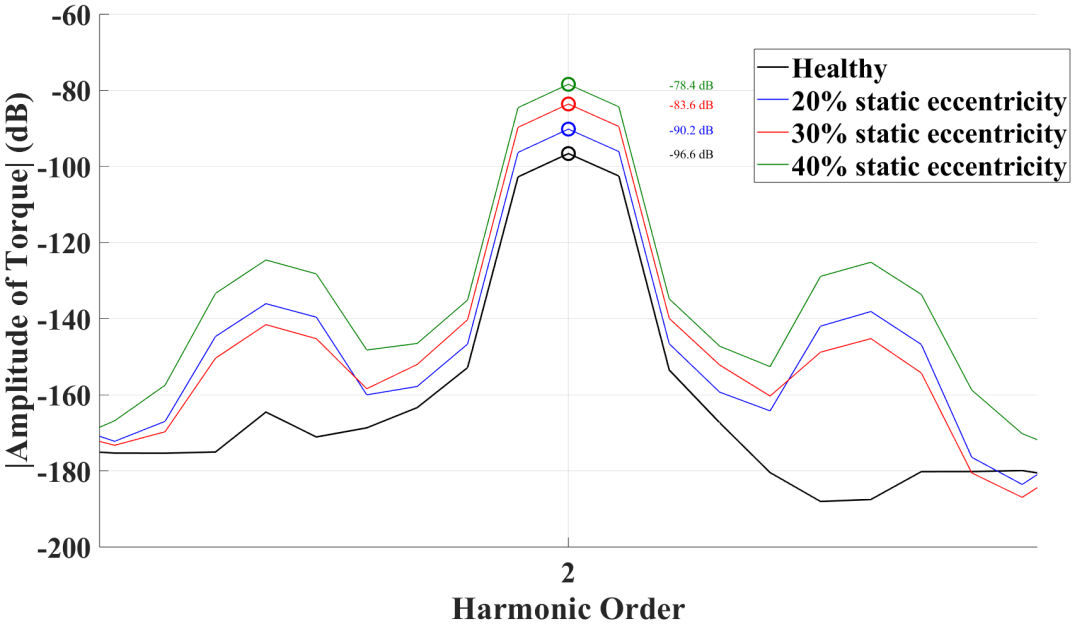

Figure 5.17. Torque Signal 2nd Harmonic

Given the small amplitude, even in the worst-case scenario, it is not sufficient to determine if the machine is under faulty conditions.

5.5.2 Dynamic Eccentricity with Torque Monitoring

The Torque signal for different severity levels of the dynamic eccentricity fault at the nominal load of 17.5Ω is presented in Figure 5.18

As observed, the torque signal exhibits time-varying periodic behavior due to the nature of dynamic eccentricity. The mean value of the torque signal increases slightly with increasing fault severity. This slight increase arises because the time-varying displacement of the rotor causes time-varying localized increases in the magnetic forces in the coils. The specific symmetry of the double rotor topology ensures that these imbalances result in only a small overall increase in the mean torque.

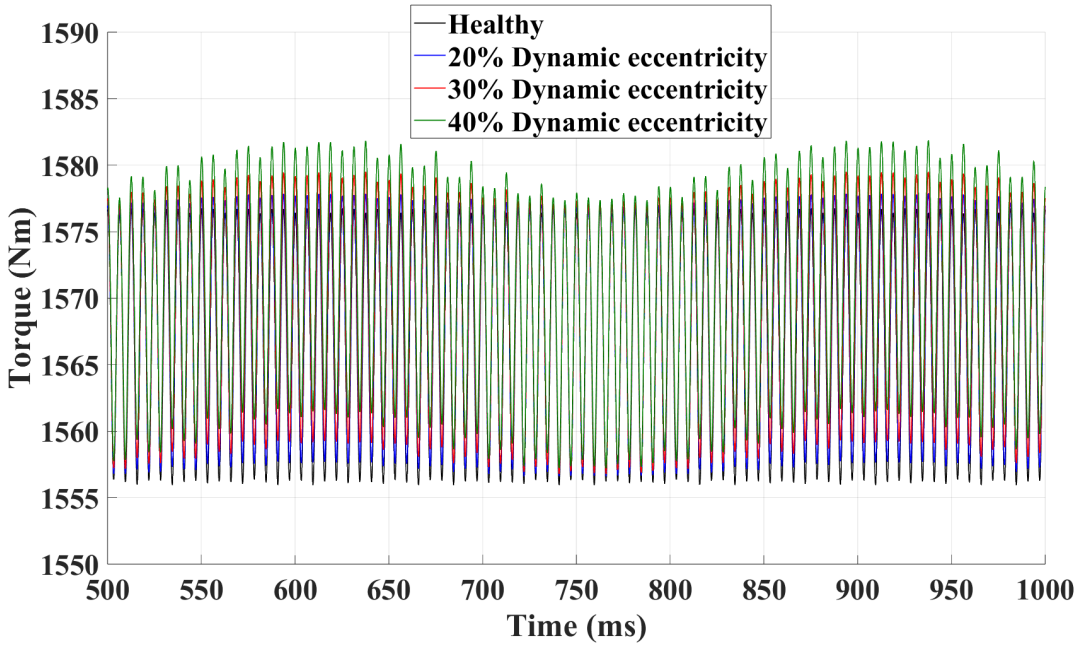

Figure 5.18. Torque Signal Under Dynamic eccentricity Fault with nominal Load

Another observation is that the ripple frequency introduced by the dynamic fault is very low, resulting in a harmonic component appearing close to 0 Hz. Specifically, the frequency of the ripple depends primarily on the mechanical rotational frequency of the rotor, which is given by $f_{\text{mech}} = \frac{f_s}{p}$, where f_s is the electrical supply frequency and p is the number of pole pairs. This behavior is characteristic of dynamic eccentricity faults, as they induce time-varying local variations in the flux of the coils, that modulate the torque at the rotor's mechanical frequency. For static eccentricity, the ripple frequency remains constant, while for dynamic eccentricity, the frequency varies periodically, leading to harmonics at f_{mech} and its multiples.

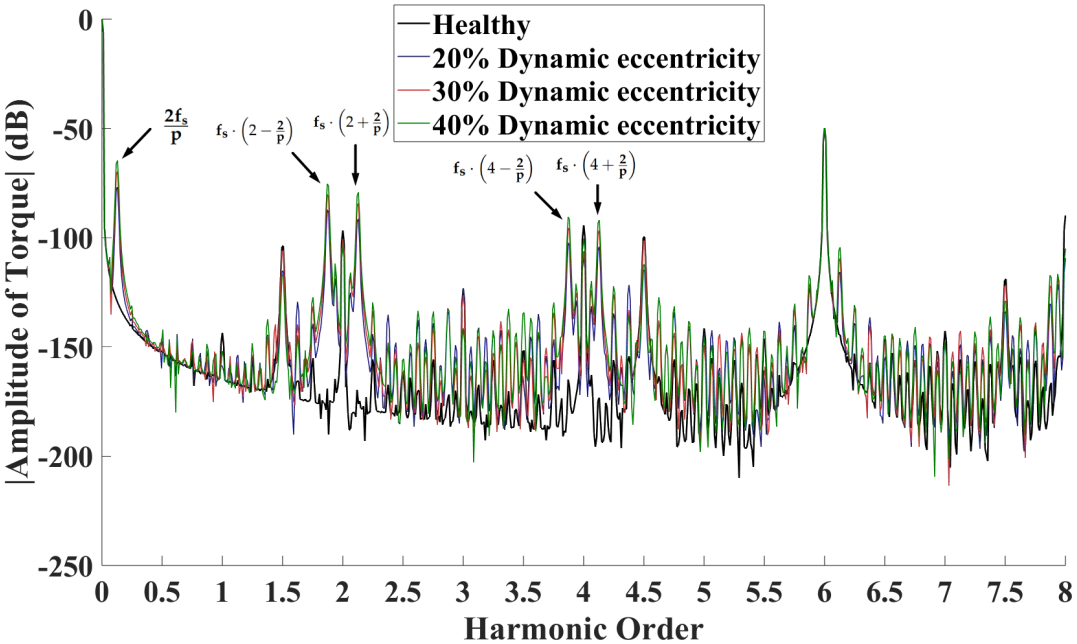

Figure 5.19. Torque Analysis Using FFT, Under dynamic eccentricity Fault

From the harmonic content of the torque signal, we observe an increase in the harmonic amplitudes at the frequencies described by Equation 3.25 for m = 2,

$$f_{\text{de}} = f_s \left(2k \pm \frac{2}{p}\right),$$

Table (5.12) provides the amplitudes of these harmonics under different percentages of dynamic eccentricity.

Table 5.12. Harmonic Amplitudes (dB) for Different Dynamic Eccentricity Cases

	$\frac{2f_s}{p}$	$f_s\left(2-\frac{2}{p}\right)$	$f_s\left(2+\frac{2}{p}\right)$	$f_s\left(4-\frac{2}{p}\right)$	$f_s\left(4+\frac{2}{p}\right)$
Healthy	-129.548	-169.044	-176.027	-164.950	-173.095
DE 20%	-76.7673	-87.215	-91.3244	-102.355	-104.095
DE 30%	-69.7189	-80.2008	-84.2497	-95.4974	-96.7763
DE 40%	-64.7254	-75.2076	-79.2591	-90.4997	-91.7895

An interesting observation is the absence of harmonics for $m = 1$ in the torque spectrum under dynamic eccentricity. The contribution of $m = 1$ harmonics, which are given by $f_s\left(2k \pm \frac{1}{p}\right)$, cancels out when the torque is synthesized from the three-phase currents. This phenomenon can possibly be attributed to the parallel connection of the coils in the circuit configuration of the machine.

The largest amplitude is observed at $2f_s/p$. This is because f_s/p corresponds to the rotor's fundamental mechanical frequency, which directly interacts with the machine's magnetic field and dominates the torque ripple.

It is evident that as the severity of the dynamic fault increases, the amplitude of these harmonics also increases. However, similar to the case of static eccentricity, the amplitudes between faulty conditions remain relatively small, even under the worst-case scenario of dynamic eccentricity. This is because the overall air-gap magnetic flux density remains largely unaffected. Consequently, the harmonic excitation is weak.

5.5.3 Mixed Eccentricity with Torque Monitoring

Mixed eccentricity is a combination of static eccentricity and dynamic eccentricity faults. To identify this fault, it is essential to apply a Fast Fourier Transform (FFT) on the torque signal to detect the characteristic fault signatures.

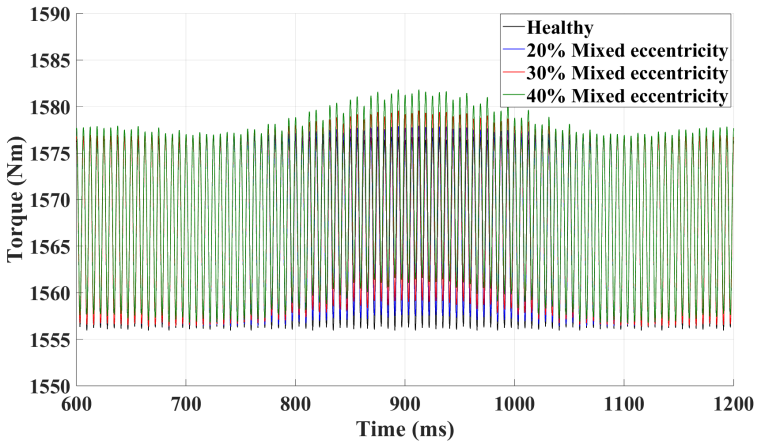

Figure 5.20. Torque Signal Under Mixed Eccentricity Fault with Nominal Load

From the harmonic content of the torque signal, we observe an increase in harmonic amplitudes at the frequencies described by Equation 3.25 for $m = 1, 2$:

$$f_{de} = f_s \left(2k \pm \frac{m}{p} \right),$$

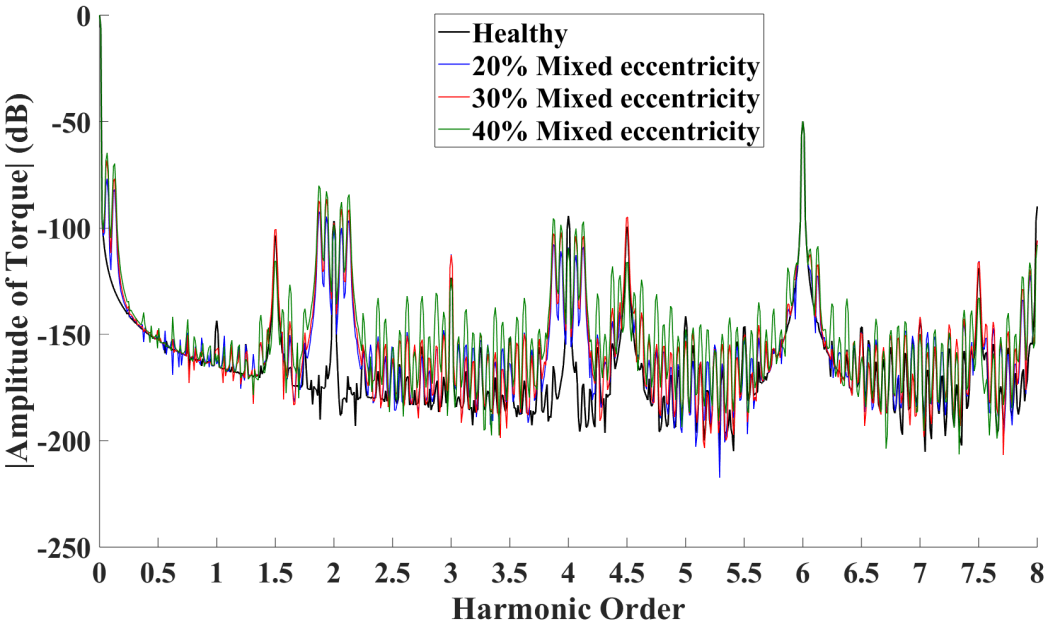

Figure 5.21. Torque Spectrum Under Mixed Eccentricity Fault with Nominal Load

Table 5.13 provides the amplitudes of these harmonics under different percentages of mixed eccentricity.

Table 5.13. Harmonic Magnitudes (dB) of Torque Signal under Healthy and Mixed Eccentricity Conditions

Condition	$\frac{f_s}{p}$	$\frac{2f_s}{p}$	$f_s(2-\frac{2}{p})$	$f_s(2-\frac{1}{p})$	$f_s(2+\frac{1}{p})$	$f_s(2+\frac{2}{p})$	$f_s(4-\frac{2}{p})$	$f_s(4-\frac{1}{p})$	$f_s(4+\frac{1}{p})$	$f_s(4+\frac{2}{p})$
Healthy (dB)	-117.29	-129.55	-169.05	-164.54	-187.5	-176.03	-164.95	-172.59	-162.76	-173.1
Mixed 20% (dB)	-76.728	-81.779	-92.23	-94.593	-99.839	-96.273	-107.53	-110.84	-112.61	-108.76
Mixed 30% (dB)	-68.256	-76.774	-87.237	-86.189	-91.156	-91.281	-102.54	-101.99	-103.78	-103.81
Mixed 40% (dB)	-64.741	-69.726	-80.188	-82.648	-87.661	-84.276	-95.373	-98.466	-100.37	-97.006

Interestingly, in the case of mixed eccentricity, the harmonics associated with $m = 1$ are not canceled, as was observed under dynamic eccentricity. This difference arises because, in mixed eccentricity, the three phases of the machine do not experience the fault's effects symmetrically over one complete rotation of the rotor. In contrast, under dynamic eccentricity, the asymmetry induced by the fault is distributed evenly across the three phases, leading to harmonic cancellation. Thus, while dynamic eccentricity exhibits harmonic cancellation, mixed eccentricity does not, allowing the $m = 1$ harmonics to remain present in the torque spectrum.

5.6 Flux Monitoring

As demonstrated, the MCSA is unable to produce distinctive fault signatures. Although several harmonics were observed in the coil current spectrum, the coil current signal cannot be obtained in practical applications. The next step is to install flux sensors inside the stator air gap in each coil, to obtain the flux per coil. The flux of the sensors can be utilized to detect the same distinctive fault signals as are produced in the coil current spectrum. One advantage of the flux sensor is its independency of the circuit design.

5.6.1 Flux Monitoring Under Static Eccentricity

The results of the Flux Monitoring method for different severity levels of the static eccentricity fault at the nominal load of 17.5 Ω are presented in Figure 5.22. The flux sensor was positioned at 0^o. The same spectrum is observed with the sensors positioned differently.

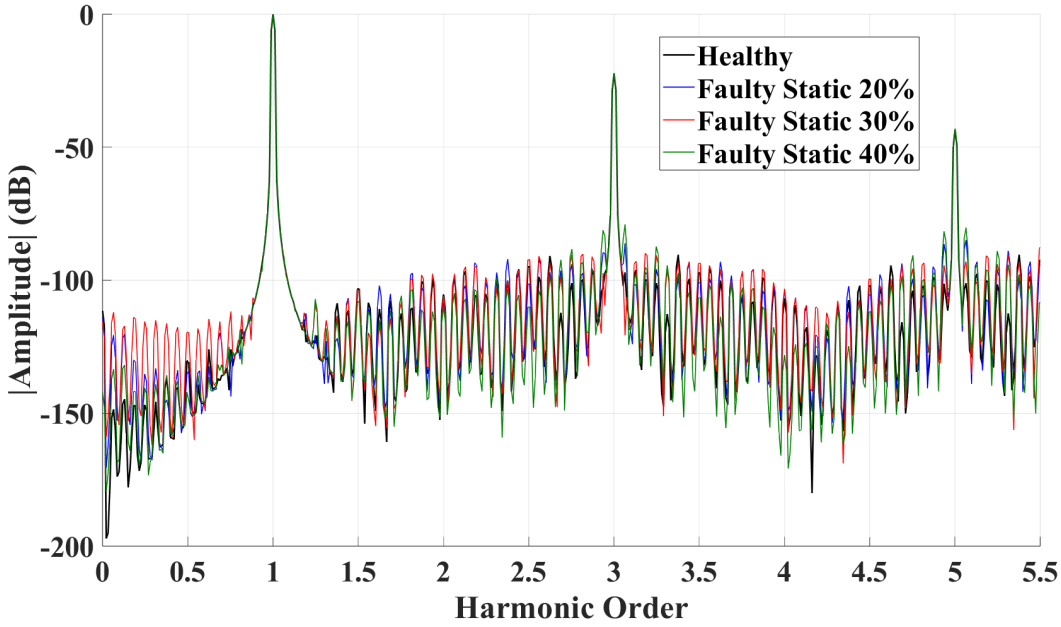

Figure 5.22. Flux Monitoring under static eccentricity Fault with nominal Load

Due to static eccentricity, each coil experiences a different flux depending on its location. These flux variations do not change with time because the eccentricity is static. Because the flux-variations are not time-dependent we expect a periodic behavior of the flux with frequency f_s.

In the coil current spectrum, an increase in the third harmonic was observed. However, this is not the case in the flux sensor spectrum, where the third harmonic is significant even under healthy conditions. This difference arises because the flux measured by the sensor is independent of the circuit connection. In contrast, in the coil current, the third harmonic cancels out due to the wye connection of the circuit.

As the severity of the static eccentricity fault increases, the amplitude of the 3rd harmonic in the flux sensor spectrum does not change. This is because the 3rd harmonic primarily results from the inherent nature of the flux signal, which arises due to the machine's structural design and magnetic properties. Static eccentricity introduces asymmetry in the air gap, but this does not further amplify the 3rd harmonic because its root cause is unrelated to the fault severity. Therefore, the amplitude of the 3rd harmonic remains unchanged under increasing fault severity. The method fails to produce characteristic fault signatures as seen (Figure 5.22)

Harmonics related to the static eccentricity fault $f_{\text{fault}} = \left(1 \pm \frac{k}{p}\right) f_s$ are not present in the flux sensor spectrum for the same reason they weren't present in the coil current spectrum. The presence of these sidebands is linked to the spatial asymmetry of the air-gap flux caused by static eccentricity. Although static eccentricity is a spatial phenomenon and does not vary with time, the rotor's motion interacts with the spatial asymmetry, resulting in periodic flux variations in each coil. However, the air-gap asymmetry ($g_{\text{se}} \approx g_{\text{healthy}}$) is minor in the C-GEN machine and such harmonics are not observed.

Table 5.14. Comparison of $3f_s$ amplitudes under healthy and static eccentricity conditions.

Condition	$3f_s$ Amplitude (dB)
Healthy	-22.3924
Static Eccentricity 20%	-22.1867
Static Eccentricity 30%	-22.132
Static Eccentricity 40%	-22.0888

5.6.2 Flux Monitoring Under Dynamic Eccentricity

The results of the Flux Monitoring method for different severity levels of the dynamic eccentricity fault at the nominal load of 17.5 Ω are presented in Figure 5.23. The flux sensor was positioned at 0^o.

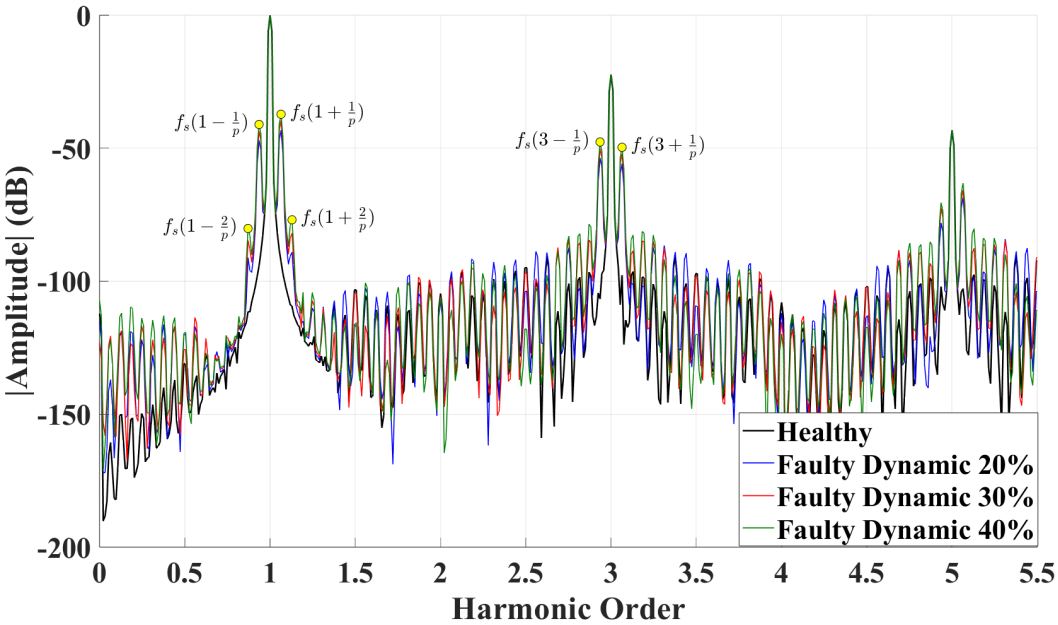

Figure 5.23. Flux Monitoring under dynamic eccentricity Fault with nominal Load

With the introduction of dynamic eccentricity, each coil experiences a time-varying flux. These variations, caused by the fault moving with the rotors, repeat after one full mechanical cycle of the machine. As the rotor completes one full rotation, the fault returns to the same relative position with respect to the coils, causing the flux variation to repeat periodically. After a 180° rotor rotation, a coil that was closer to one rotor due to the dynamic eccentricity (e.g., the inner rotor) will now be closer to the other rotor (e.g., the outer rotor). Consequently, the coil will be closer to the north pole magnet and further from the south pole, opposite to

its initial position. Because the rotor has rotated 180°, the flux of the coil will be opposite. However, the flux of the coil will not be perfectly opposite, as the two magnets have different widths and the coil will be closer to one of the magnets, opposite from before, changing slightly the reluctance and so the flux. Since the two magnets have different widths, this asymmetry introduces additional harmonics. These harmonics correspond to the periodic flux variations caused by the 180° rotation, which occur at twice the mechanical frequency.

This indicates that performing Fourier analysis on one of the flux sensors under dynamic eccentricity reveals harmonics at frequencies $f_s \pm \frac{kf_s}{p}$, where k is an integer and $\frac{f_s}{p}$ corresponds to the mechanical frequency of the rotor. This observation is shown in Figure 5.23 and Table 5.15.

Table 5.15. Harmonic Magnitudes (dB) of Flux Sensor under Healthy and Dynamic Fault Conditions

Condition	$f_s(1-\frac{2}{p})$	$f_s(1-\frac{1}{p})$	$f_s(1+\frac{1}{p})$	$f_s(1+\frac{2}{p})$	$f_s(3-\frac{1}{p})$	$f_s(3+\frac{1}{p})$
Healthy (dB)	-111.471	-94.2698	-92.6681	-109.535	-106.657	-97.6707
Dynamic 20% (dB)	-91.2859	-47.101	-43.2539	-89.1725	-53.6081	-55.8827
Dynamic 30% (dB)	-84.7656	-43.5799	-39.7232	-81.8746	-50.188	-52.1359
Dynamic 40% (dB)	-80.1805	-41.0795	-37.2236	-76.9214	-47.6616	-49.6684

From Table 5.15, when dynamic eccentricity occurs, harmonics appear at frequencies $f_s \pm \frac{kf_s}{p}$ as expected. We also observe sidebands at $\pm\frac{k}{p}$ around $3f_s$, which have smaller amplitudes compared to the sidebands around the fundamental frequency f_s, because they are higher order harmonics. The frequency signatures introduced by the 180° rotation ($k = 2$) have smaller amplitudes because the flux of the coil after 180° rotation, will not be opposite only by a small factor.

5.6.3 Flux Monitoring Under Mixed Eccentricity

The results of the Flux Monitoring method for different severity levels of the mixed eccentricity fault at the nominal load of 17.5 Ω are presented in Figure 5.24.

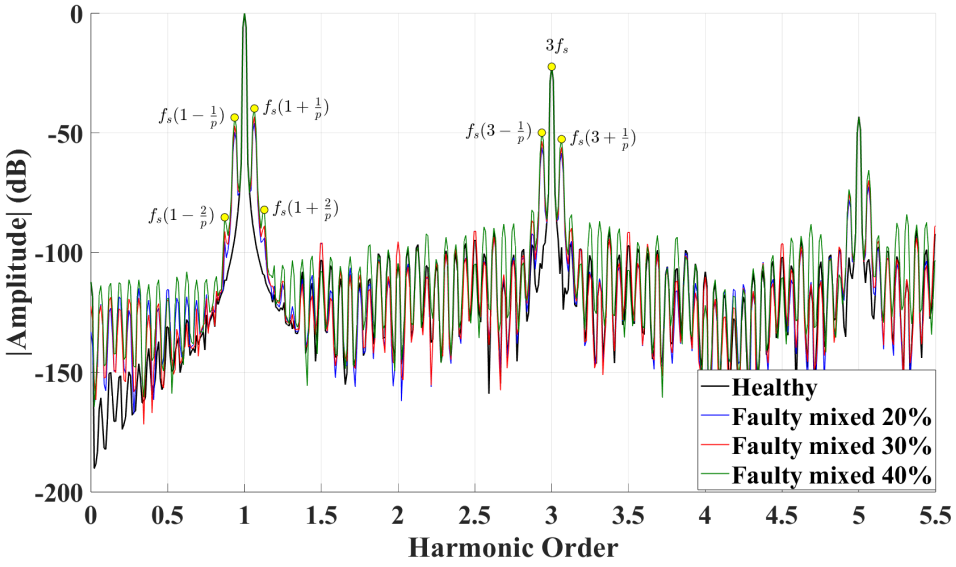

Figure 5.24. Flux Monitoring under mixed eccentricity Fault with nominal Load

Mixed eccentricity is a combination of static and dynamic eccentricity faults. The dynamic component of the mixed fault introduces flux variations in the coils, that repeat every full rotation of the machine. Additionally, due to the different magnet widths, harmonics linked to half rotation of the machine will be introduced, as was the case with dynamic eccentricity. As was explained in the flux monitoring under static eccentricity, the static component of the mixed fault is unable to produce characteristic fault signatures.

Performing Fourier analysis on the flux sensor signal under mixed eccentricity reveals harmonics at frequencies $f_s \pm \frac{kf_s}{p}$, where k is an integer and $\frac{f_s}{p}$ corresponds to the mechanical frequency of the rotor. Harmonics at $3f_s$ from the static component don't reveal change in amplitude. This observation is shown in Figure 5.24 and Table 5.16.

Table 5.16. Harmonic Magnitudes (dB) of Flux sensor under Healthy and Mixed Fault Conditions

Condition	$f_s(1-\frac{2}{p})$	$f_s(1-\frac{1}{p})$	$f_s(1+\frac{1}{p})$	$f_s(1+\frac{2}{p})$	$f_s(3-\frac{1}{p})$	$f_s(3+\frac{1}{p})$	$3f_s$
Healthy (dB)	-111.471	-94.2698	-92.6681	-109.535	-106.657	-97.6707	-22.3784
Mixed 20% (dB)	-95.4414	-49.5798	-45.7728	-93.9145	-56.1107	-58.3545	-22.3502
Mixed 30% (dB)	-91.1175	-47.0549	-43.2889	-88.8297	-53.4883	-55.9853	-22.3279
Mixed 40% (dB)	-85.2105	-43.5309	-39.7635	-82.0894	-49.8697	-52.5737	-22.3176

From Table 5.16, when mixed eccentricity occurs, harmonics appear at frequencies $f_s \pm \frac{kf_s}{p}$ as expected. We also observe sidebands at $\pm\frac{k}{p}$ around $3f_s$, which have smaller amplitudes compared to the sidebands around the fundamental frequency f_s, because they are higher order harmonics. The frequency signatures introduced by the 180° periodic behavior ($k = 2$) have smaller amplitudes because the full periodic behavior of the flux occurs every 360° (not 180°). The partial symmetry at 180° leads to weaker secondary flux variations, which are reflected as lower amplitudes at $k = 2$.

5.7 Magnetically Coupled Search-Coils

Using the previously discussed diagnostic methods, MCSA and flux monitoring, we were unable to detect all three types of eccentricity faults. Specifically, MCSA failed to detect any of the three faults, while flux monitoring was only capable of detecting the dynamic fault. To overcome this, we need a method capable of identifying all three types of eccentricity faults. As we will demonstrate, the search coil method effectively detects all three types of eccentricity.

5.7.1 Search Coil Method Under Static Eccentricity

To detect the static eccentricity fault two magnetically coupled coils are employed. One is placed in the rotor air gap and the other on the stator. The rotor search coil is short-circuited and the stator search coil is left open-circuited. Both coils share the same pitch and are designed to span 180°.

In a healthy machine, the magnetic flux across the air gap is symmetric, resulting in no current in the rotor search coil and, consequently, no induced voltage in the stator search coil. However, when a static fault occurs, such as static eccentricity in the C-GEN topology, the situation changes. Although the total air-gap flux remains constant, local variations in reluctance due to misaligned stator-rotor positioning cause the flux per coil to differ. These variations are static, but because the rotor is in motion, a time-varying voltage is induced in the rotor search coil, leading to a current. This current generates an MMF, producing an air-gap magnetic field that induces a time-varying flux in the stator search coil, resulting in an observable voltage.

This voltage is increased monotonically with the severity of the fault as observed in Figure 5.25.

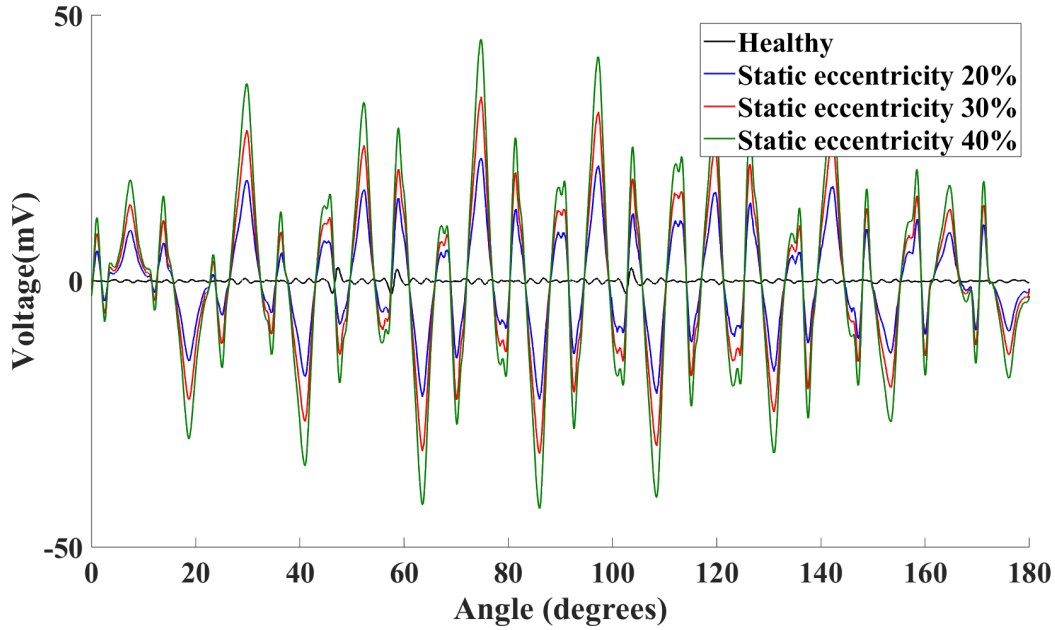

Figure 5.25. Stator Search Coil Voltage Under Static eccentricity Fault with nominal Load

The next step is to perform a Fast Fourier Transform (FFT) on the stator search coil voltage signal to obtain its frequency spectrum. This analysis will provide a deeper understanding of the fault characteristics.

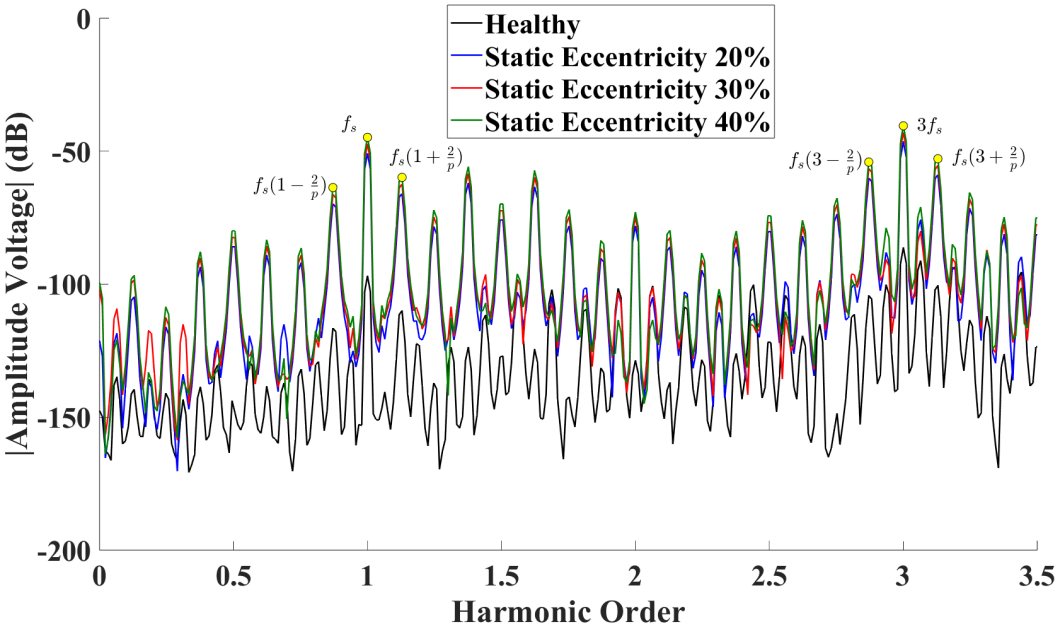

Figure 5.26. Stator Search Coil Voltage Spectrum Under Static eccentricity Fault with nominal Load

Table 5.17. Harmonic Magnitudes (dB) Under Different Severities of Static Eccentricity

Condition	$f_s(1-\frac{2}{p})$	f_s	$f_s(1+\frac{2}{p})$	$f_s(3-\frac{2}{p})$	$3f_s$	$f_s(3+\frac{2}{p})$
Healthy	-116.56	-96.854	-109.93	-104.28	-86.235	-100.54
Static 20%	-69.704	-50.802	-65.871	-60.116	-46.463	-58.81
Static 30%	-66.205	-47.302	-62.356	-56.582	-42.93	-55.296
Static 40%	-63.675	-44.795	-59.84	-54.073	-40.455	-52.832

As observed in Table 5.17 and Figure 5.26, there is a monotonic increase in the amplitudes of f_s and $3f_s$ with increasing fault severity. Additionally, the sidebands of f_s and $3f_s$ at $\pm\frac{2k}{p}$ also exhibit an increase. The term $\frac{2f_s}{p}$ corresponds to half a mechanical rotation of the machine, which matches the span of the search coils. The flux variations, which are time-varying because this method transforms a static fault into a dynamic one, repeat every half rotation of the machine. This behavior arises because the span of the rotor search coils matches half the machine. Since the fault is static, it remains fixed relative to the machine structure. Thus, after 180° of rotor rotation, the search coils interact with the same flux variations as they did 180° earlier. This symmetry ensures that the voltage induced in the stator search coil is identical after every 180° rotation.

The question that arises is how the harmonics at f_s and $3f_s$ increase in amplitude as the fault severity increases. It is suspected that these harmonics will appear even without the rotor coil. This can be verified by using the search coil method under static eccentricity without the rotor search coil. Figure (5.27).

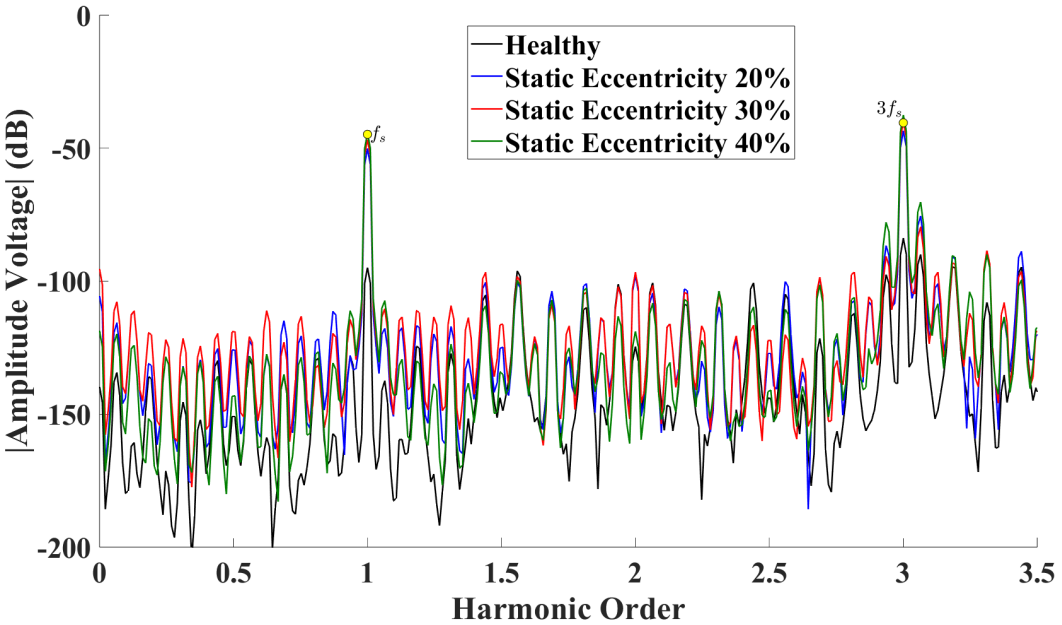

Figure 5.27. Stator Search Coil Voltage Spectrum Under Static eccentricity Fault without the rotor search coil

The rotor's magnetic field reverses its polarity every 180° electrical degrees. For machines with an even number of magnets, the net magnetic flux across any cross-section with the same span is zero in healthy conditions.

However, under static eccentricity, slight differences in reluctance between regions disrupt the symmetry of the healthy machine. This asymmetry results in a non-zero net flux across the stator search coil, causing the induced voltage to no longer sum to zero.

Table 5.18. Harmonic Magnitudes (dB) Under Different Severities of Static Eccentricity Without The Rotor Search Coil

Condition	f_s	$3f_s$
Healthy	-94.874	-83.903
Static 20%	-50.198	-43.539
Static 30%	-46.701	-40.009
Static 40%	-44.195	-37.529

The voltage induced in the stator search coil exhibits a periodic behavior with a frequency of f_s. This periodicity occurs because, after one electrical period of f_s, the rotor rotates to the same relative position with respect to the stator. As the fault is static, the stator search coil observes the same magnetic flux, every period of f_s. This explains how even without the rotor search coil, characteristic fault signatures can be produced under static eccentricity.

However, fault signatures are detected due to the specific position of the search coil, spanning from $-180°$ to $0°$, which is sensitive to the asymmetry introduced by the eccentricity fault at $0°$. If the eccentricity occurred at $90°$ instead of $0°$, the asymmetry would not be detected, and no voltage would be induced in the stator search coil.

This can be explained by noting that if the eccentricity is located at $90°$, the stator search coil that spans from $0°$ to $180°$ would experience the same flux distribution as in the healthy machine, because its position relative to the rotors wouldn't change. Consequently, the search coil would not detect any flux , making fault detection impossible in this configuration. To solve this two stator search coils can be installed with $90°$ difference to cover all the cases of static eccentricity.

5.7.2 Search Coil Method Under Dynamic Eccentricity

To detect the dynamic eccentricity fault, the rotor search coil is unnecessary. This is because dynamic variations inherently cause time-varying magnetic flux, directly inducing a voltage in the stator search coil. This voltage as in the static eccentricity fault, increases monotonically with the severity of the fault. This can be observed by Figure 5.28

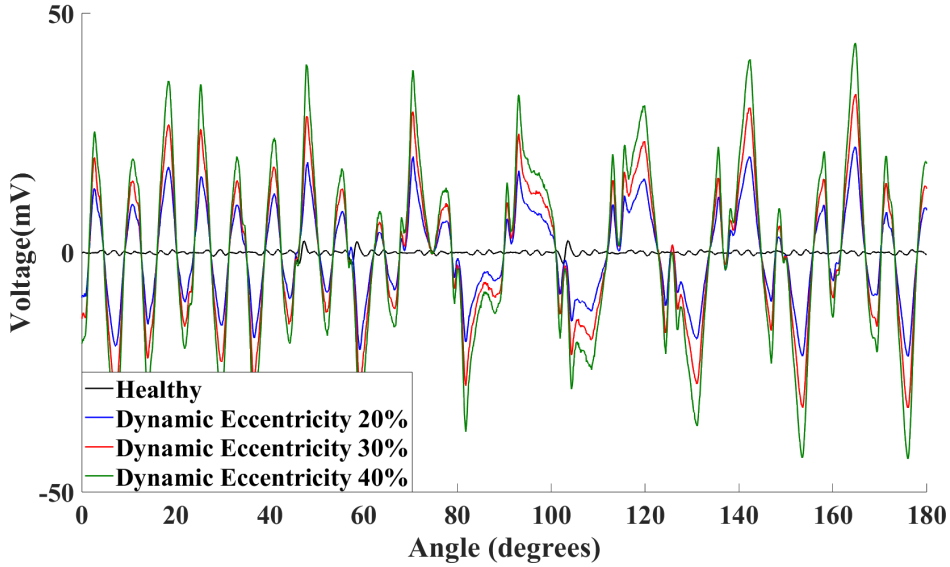

Figure 5.28. Stator Search Coil Voltage Under Dynamic Eccentricity Fault

The next step is to perform a Fast Fourier Transform (FFT) on the stator search coil voltage signal to obtain its frequency spectrum. This analysis will provide a deeper understanding of the fault characteristics.

Table 5.19. Harmonic Magnitudes (dB) Under Different Severities of Dynamic Eccentricity

Condition	$f_s(1-\frac{1}{p})$	$f_s(1+\frac{1}{p})$	$f_s(3-\frac{1}{p})$	$f_s(3+\frac{1}{p})$
Healthy	-128.01	-137.39	-97.453	-89.976
Dynamic 20%	-49.058	-52.911	-50.102	-49.263
Dynamic 30%	-45.542	-49.388	-46.741	-45.516
Dynamic 40%	-43.04	-46.888	-44.213	-43.011

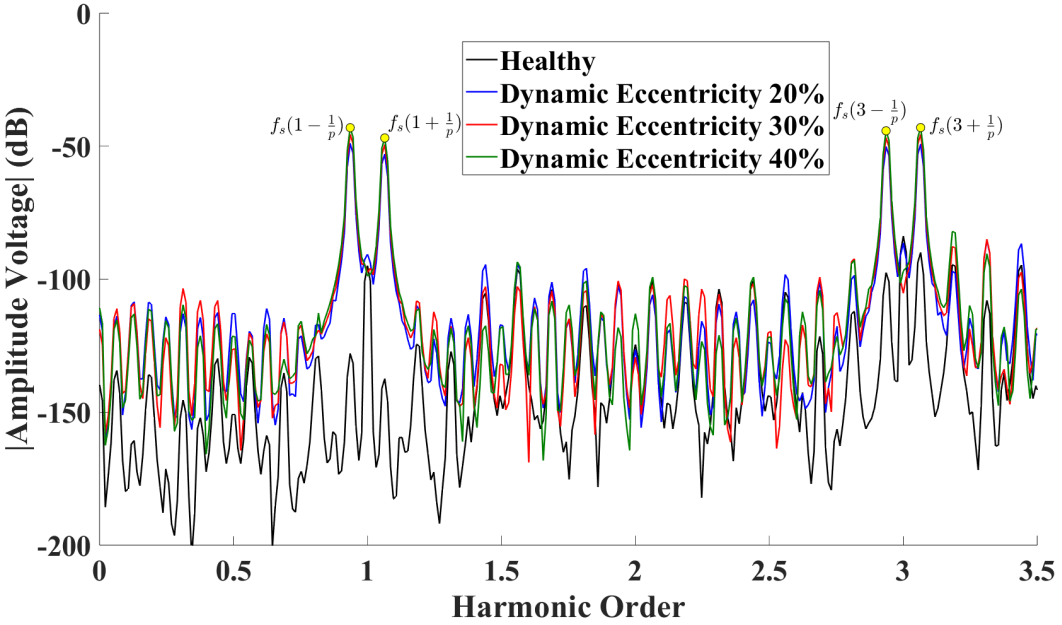

Figure 5.29. Stator Search Coil Voltage Spectrum Under Dynamic eccentricity Fault with nominal Load

As observed in Table 5.19 and Figure 5.29, there is a monotonic increase in the amplitudes of the sideband harmonics around f_s and $3f_s$ with increasing fault severity. With the introduction of the dynamic fault the stator search coil will have a time-varying flux. These variations, caused by the fault moving with the rotors, repeat after one full mechanical cycle of the machine. As the rotor completes one full rotation, the fault returns to the same relative position with respect to the stator search coil, causing the flux variation to repeat periodically. After 180° of rotor rotation, the flux of the stator search coil which spans 180°, will be completely opposite. So harmonics at $\frac{2f_s}{p}$ will not appear.

5.7.3 Search Coil Method Under Mixed Eccentricity

To detect the mixed eccentricity fault, only the stator search coil was used. Mixed eccentricity is a combination of static and dynamic eccentricity. Time-varying flux will induce voltage in the stator search coil. This voltage as in the static and dynamic eccentricity faults, increases monotonically with the severity of the fault. This can be observed by Figure (5.30). The problem with the signal in the time domain is that it is very difficult to differentiate between the three eccentricity faults. So the next step is to perform a Fast Fourier Transform (FFT) on the stator

search coil voltage signal to obtain its frequency spectrum. This analysis will provide a deeper understanding of the fault characteristics. The stator search coil voltage signal in the frequency domain is observed in Figure (5.31).

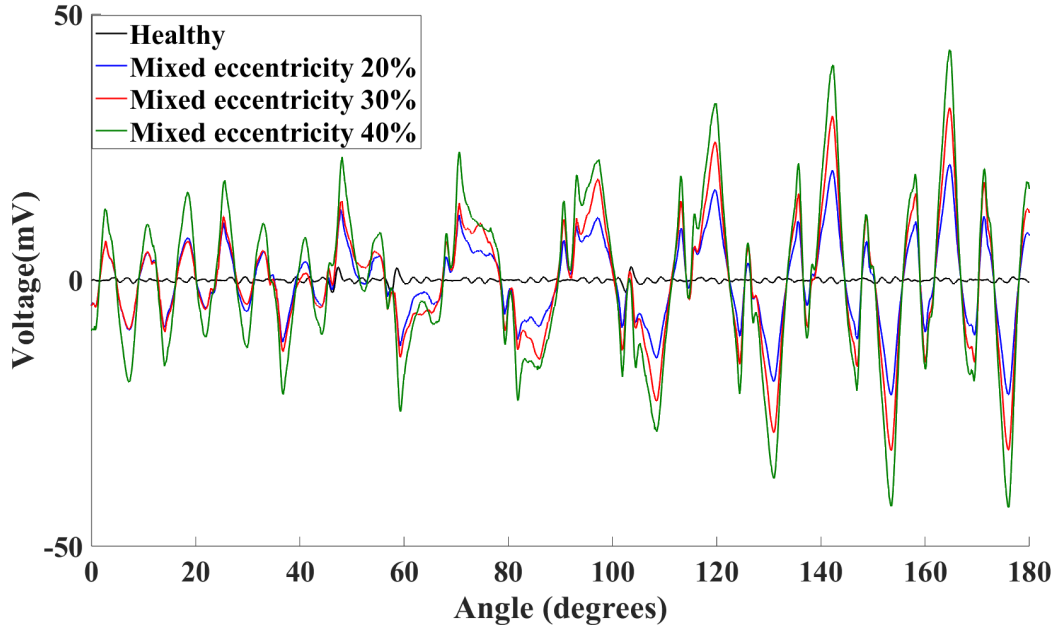

Figure 5.30. Stator Search Coil Voltage Under Mixed Eccentricity Fault

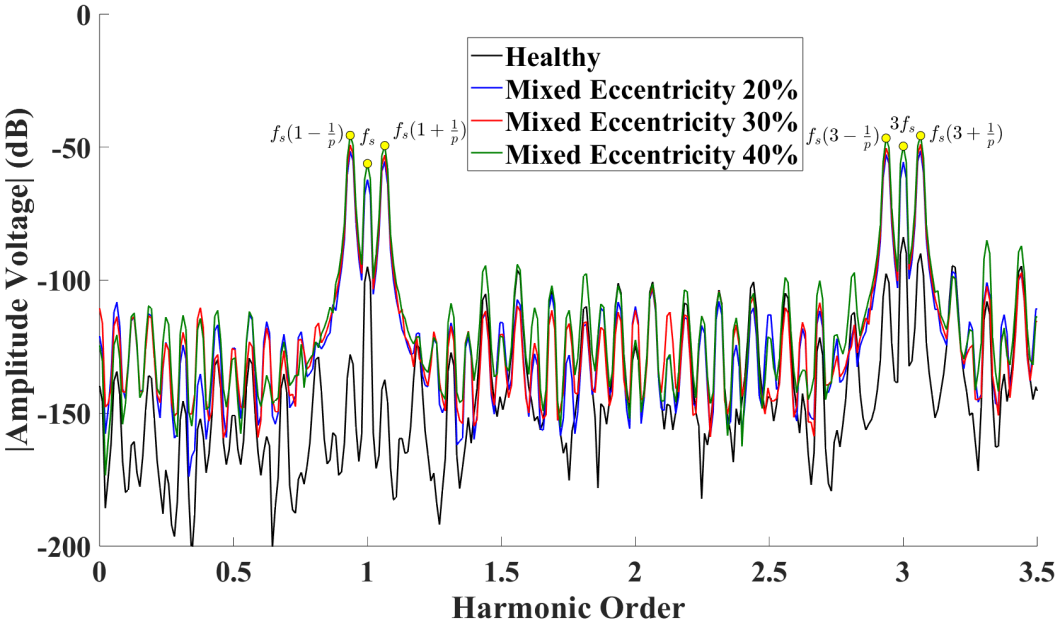

Figure 5.31. Stator Search Coil Voltage Spectrum Under Mixed eccentricity Fault with nominal Load

Table 5.20. Harmonic Magnitudes (dB) Under Different Severities of Mixed Eccentricity

Condition	$f_s(1-\frac{1}{p})$	f_s	$f_s(1+\frac{1}{p})$	$f_s(3-\frac{1}{p})$	$3f_s$	$f_s(3+\frac{1}{p})$
Healthy	-128.01	-94.874	-137.39	-97.453	-83.903	-89.976
Mixed 20%	-51.558	-62.114	-55.408	-52.712	-55.674	-51.371
Mixed 30%	-49.06	-56.167	-52.906	-50.2	-49.611	-48.891
Mixed 40%	-45.537	-56.161	-49.384	-46.591	-49.616	-45.642

From Table 5.20, it can be observed that the increase in the harmonics at $f_s(1 \pm \frac{1}{p})$ and $3f_s(1 \pm \frac{1}{p})$ is attributed to the dynamic component of the fault, while the increase in the harmonics at f_s and $3f_s$ is caused by the static component of the fault. Additionally, the amplitudes of the first and third harmonics do not increase between the 30% and 40% eccentricity faults. This is because the same percentage of static eccentricity was applied in both the 30% mixed and 40% mixed fault conditions. Sideband harmonics $\frac{2f_s}{p}$ were not observed because the rotor search coil was not used.

5.8 Zero-Sequence-Flux Analysis

The zero-sequence component (ZSC) has a fundamental frequency of $3f_s$, which results in a higher signal amplitude compared to the individual sensor outputs. This enhanced amplitude increases the magnitude of the characteristic fault signatures harmonics, allowing for more accurate detection of faults. The method also is able to detect both static and dynamic faults and differentiate between them. Thus the ZSF method provides clear advantages compared to traditional methods like MCSA.

5.8.1 ZSF Under Static Eccentricity

Under healthy conditions the three flux sensors have the same flux with 120° electrical difference. When we add the signals from the three flux sensors it will result to a signal with fundamental frequency $3f_s$ where harmonics at frequencies $(6k \pm 1)f_s$ (e.g, 1st, 5th, 7th,...) cancel out. Under Static eccentricity, local variations in reluctance due to misaligned stator-rotor positioning causes the flux to differ among the three sensors. As a result, the amplitudes of the three induced voltages are no longer equal, and their summation no longer cancels out the $(6k \pm 1)f_s$ harmonics. The amplitudes of these harmonics increase monotonically with the severity of the fault, making it a clear indicator of static faults.

The ZSF analysis can be implemented with two different strategies. Firstly, the three flux sensors are placed 120 electrical degrees apart and secondly 120 mechanical degrees apart. Although in this application, both methods can be easily applied, in different machine types there may be applicability issues due to the external geometry of the tested machine, therefore one of the two may be implemented.

ZSF With the Sensors placed 120° electrically apart Under Static Fault

The results of the ZSF method for different severity levels of the static eccentricity fault at the nominal load of 17.5 Ω are presented in Figure 5.32 and Table 5.21. The flux sensors were positioned mechanically at $0^o, 15^o, 30^o$.

Table 5.21. Harmonic Magnitudes (dB) Under Different Severities of Static Eccentricity (120° electrically apart)

Condition	f_s (1st Harmonic)	$5f_s$ (5th Harmonic)
Healthy	-48.492	-62.098
Static 20%	-38.876	-60.913
Static 30%	-35.303	-59.370
Static 40%	-32.735	-58.513

As expected the amplitudes of the harmonics f_s and $5f_s$ increase with the severity of the fault, making it a clear indicator of a static fault. This can be easily seen by Figure 5.33.

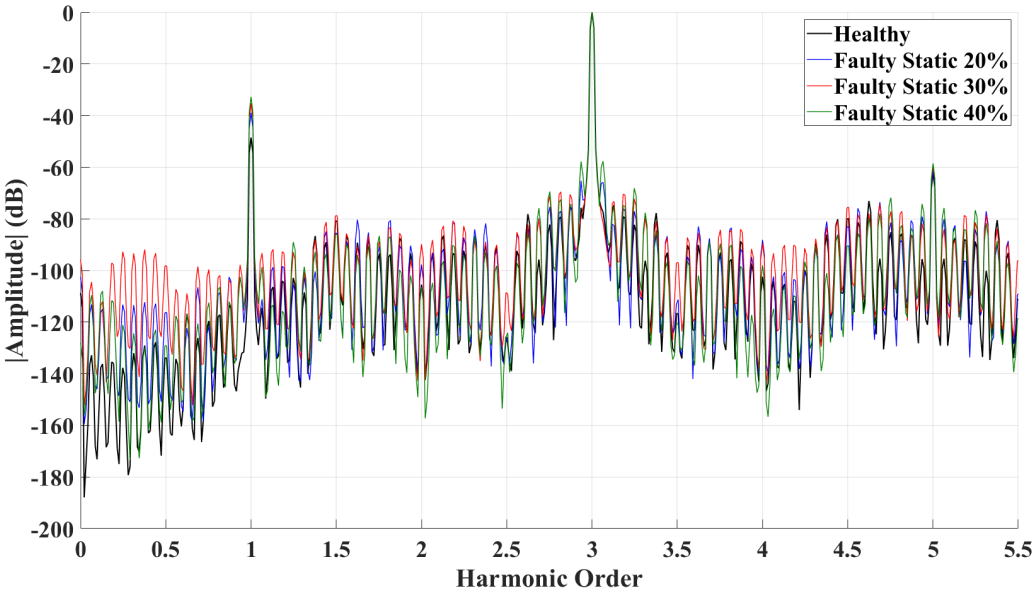

Figure 5.32. ZSF Under Static Eccentricity Fault (120° electrically apart)

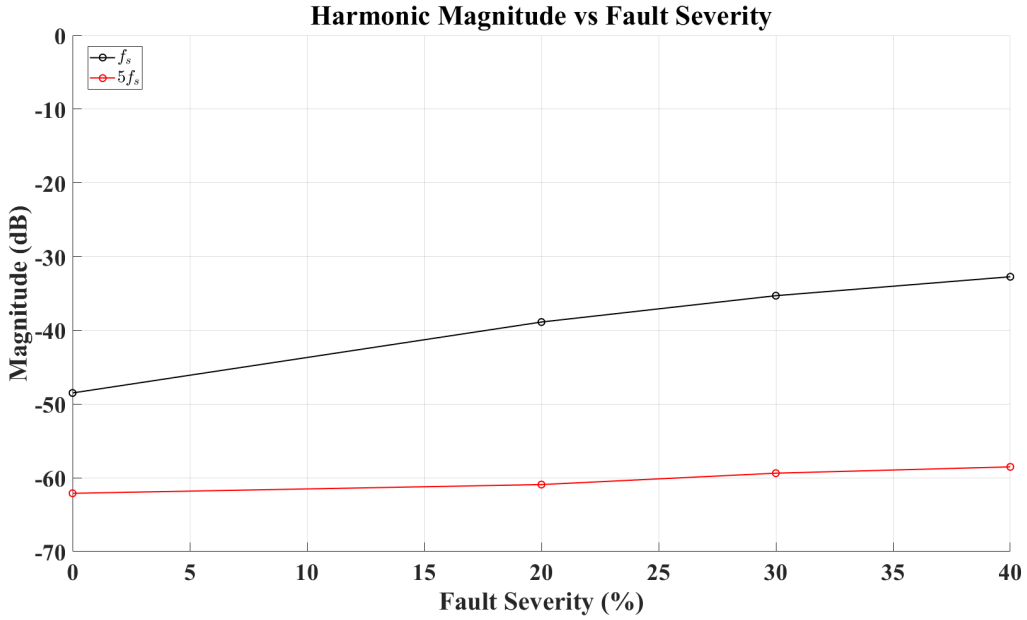

Figure 5.33. Harmonic Magnitude of 1st,5th harmonic vs Static Eccentricity Fault Severity (120° electrically apart)

From Table 5.21 and Figure 5.33, it can be observed that the healthy machine exhibits relatively weak harmonics at f_s (-48.492 dB) and $5f_s$ (-62.098 dB). Ideally, these harmonics should not exist in a healthy machine but appear due to minor asymmetries caused by the non-linear characteristics of the permanent magnets and inherent minor model imperfections. When static eccentricity is introduced, these harmonics increase in amplitude. Furthermore, their growth is monotonic with the severity of the fault level. The 5th harmonic is a higher order harmonic which is naturally attenuated and thus even under static eccentricity the amplitude of the 5th increases only by a small factor ($\approx 1dB$).

ZSF With the Sensors placed 120° mechanically apart Under Static Fault

The results of the ZSF method for different severity levels of the static eccentricity fault at the nominal load of 17.5 Ω are presented in Figure 5.34 and Table 5.22. The flux sensors were positioned mechanically at $0^o, 120^o, 240^o$.

Table 5.22. Harmonic Magnitudes (dB) Under Different Severities of Static Eccentricity (120° mechanically apart)

Condition	f_s (1st Harmonic)	$5f_s$ (5th Harmonic)
Healthy	-48.476	-61.977
Static 20%	-23.757	-47.338
Static 30%	-20.142	-43.048
Static 40%	-17.609	-40.52

As expected the amplitudes of the harmonics f_s and $5f_s$ increase with the severity of the fault, making it a clear indicator of a static fault. This can be easily seen by Figure 5.35.

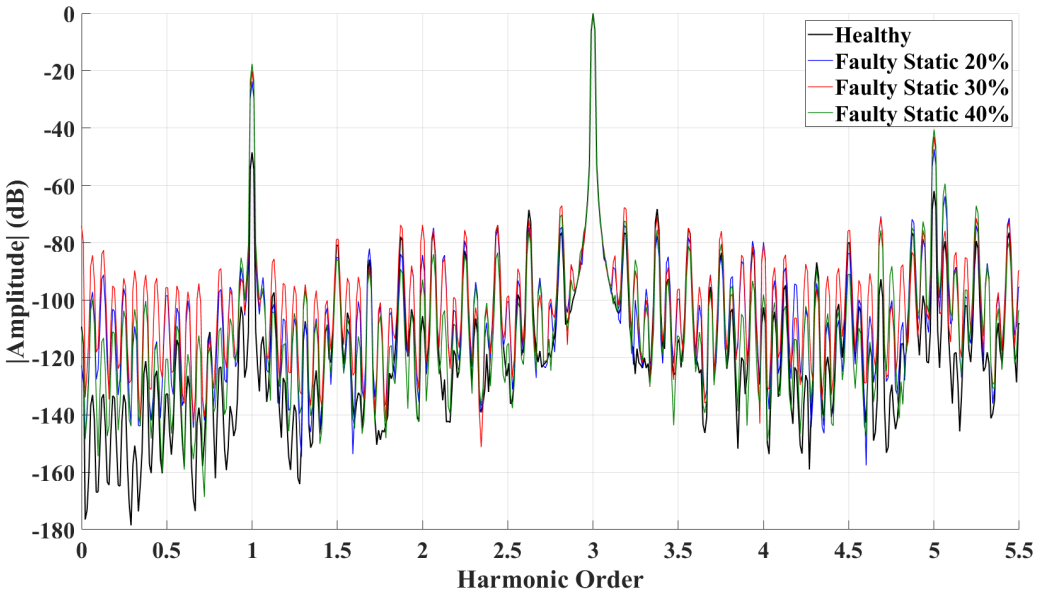

Figure 5.34. ZSF Under Static Eccentricity Fault (120° mechanically apart)

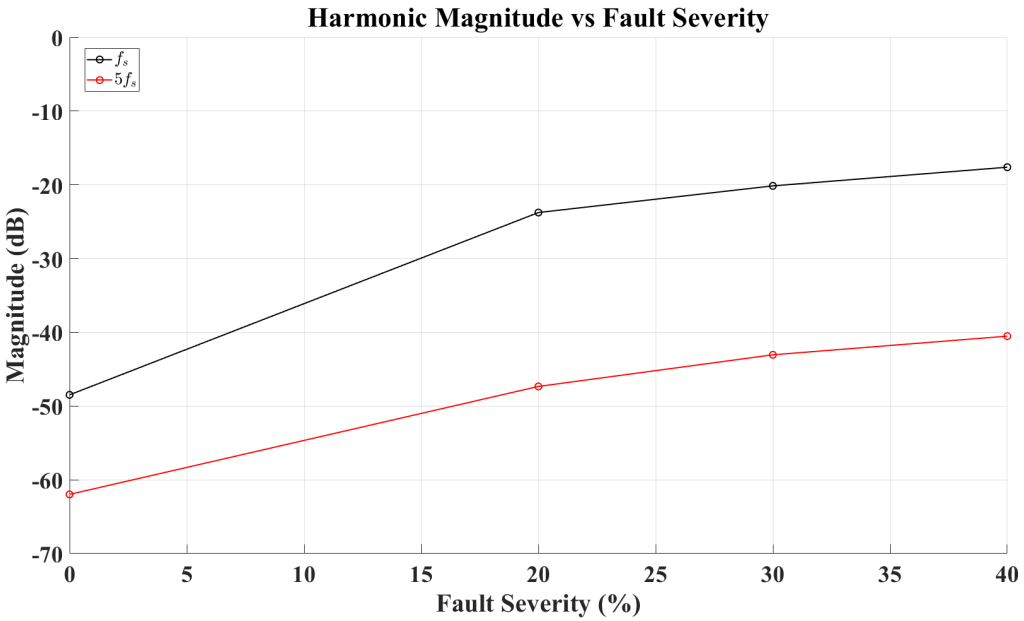

Figure 5.35. Harmonic Magnitude of 1st,5th harmonic vs Static Eccentricity Fault Severity (120° mechanically apart)

From Table 5.22 and Figure 5.33, it can be observed that when static eccentricity is introduced, the 1st and 5th harmonics increase significantly in amplitude. Compared to the ZSF method with the sensors placed 120 deg electrically apart, the sensitivity of the method is enhanced when the three sensors are placed at 120 mechanical degrees from each other. This result is reasonable because sensors spaced 120 mechanical degrees apart are physically farther apart in the stator frame, allowing them to capture bigger variations in the magnetic flux between the three sensors, caused by the static eccentricity fault. Despite the weaker results, the methodology using sensors placed 120 electrical degrees apart can still successfully identify the fault to some extent. While the smaller physical spacing leads to reduced sensitivity, the same harmonics can be observed.

5.8.2 ZSF Under Dynamic Eccentricity

Under dynamic eccentricity, the rotor's motion creates time-varying changes in the flux of each coil. These variations occur uniformly across the three sensors, resulting in identical signals with a phase shift of 120°. This symmetry ensures that harmonics at $(6k \pm 1)f_s$ (e.g., the 1st, 5th, and 7th harmonics) still cancel out, as in the healthy condition. The time-varying variations in the flux of each coil, repeat with every full rotation of the machine. These variations generate sideband harmonics $\frac{kf_s}{p}$, around the main frequencies $(6k \pm 1)f_s$ as well as the 3$^{\text{rd}}$ harmonic.

As in the case with static eccentricity, the method can be used with two different strategies. The three flux sensors are placed 120 electrical degrees apart and 120 mechanical degrees apart.

ZSF With the Sensors placed 120° electrically apart under Dynamic Fault

The results of the ZSF method for different severity levels of the dynamic eccentricity fault at the nominal load of 17.5 Ω are presented in Figure 5.36 and Table 5.23. The flux sensors were positioned mechanically at $0^o, 15^o, 30^o$.

Table 5.23. Harmonic Magnitudes (dB) of Flux Sensor under Healthy and Dynamic Eccentricity Conditions (120° electrically apart)

Condition	$f_s(1-\frac{2}{p})$	$f_s(1-\frac{1}{p})$	$f_s(1+\frac{1}{p})$	$f_s(1+\frac{2}{p})$	$f_s(3-\frac{1}{p})$	$f_s(3+\frac{1}{p})$	$f_s(5-\frac{1}{p})$	$f_s(5+\frac{1}{p})$
Healthy (dB)	-114.7	-135.17	-114.44	-106.37	-75.713	-77.312	-95.57	-95.448
Dynamic 20% (dB)	-82.227	-38.176	-42.533	-76.452	-30.619	-31.9	-71.481	-62.545
Dynamic 30% (dB)	-77.084	-34.675	-39.022	-68.92	-27.242	-28.21	-66.19	-59.808
Dynamic 40% (dB)	-70.86	-32.159	-36.521	-63.875	-24.714	-25.728	-64.16	-57.114

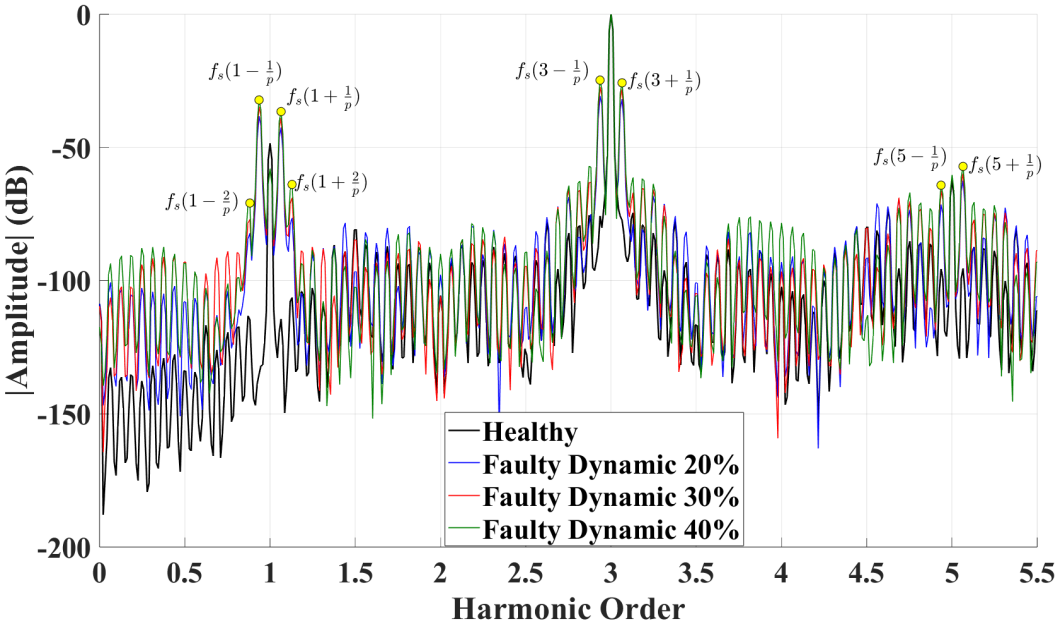

Figure 5.36. ZSF Under Dynamic Eccentricity Fault (120° electrically apart)

From the results, we observe sideband harmonics at frequencies that are multiples of the mechanical frequency $\frac{f_s}{p}$. Each sensor, when analyzed using the flux monitoring method under dynamic eccentricity, exhibits these sideband frequencies.

When the flux signals from the three sensors are combined, these harmonics appear amplified in the spectrum. The sideband harmonics at the fundamental frequency $3f_s$ showcase the fault signatures more prominently. Under healthy conditions, these harmonics are absent in the flux spectrum of each coil, and therefore, they do not appear in the Zero-Sequence Flux (ZSF) method.

Figure 5.37 illustrates the harmonic magnitudes of the characteristic fault frequencies in relation to the dynamic fault severity. The harmonics closer to the fundamental $3f_s$ exhibit the largest amplitude, followed by the sidebands at the first-order harmonic for $k = 1$. For $k = 2$, the magnitudes are smaller, as explained in the flux monitoring method.

In general, there is a monotonic increase in the amplitude of these harmonics as the fault severity increases.

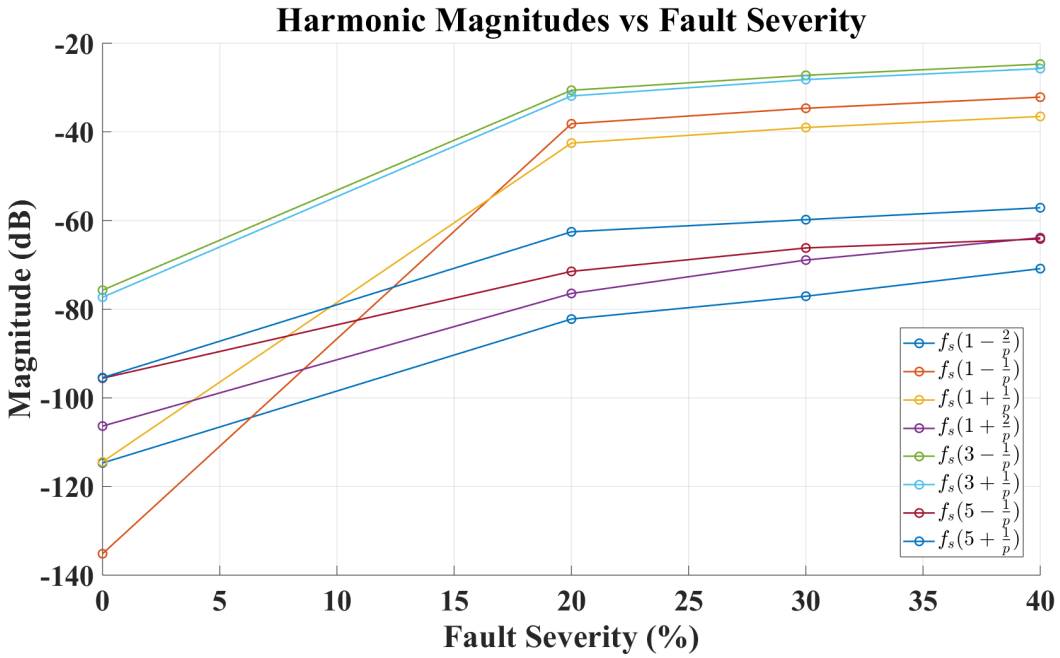

Figure 5.37. Harmonic Magnitude of harmonic vs Dynamic Eccentricity Fault Severity (120° electrically apart)

ZSF With the Sensors placed 120° mechanically apart under Dynamic Fault

The results of the ZSF method for different severity levels of the dynamic eccentricity fault at the nominal load of 17.5 Ω are presented in Figure 5.38 and Table 5.24. The flux sensors were positioned mechanically at $0^o, 120^o, 240^o$.

Table 5.24. Harmonic Magnitudes (dB) of Flux Sensor under Healthy and Dynamic Eccentricity Conditions (120° mechanically apart)

Condition	$f_s(1-\frac{1}{p})$	$f_s(1+\frac{1}{p})$	$f_s(1+\frac{2}{p})$	$f_s(3-\frac{1}{p})$	$f_s(3+\frac{1}{p})$	$f_s(5-\frac{1}{p})$	$f_s(5+\frac{1}{p})$
Healthy (dB)	-102.21	-112.64	-97.288	-83.229	-85.388	-98.407	-79.452
Dynamic 20% (dB)	-22.613	-35.39	-67.209	-51.62	-55.172	-74.342	-45.905
Dynamic 30% (dB)	-19.097	-31.86	-59.933	-48.193	-51.495	-69.134	-43.221
Dynamic 40% (dB)	-16.606	-29.373	-54.804	-45.775	-49.191	-67.18	-40.554

From the results, we observe the same sideband harmonics as were observed when the three flux sensors were placed 120° electrically apart.

Figure 5.39 illustrates the harmonic magnitudes of the characteristic fault frequencies compared to the dynamic fault severity. Interestingly, the sideband harmonics at the fundamental $3f_s$ now have smaller amplitudes compared to the harmonics around f_s. This is expected because the third harmonic sidebands now exhibit a phase difference close to 120° between the sensors.

In general, to calculate the electric phase of a harmonic, we use the formula:

$$\theta_{\text{el}} = n\frac{p}{2}\theta_{\text{mech}} \tag{5.2}$$

Substituting n (harmonic order) for a specific harmonic around $3f_s$, we find that the phase of this harmonic for the three sensors, mechanically placed at 0°, 120°, and 240°, will exhibit a phase difference close to 120° between the sensors. Consequently, when these harmonics are

summed, they are attenuated. On the other hand, for the first harmonic, the three flux sensors have a small phase difference, resulting in a significant harmonic amplitude when added.

As in the case where the three flux sensors were placed 120° electrically apart, there is a monotonic increase in the characteristic fault harmonics with the increase in the severity level of the dynamic fault.

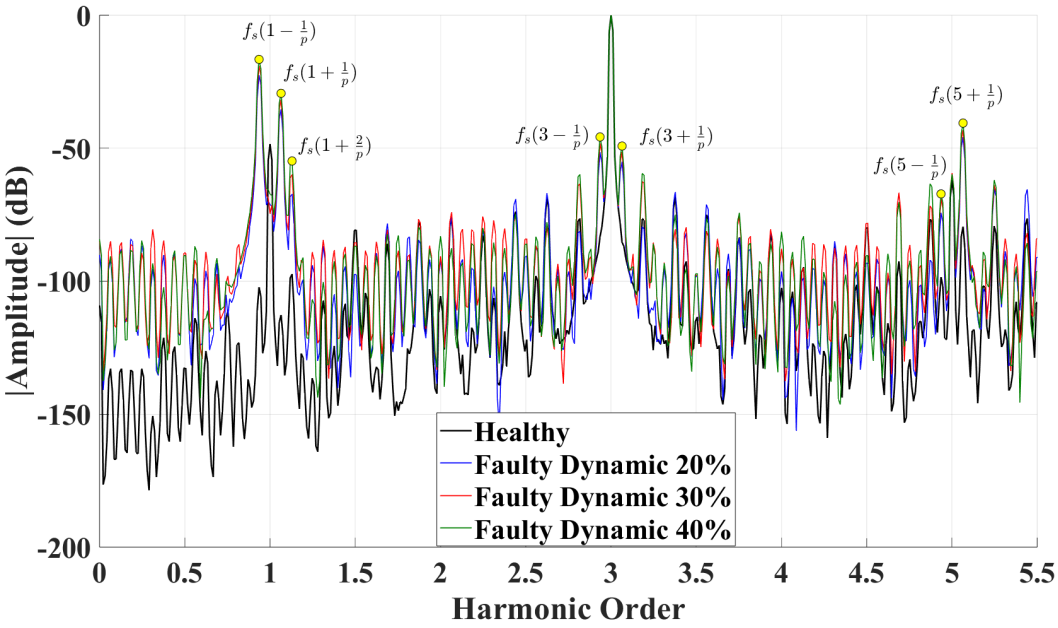

Figure 5.38. ZSF Under Dynamic Eccentricity Fault (120° mechanically apart)

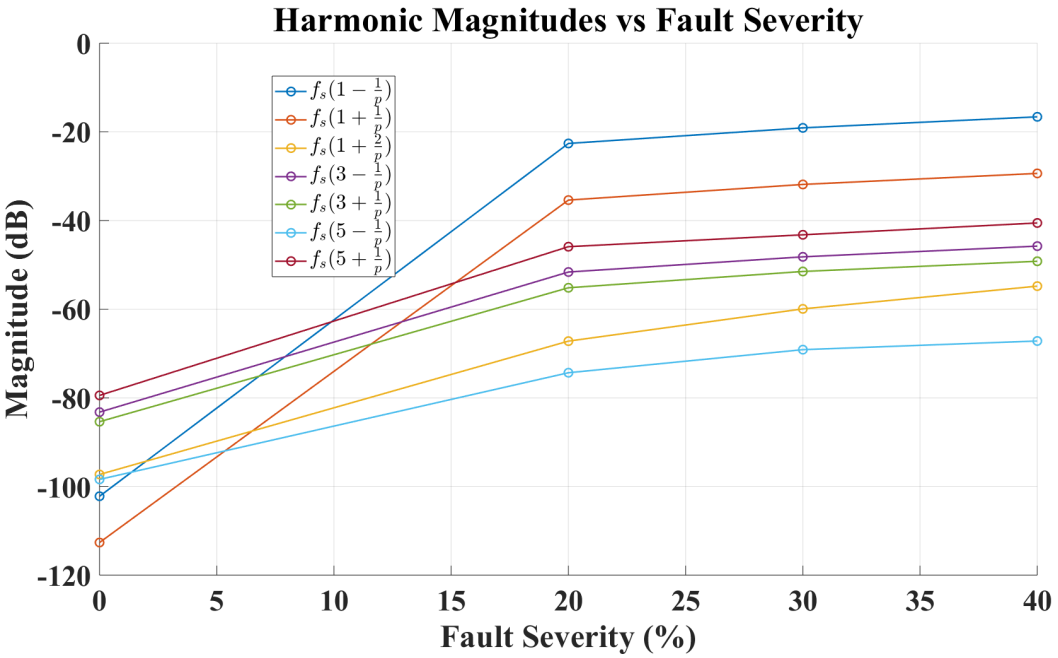

Figure 5.39. Harmonic Magnitude of harmonic vs Dynamic Eccentricity Fault Severity (120° mechanically apart)

5.8.3 ZSF Under Mixed Eccentricity

Mixed eccentricity is a combination of static and dynamic eccentricity faults. The static component of the fault produces characteristic fault signatures at frequencies $(6k \pm 1)f_s$, because the three sensors experience different flux amplitudes due to the fault.

On the other hand, the dynamic component introduces characteristic fault signatures at the sidebands of the frequencies $(6k \pm 1)f_s$ as well as the fundamental third harmonic. These sidebands are related to the mechanical frequency of the rotor, given by $\frac{f_s}{p}$.

Mixed eccentricity combines the effects of both static and dynamic faults and, consequently, will produce characteristic fault signatures corresponding to both types of faults.

As with static and dynamic eccentricity, the Zero Sequence Flux (ZSF) method can be employed in two different configurations:

1. The flux sensors are placed 120° electrically apart.
2. The flux sensors are placed 120° mechanically apart.

ZSF With the Sensors placed 120° electrically apart Under Mixed Fault

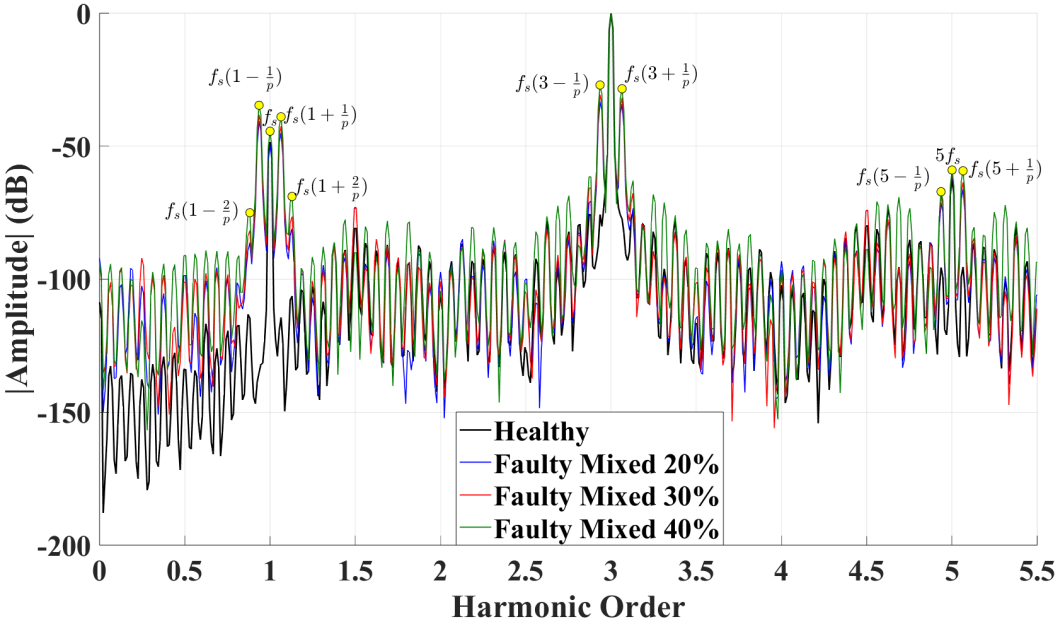

Figure 5.40. ZSF Under Mixed Eccentricity Fault (120° electrically apart)

The results of the ZSF method for different severity levels of the mixed eccentricity fault at the nominal load of 17.5 Ω are presented in Figure 5.40 and Table 5.25. The flux sensors were positioned mechanically at $0^o, 15^o, 30^o$.

Table 5.25. Harmonic Magnitudes (dB) of Flux Sensor under Healthy and Mixed Eccentricity Conditions (120° electrically apart)

Condition	$f_s(1-\frac{2}{p})$	$f_s(1-\frac{1}{p})$	f_s	$f_s(1+\frac{1}{p})$	$f_s(1+\frac{2}{p})$	$f_s(3-\frac{1}{p})$	$f_s(3+\frac{1}{p})$	$f_s(5-\frac{1}{p})$	$5f_s$	$f_s(5+\frac{1}{p})$
Healthy (dB)	-114.7	-135.17	-48.492	-114.44	-106.37	-75.713	-77.312	-95.57	-62.098	-95.448
Mixed 20% (dB)	-86.28	-40.638	-49.531	-44.975	-80.922	-33.175	-34.268	-71.293	-60.119	-66.192
Mixed 30% (dB)	-81.769	-38.105	-44.39	-42.474	-76.469	-30.596	-31.804	-68.755	-59.469	-63.524
Mixed 40% (dB)	-75.026	-34.6	-44.359	-38.953	-68.9	-26.989	-28.39	-67.115	-58.955	-59.244

As expected, the characteristic fault signatures observed in mixed eccentricity faults are a combination of the characteristic frequencies associated with dynamic and static faults. The increase in amplitude of the sidebands around the 1st, 3rd, and 5th harmonics highlights the dynamic fault component, while the increase at the 1st and 5th harmonics indicates the static fault component.

Similar to the case of dynamic faults, the sidebands around the fundamental frequency exhibit the largest increase in amplitude. This occurs because the phase differences at these harmonics between the flux sensors are small, leading to a combination that amplifies these harmonics.

ZSF With the Sensors placed 120° mechanically apart Under Mixed Fault

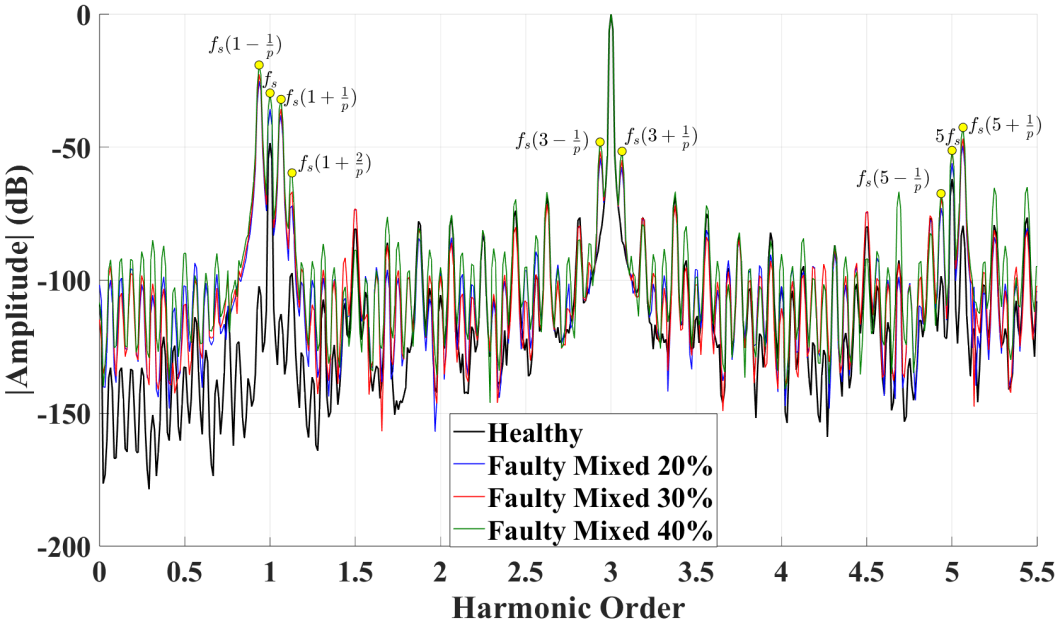

Figure 5.41. ZSF Under Mixed Eccentricity Fault (120° mechanically apart)

The results of the ZSF method for different severity levels of the mixed eccentricity fault at the nominal load of 17.5 Ω are presented in Figure 5.41 and Table 5.26. The flux sensors were positioned mechanically at $0^O, 120^o, 240^o$.

Table 5.26. Harmonic Magnitudes (dB) of Flux Sensor under Healthy and Mixed Eccentricity Conditions (120° mechanically apart)

Condition	$f_s(1-\frac{1}{p})$	f_s	$f_s(1+\frac{1}{p})$	$f_s(1+\frac{2}{p})$	$f_s(3-\frac{1}{p})$	$f_s(3+\frac{1}{p})$	$f_s(5-\frac{1}{p})$	$5f_s$	$f_s(5+\frac{1}{p})$
Healthy (dB)	-102.21	-48.476	-112.64	-97.288	-83.229	-85.388	-98.407	-61.977	-79.452
Mixed 20% (dB)	-25.104	-35.688	-37.936	-72.056	-54.134	-57.472	-72.855	-56.089	-49.353
Mixed 30% (dB)	-22.601	-29.64	-35.504	-66.882	-51.64	-54.93	-69.244	-51.599	-46.761
Mixed 40% (dB)	-19.089	-29.64	-31.992	-59.672	-48.055	-51.538	-67.438	-51.207	-42.555

From the results, we observe the same sideband harmonics as were observed when the three flux sensors were placed 120° electrically apart. As with the dynamic eccentricity when the flux sensors are placed 120° mechanically apart the sidebands of the 3rd harmonic are attenuated because the phase difference of the three sensors at these frequencies are close to 120°. The sidebands around the 1st harmonic have the biggest amplitude. The better results appear when the sensors are placed 120° mechanically apart as they are further apart and can have better sensitivity to the eccentricity fault.

Chapter 6

Conclusions And Future Work

6.1 Conclusion

This thesis delves into the impact of eccentricity faults and evaluates various diagnostic methods, for the innovative C-GEN topology. The study utilized finite element modeling (FEM) to simulate fault conditions and employed multiple diagnostic techniques, aiming to identify the most effective strategies for detecting and characterizing eccentricity faults.

6.1.1 Methods and Diagnostic Evaluation

A range of diagnostic techniques were applied, including Motor Current Signature Analysis (MCSA), Torque monitoring, Magnetic flux analysis, Magnetically coupled search coils, and Zero Sequence Flux (ZSF) analysis. These methods were evaluated in the context of the C-GEN topology, which presents unique challenges due to its iron-less stator, Y-connected parallel coils, and symmetrical double rotor design. Generally C-GEN is a harmonic free machine.

6.1.2 Results and Analysis

1. Motor Current Signature Analysis (MCSA): MCSA was unable to reliably diagnose eccentricity faults in the C-GEN design. The double-rotor topology and Y-connected parallel coil configuration cancel the harmonics typically indicative of such faults. Consequently, MCSA failed to identify distinct fault-induced frequencies, limiting its diagnostic potential for this topology.
2. Torque Monitoring: Torque monitoring produces detectable results for static, dynamic, and mixed eccentricity faults. However, the amplitudes of the diagnostic harmonics were notably small under static eccentricity conditions. This limitation was attributed to the symmetry of the magnetic air-gap flux density, which remained almost identical to that of the healthy condition. Consequently, Torque monitoring was unable to effectively distinguish between faulty and healthy states under static eccentricity. For dynamic eccentricity, Torque monitoring successfully produced sideband characteristic frequencies at $\frac{2f_s}{p}$, which were absent under healthy conditions. However, these frequencies also exhibited small amplitudes, making it challenging to differentiate between different levels of dynamic eccentricity severity.
3. Flux Monitoring: Flux monitoring exhibited mixed outcomes:

- For **static eccentricity**, the method failed to generate fault-characteristic frequencies, as the third harmonic in the flux spectrum remained prominent even under healthy conditions, masking fault signatures.
- For **dynamic eccentricity**, flux monitoring successfully produced sideband frequencies f_s/p around the first and third harmonics. Compared to the Phase current spectrum, these harmonics don't cancel due to the parallel design of the coils, because the flux is independent of the circuit design.

4. Magnetically Coupled Search Coils: The magnetically coupled search coils method demonstrated good results across all eccentricity fault types. However, this approach has significant practical limitations. It is highly intrusive, requiring installation of 2 search coils within the air-gap that span 180°.
5. Zero Sequence Flux (ZSF) Analysis: ZSF analysis emerged as the most promising diagnostic technique for the C-GEN topology. It successfully generated characteristic fault signatures across all fault types, static, dynamic, and mixed eccentricity. Unlike other methods, ZSF was unaffected by the circuit design because it is based on the flux monitoring method and demonstrated a high degree of sensitivity to fault-induced asymmetries. Its ability to detect and differentiate between fault conditions makes it an optimal choice for real-world applications in fault detection, particularly for static eccentricity, where other methods have proven inadequate. The method's performance improves significantly when sensors are positioned 120° mechanically apart. This arrangement increases their spatial separation within the machine, enhancing sensitivity to flux variations among the three sensors and improving fault detection across all fault types.

6.2 Future Work

The ZSF and search coil methods should be applied in real-time experimental applications to validate their results and diagnostic capabilities. These diagnostic techniques should also be employed across different machine designs and fault types to assess their robustness. Enhancing the FEM simulations of the C-GEN model with improved sampling frequency could better align the machine's behavior with real-world conditions.

To examine the thermal effects of circulating currents on the machine, a thermal model of the C-GEN should be created. Machine learning approaches could also be applied to distinguish between various faults and identify faulty conditions.

The search coil method could be used by utilizing two coils placed within the stator air-gap, spanning 180°, 90° apart. This configuration could identify static eccentricity faults regardless of the directional position of the fault. Lastly, mathematical analysis should be developed to explain why, under dynamic eccentricity, the frequencies related to $f_s(k \pm m/p)$ for $m = 1$ are canceled, whereas for mixed eccentricity, both $m = 1$ and $m = 2$ frequencies are present.

Bibliography

[1] OpenEI. *Wind Energy*. Accessed: 2024-12-23. 2024. URL: https://openei.org/wiki/Wind_energy.

[2] World Wind Energy Association. *Annual Report 2023*. Accessed: 2024-12-23. 2023. URL: https://wwindea.org/AnnualReport2023.

[3] Wikipedia contributors. *Wind Turbine — Wikipedia, The Free Encyclopedia*. Accessed: 2024-12-23. 2024. URL: https://en.wikipedia.org/wiki/Wind_turbine.

[4] Geerten van de Kaa et al. "Wind turbine technology battles: Gearbox versus direct drive - opening up the black box of technology characteristics". In: *Technological Forecasting and Social Change* 153 (2020), p. 119933. ISSN: 0040-1625. DOI: https://doi.org/10.1016/j.techfore.2020.119933. URL: https://www.sciencedirect.com/science/article/pii/S0040162519313691.

[5] Samandar Khan Afridi et al. "Winds of Progress: An In-Depth Exploration of Offshore, Floating, and Onshore Wind Turbines as Cornerstones for Sustainable Energy Generation and Environmental Stewardship". In: *IEEE Access* 12 (2024), pp. 66147–66166. URL: https://ieeexplore.ieee.org/document/10521472.

[6] Alma Economics. *Social Impact Study*. Accessed: 2024-12-23. 2021. URL: https://www.eliamep.gr/wp-content/uploads/2021/09/Social-impact-study_Alma-Economics-1.pdf.

[7] European Commission. *Greece: National Energy and Climate Plan*. Accessed: 2024-12-23. 2020. URL: https://energy.ec.europa.eu/system/files/2020-03/el_final_necp_main_en_0.pdf.

[8] Stephen J. Chapman. *Electric Machinery Fundamentals*. 5th. New York: McGraw-Hill Education, 2011. ISBN: 978-0073529547.

[9] J. C. Malloch, D. M. Grant, and D. G. Robertson. "Carbon Brush Performance on Slip Rings". In: *2010 Petroleum and Chemical Industry Conference*. 2010, pp. 1–6. DOI: 10.1109/PCICON.2010.5666645. URL: https://ieeexplore.ieee.org/document/5556522.

[10] M. A. Rahman, A. M. Osheiba, and T. S. Radwan. "A Comparison between Hybrid Excited Permanent Magnet and Wound Rotor Machines". In: *2022 IEEE International Electric Machines & Drives Conference (IEMDC)*. 2022, pp. 1–6. DOI: 10.1109/IEMDC44711.2022.9842232. URL: https://ieeexplore.ieee.org/document/9842232.

[11] Z.Q. Zhu. "Recent Advances on Permanent Magnet Machines". In: *Diangong Jishu Xuebao/Transactions of China Electrotechnical Society* 27 (Mar. 2012), pp. 1–11.

[12] Author (if available) Chen. *Modelling and Design of Permanent Magnet Machines*. Accessed: 2024-12-23. URL: https://www.semanticscholar.org/paper/Modelling-and-Design-of-Permanent-magnet-Machines-Chen/0c0fc33940f702806c73608e9527e040cbdc3673.

[13] Stanford Magnets. *Permanent Magnet Generator: An Overview*. Accessed: 2024-12-23. URL: https://www.stanfordmagnets.com/permanent-magnet-generator-an-overview.html.

[14] IEEE Spectrum. *Axial Flux Motors: Compact, Efficient, and Gaining Ground*. Accessed: 2024-12-23. 2024. URL: https://spectrum.ieee.org/axial-flux-motor.

[15] Velington de Aquino Neumann and Roberto Petry Homrich. "Comparison between radial and axial permanent magnet generators for low speed application". In: *2014 11th IEEE/IAS International Conference on Industry Applications*. 2014, pp. 1–6. DOI: 10.1109/XXXX.2014.6860746. URL: https://ieeexplore.ieee.org/stamp/stamp.jsp?tp=&arnumber=6860746.

[16] Yicheng Chen, P. Pillay, and A. Khan. "PM Wind Generator Topologies". In: *IEEE Transactions on Industry Applications* 41.6 (2005), pp. 1619–1626. DOI: 10.1109/TIA.2005.858261.

[17] Yanli Feng and Chengning Zhang. "A Novel Method for the Core Loss Calculation in the Surface-Mounted Permanent Magnet Synchronous Machine". In: *International Journal of Applied Electromagnetics and Mechanics* (2018), pp. 427–444. DOI: 10.3233/JAE-170062. URL: https://content.iospress.com/articles/international-journal-of-applied-electromagnetics-and-mechanics/jae170062.

[18] Kyungil Woo et al. "Improvement of Torque Characteristics of Permanent Magnet Wind Generator by FEM and Optimization". In: *International Journal of Applied Electromagnetics and Mechanics* 33 (Oct. 2010). DOI: 10.3233/JAE-2010-1112.

[19] Vector Magnets. *Permanent Magnet Motors*. Accessed: 2024-12-23. 2024. URL: http://www.vectormagnets.com/oid1742283/Permanent-Magnet-Motors.htm.

[20] E.R. Braga Filho, A.M.N. Lima, and T.S. Araujo. "Reducing Cogging Torque in Interior Permanent Magnet Machines Without Skewing". In: *IEEE Transactions on Magnetics* 34.5 (1998), pp. 3652–3655. DOI: 10.1109/20.717863.

[21] Ayman M. EL-Refaie. "Fractional-Slot Concentrated-Windings Synchronous Permanent Magnet Machines: Opportunities and Challenges". In: *IEEE Transactions on Industrial Electronics* 57.1 (2010), pp. 107–121. DOI: 10.1109/TIE.2009.2030211.

[22] Soon-o Kwon et al. "Performance Comparison of IPMSM with Distributed and Concentrated Windings". In: *Conference Record of the 2006 IEEE Industry Applications Conference Forty-First IAS Annual Meeting*. Vol. 4. 2006, pp. 1984–1988. DOI: 10.1109/IAS.2006.256807.

[23] Harold Saavedra, Jordi-Roger Riba, and Luis Romeral. "Multi-objective Optimal Design of a Five-Phase Fault-Tolerant Axial Flux PM Motor". In: *Advances in Electrical and Computer Engineering* 15 (Feb. 2015), pp. 69–76. DOI: 10.4316/AECE.2015.01010.

[24] OSWOS. *Motor Windings*. Accessed: 2024-12-23. 2024. URL: https://oswos.com/motor-windings/.

[25] Lester Chong, Rukmi Dutta, and M.F. Rahman. "Application of Concentrated Windings in Interior Permanent Magnet Machine". In: *2007 Australasian Universities Power Engineering Conference*. 2007, pp. 1–5. DOI: 10.1109/AUPEC.2007.4548069.

[26] O. Keysan et al. "C-GEN, a Lightweight Direct Drive Generator for Marine Energy Converters". In: *5th IET International Conference on Power Electronics, Machines and Drives (PEMD 2010)*. 2010, pp. 1–6. DOI: 10.1049/cp.2010.0021.

[27] Alasdair Stewart McDonald. "Structural Analysis of Low Speed, High Torque Electrical Generators for Direct Drive Renewable Energy Converters". Accessed: 2024-12-23. PhD thesis. The University of Edinburgh, 2008. URL: https://era.ed.ac.uk/handle/1842/12608.

[28] O. Keysan et al. "Designing the C-GEN Lightweight Direct Drive Generator for Wave and Tidal Energy". In: *Renewable Power Generation, IET* 6 (May 2012), pp. 161–170. DOI: 10.1049/iet-rpg.2009.0213.

[29] Halil Çimen. "Development of the C-GEN Generator Technology for Vertical Axis Wind Turbines". Accessed: 2024-12-23. PhD thesis. The University of Edinburgh, 2023. URL: https://era.ed.ac.uk/handle/1842/39826.

[30] A. J. M. Cardoso, ed. *Diagnosis and Fault Tolerance of Electrical Machines, Power Electronics and Drives*. London, UK: IET, 2018. ISBN: 978-1-78561-291-7.

[31] Haneen Ghanayem, Mohammad Alathamneh, and R. Mark Nelms. "Decoupled Speed and Flux Control of a Three-Phase Permanent Magnet Synchronous Motor under an Open-Circuit Fault Using a PR Current Controller". In: *Energies* 16.14 (July 2023), p. 5325. DOI: 10.3390/en16145325. URL: https://www.mdpi.com/1996-1073/16/14/5325.

[32] M. Sumislawska et al. "The Impact of Thermal Degradation on Properties of Electrical Machine Winding Insulation Material". In: *IEEE Transactions on Industry Applications* 52.4 (2016), pp. 2951–2960. DOI: 10.1109/TIA.2016.2544745. URL: https://ieeexplore.ieee.org/document/7437443.

[33] Przemyslaw Pietrzak and Marcin Wolkiewicz. "Comparison of Selected Methods for the Stator Winding Condition Monitoring of a PMSM Using the Stator Phase Currents". In: *Energies* 14.6 (2021), p. 1630. DOI: 10.3390/en14061630. URL: https://www.mdpi.com/1996-1073/14/6/1630.

[34] V. Hegde and M. G. Sathyanarayana Rao. "Detection of Stator Winding Inter-Turn Short Circuit Fault in Induction Motor Using Vibration Signals by MEMS Accelerometer". In: *Electric Power Components and Systems* 45.13 (2017), pp. 1463–1473. DOI: 10.1080/15325008.2017.1358777. URL: https://doi.org/10.1080/15325008.2017.1358777.

[35] Farshid Mahmouditabar, Abolfazl Vahedi, and Fabrizio Marignetti. "The Demagnetization Phenomenon in PM Machines: Principles, Modeling, and Design Considerations". In: *IEEE Access* 11 (2023), pp. 47750–47773. DOI: 10.1109/ACCESS.2023.3274701.

[36] Zia Ullah and Jin Hur. "A Comprehensive Review of Winding Short Circuit Fault and Irreversible Demagnetization Fault Detection in PM Type Machines". In: *Energies* 11.12 (2018), p. 3309. DOI: 10.3390/en11123309. URL: https://www.mdpi.com/1996-1073/11/12/3309.

[37] J. Faiz and M. Ojaghi. "Different indexes for eccentricity faults diagnosis in three-phase squirrel-cage induction motors: A review". In: *Mechatronics* 19.1 (2009), pp. 2–13. DOI: 10.1016/j.mechatronics.2008.07.004. URL: https://www.academia.edu/48897840/Different_indexes_for_eccentricity_faults_diagnosis_in_three_phase_squirrel_cage_induction_motors_A_review.

[38] David G. Dorrell, W. T. Thomson, and S. Roach. "Combined Effects of Static and Dynamic Eccentricity on Airgap Flux Waves and the Application of Current Monitoring to Detect Dynamic Eccentricity in 3-Phase Induction Motors". In: *IEEE Transactions on Industry Applications* 32.5 (1996), pp. 1350–1358. DOI: 10.1109/28.536875. URL: https://ieeexplore.ieee.org/document/536875.

[39] Bashir Mahdi Ebrahimi, Jawad Faiz, and Mehrsan Javan Roshtkhari. "Static-, Dynamic-, and Mixed-Eccentricity Fault Diagnoses in Permanent-Magnet Synchronous Motors". In: *IEEE Transactions on Industrial Electronics* 56.11 (2009), pp. 4727–4739. DOI: 10.1109/TIE.2009.2022512. URL: https://ieeexplore.ieee.org/document/5226595.

[40] Kaswar Mostafa. "Direct Drive Wind Turbines: The Effect of Unbalanced Magnetic Pull on Permanent Magnet Generators and Bearing Arrangements". PhD thesis. The University of Edinburgh, 2018. URL: https://era.ed.ac.uk/handle/1842/31360.

[41] S. Rasid et al. "Detection of Eccentricity Faults in Air-Cored C-GEN PM Machines for Wind Turbine". In: *2021 IEEE International Electric Machines & Drives Conference (IEMDC)*. 2021, pp. 1–7. DOI: 10.1109/IEMDC47953.2021.9605529. URL: https://ieeexplore.ieee.org/document/9605529.

[42] Pakédam Lare. "Methodology for Modeling and Detection of Inter-Turn Short-Circuit Faults of a Permanent Magnet Assisted Synchronous Reluctance Motor in Electric Vehicles". NNT : 2023UPAST198. PhD Thesis. Université Paris-Saclay, 2023. URL: https://theses.hal.science/tel-04509413.

[43] Sang Bin Lee et al. "Condition Monitoring of Industrial Electric Machines: State of the Art and Future Challenges". In: *IEEE Industrial Electronics Magazine* 14.4 (2020), pp. 158–167. DOI: 10.1109/MIE.2020.3016138.

[44] Bashir Mahdi Ebrahimi and Jawad Faiz. "Configuration Impacts on Eccentricity Fault Detection in Permanent Magnet Synchronous Motors". In: *IEEE Transactions on Magnetics* 48.2 (2012), pp. 903–906. DOI: 10.1109/TMAG.2011.2172977.

[45] Yao Duan and Hamid Toliyat. "A Review of Condition Monitoring and Fault Diagnosis for Permanent Magnet Machines". In: *Power and Energy Society General Meeting, 2012 IEEE*. IEEE Power and Energy Society. San Diego, CA, USA: IEEE, July 2012. DOI: 10.1109/PESGM.2012.6345545.

[46] Jacek F. Gieras, Chong Wang, and Joseph Cho Lai. *Noise of Polyphase Electric Motors*. Vol. 129. Electrical and Computer Engineering. Boca Raton, FL: CRC Press, 2006. ISBN: 9780824723811. DOI: 10.1201/9781420027730. URL: https://doi.org/10.1201/9781420027730.

[47] John S. Hsu. "Monitoring of Defects in Induction Motors Through Air-Gap Torque Observation". In: *IEEE Transactions on Industry Applications* 31.5 (1995), pp. 1016–1021. DOI: 10.1109/28.464514. URL: https://ieeexplore.ieee.org/document/464514.

[48] Konstantinos N. Gyftakis et al. "Identification of the Broken Bar Fault in Induction Motors with Rotor Air Ducts Through the Torque Spectrum". In: *2014 International Conference on Electrical Machines (ICEM)*. 2014, pp. 1614–1620. DOI: 10.1109/ICELMACH.2014.6960398.

[49] Konstantinos N. Gyftakis, Panagiotis A. Panagiotou, and Dimitrios Spyrakis. "Recent Experiences with MCSA and Flux Condition Monitoring of Mechanical Faults in 6kV Induction Motors for Water Pumping Applications". In: *2019 IEEE International Electric Machines & Drives Conference (IEMDC)*. 2019, pp. 886–892. DOI: 10.1109/IEMDC.2019.8785335. URL: https://ieeexplore.ieee.org/document/8785335.

[50] Giorgos A. Skarmoutsos et al. "General Diagnostics in Direct-Drive Permanent-Magnet Synchronous Generators Using Two Magnetically-Coupled Search-Coils". In: *IEEE Transactions on Industry Applications* (2023), pp. 1–11. DOI: 10.1109/TIA.2023.3338196. URL: https://ieeexplore.ieee.org/document/10337651.

[51] Georgios Skarmoutsos. "Diagnostics and Analytical Modelling for Permanent-Magnet Synchronous Machines". PhD thesis. The University of Edinburgh, 2023. URL: https://hdl.handle.net/1842/40518.

[52] Marios Salinas et al. "Reliable Detection of Non-Adjacent Broken Rotor Bars via the Analysis of the Zero-Sequence Flux". In: *2024 International Conference on Electrical Machines (ICEM)*. 2024, pp. 1–6. DOI: 10.1109/ICEM60801.2024.10700394.

[53] Konstantinos N. Gyftakis et al. "Introduction of the Zero-Sequence Stray Flux as a Reliable Diagnostic Method of Rotor Electrical Faults in Induction Motors". In: *IECON 2019 - 45th Annual Conference of the IEEE Industrial Electronics Society*. Vol. 1. 2019, pp. 6016–6021. DOI: 10.1109/IECON.2019.8927775.

[54] Konstantinos N. Gyftakis and Joya C. Kappatou. "The Zero-Sequence Current as a Generalized Diagnostic Mean in Δ-Connected Three-Phase Induction Motors". In: *IEEE Transactions on Energy Conversion* 29.1 (2014), pp. 186–196. DOI: 10.1109/TEC.2013.2287757.

[55] O. C. Zienkiewicz, R. L. Taylor, and J. Z. Zhu. *The Finite Element Method: Its Basis and Fundamentals*. 6th. Oxford, UK: Elsevier, 2005. ISBN: 978-0-7506-6320-7.

[56] Gyftakis Konstantinos. "Electromagnetic Analysis of Induction Motor Faults and Development of New Diagnostic Methods to Detect Them". Ph.D. Dissertation. Patras, Greece: University of Patras, 2015.

[57] Xiaodong Liang et al. "Induction Motors Fault Diagnosis Using Finite Element Method: A Review". In: *IEEE Transactions on Industry Applications* 56.6 (2020), pp. 5915–5925. DOI: 10.1109/TIA.2020.3024899. URL: https://ieeexplore.ieee.org/document/8930293.

[58] Jian-Ming Jin. *The Finite Element Method in Electromagnetics*. 3rd. John Wiley & Sons, 2015. ISBN: 9781119108085. URL: https://books.google.com/books?hl=en&lr=&id=DFi-BgAAQBAJ&oi=fnd&pg=PP1&dq=the+finite+element+analysis+method+for+electromagnetic&ots=nIb0v0f7p1&sig=EKD8gDY4lHMS9pDbnHNTG_2FOX8.

[59] Siemens Digital Industries Software. *MAGNET Getting Started Guide*. Simcenter MAGNET 2022.1 User Documentation. 2022.

[60] Alexandros Sergakis et al. "Demagnetization Detection, Misdiagnosis and Impact in Permanent Magnet Generators". In: *2024 International Conference on Electrical Machines (ICEM)*. 2024, pp. 1–7. DOI: 10.1109/ICEM60801.2024.10700057.